LA-9841-PR
Progress Report

C.3

Los Alamos National Laboratory is operated by the University of California for the United States Department of Energy under contract W-7405-ENG-36.

Applied Nuclear Data Research and Development Semiannual Progress Report

October 1, 1982—March 31, 1983

Los Alamos National Laboratory
Los Alamos, New Mexico 87545

The four most recent reports in this series, unclassified, are LA-9060-PR, LA-9262-PR, LA-9468-PR, and LA-9647-PR.

This work was performed under the auspices of the US Department of Energy's Division of Reactor Research and Technology, Office of Basic Energy Sciences and Office of Fusion Energy; the Spent Fuel Project Office under the technical direction of the Savannah River Laboratory; and the Electric Power Research Institute.

Prepared by A. D. Mutschlecner, Group T-2

LA-9841-PR
Progress Report

UC-34c
Issued: August 1983

Applied Nuclear Data Research and Development Semiannual Progress Report

October 1, 1982—March 31, 1983

Compiled by
E. D. Arthur

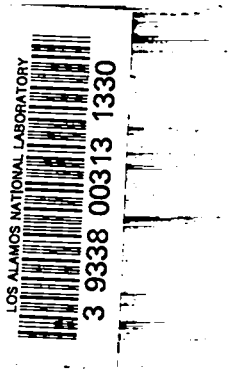

Los Alamos National Laboratory
Los Alamos, New Mexico 87545

CONTENTS

APPLIED NUCLEAR DATA RESEARCH AND DEVELOPMENT
SEMIANNUAL PROGRESS REPORT
October 1, 1982—March 31, 1983

Compiled by

E. D. Arthur

ABSTRACT

This progress report describes the activities of the Los Alamos Nuclear Data Group for October 1, 1982, through March 31, 1983. The topical content is summarized in the Contents.

I. THEORY AND EVALUATION OF NUCLEAR CROSS SECTIONS

A. Averaged Fusion Cross Sections for Polarized Plasma Applications [G. M. Hale, P. W. Keaton (ADPA), G. D. Doolen (X-5)]

We have continued to study cross sections for thermonuclear reactions induced by polarized particles, as interest in this subject increases in the fusion community. We had given results[1] for the d-t and d-d reactions when the axis of quantization is along the center-of-mass incident momentum direction ($\beta = 0$). Cross sections more appropriate for plasma applications, however, are defined by holding the axis of quantization and outgoing momentum direction fixed and averaging over incident momentum directions.

Such averaged cross sections are conveniently described in terms of the angles α, β, and γ, shown in Fig. 1, giving the relative orientations of the spin quantization axis (or external $\underline{\beta}$-field direction) $\hat{s}$, and the incoming- and outgoing-particle momenta, $\underline{k}$ and $\underline{k}'$, respectively.

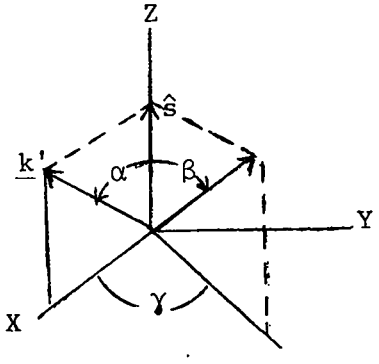

Fig. 1. Center-of-mass coordinate system for describing polarized cross sections.

The averaged cross sections for plasma applications are defined by

$$\bar{\sigma}_{m,n}(\alpha) = \frac{1}{4\pi} \int_0^{2\pi} d\gamma \int_{-1}^{1} d(\cos\beta)\sigma_{m,n}(\alpha,\beta,\gamma) \quad ,$$

and

$$\bar{\bar{\sigma}}_{m,n} = 2\pi \int_{-1}^{1} d(\cos\alpha)\bar{\sigma}_{m,n}(\alpha) \quad ,$$

where $\sigma_{m,n}(\alpha,\beta,\gamma)$ is the polarized differential cross section for projections m and n of the initial particle spins along $\hat{s}$.

Reactions dominated by s-waves in the entrance channel have no dependence on β, so the results given previously[1] for the d-t reaction at $\beta = 0$ hold almost equally well for the averaged cross sections. However, for the d-d reactions, $\bar{\sigma}_{m,n}$ and $\sigma_{m,n}(\beta = 0)$ are quite different for spin configurations [(m,n) = (1,0) and (1,-1)] to which the p-waves contribute substantially.

The values for $\bar{\sigma}_{m,n}$ given in Table I for the d-d reactions lead to different conclusions from those based on $\sigma_{m,n}(\beta = 0)$.[1] At energies of a few hundred keV, the best configuration for suppressing the cross section is (1,1) and the best one for enhancing it (the enhancement being somewhat lower than before) is (1,-1). These results were reported[2] at a Workshop on Polarized Fuel Reactors, held at Madison, Wisconsin, on March 28-30, 1983.

It was clear from the Workshop discussion that the main interest in polarized d-d reactions stems from the prospect of suppressing them in a d-^{3}He reactor in order to make it more nearly neutron-free. The results of our R-matrix calculations given in Table I indicate that suppressions of the d-d reactions relative to d-^{3}He (taking into account the enhancement of the d-^{3}He reaction by ~ 1.5 for parallel d and ^{3}He spins) of the order of 3 are attainable. These suppressions probably are not large enough to be of interest, and they differ significantly from the predictions of an earlier Russian study[3] of the D(d,p) reaction at 290 keV that gives much higher suppression. The feasibility of a d-^{3}He fusion reactor appears to depend critically on a reliable determination of the suppression of polarized d-d reactions, either from further analysis, or new measurements, or both.

TABLE I

POLARIZED CROSS SECTIONS FOR THE d-d REACTIONS

A. D(d,p)†

E_d(keV)	σ_0(mb)	$\frac{\bar{\sigma}_{1,1}}{\sigma_0}$	$\frac{\bar{\sigma}_{1,0}}{\sigma_0}$	$\frac{\bar{\sigma}_{1,-1}}{\sigma_0}$	$\frac{\bar{\sigma}_{0,0}}{\sigma_0}$
10	9.657×10^{-3}	1.197	.814	.990	1.373
50	4.780	1.077	.872	1.052	1.257
100	16.05	.950	.933	1.117	1.134
150	25.86	.853	.987	1.161	1.027
200	33.68	.778	1.034	1.188	.933
300	45.14	.675	1.108	1.217	.783
400	53.18	.607	1.161	1.232	.678
500	59.10	.559	1.197	1.244	.607

B. D(d,n)†

E_d(keV)	σ_0(mb)	$\frac{\bar{\sigma}_{1,1}}{\sigma_0}$	$\frac{\bar{\sigma}_{1,0}}{\sigma_0}$	$\frac{\bar{\sigma}_{1,-1}}{\sigma_0}$	$\frac{\bar{\sigma}_{0,0}}{\sigma_0}$
10	8.647×10^{-3}	1.032	.845	1.122	1.309
50	4.497	.886	.928	1.186	1.145
100	15.87	.746	1.007	1.247	.987
150	26.55	.647	1.069	1.284	.862
200	35.60	.575	1.120	1.305	.760
300	49.70	.481	1.195	1.324	.609
400	60.08	.424	1.245	1.331	.510
500	67.99	.386	1.278	1.336	.445

---

†Sum rule for cross sections

$$1/9(2\sigma_{1,1} + 4\sigma_{1,0} + 2\sigma_{1,-1} + \sigma_{0,0}) = \sigma_0.$$

B. R-Matrix Analysis of Reactions in the ^{4}He System (G. M. Hale and D. C. Dodder)

Due to current high interest in polarized d-d reactions, as explained at the end of the preceding contribution, we have reactivated our analysis of reactions in the ^{4}He system, adding new polarization data[4] for the d-d reactions. We find that the new data do not materially change the results of the analysis, because they were already in qualitative agreement with its predictions. The fits including the new data reinforce our result, unfortunately, that polarizing the d-d reactions does not suppress them enough to make the d-^{3}He reaction chain an attractive neutron-free alternative to d-t.

C. Complete Fokker-Planck Treatment of Slowing Down Due to Small-Angle Charged-Particle Elastic Scattering [G. M. Hale and A. Andrade (X-2)]

The availability of complete theoretical expansions[5] that give reliable representations of the measurements for most of the elastic scattering processes among light ions has induced us to consider the nuclear and Coulomb-nuclear interference components (σ_{NI}) of elastic scattering cross sections in the Fokker-Planck (F-P) treatment of small-angle slowing down. Previous treatments have included only the Rutherford cross section (σ_R). We find that integrals over the angles of σ_{NI} occurring in the terms of the F-P equation can be done analytically in terms of confluent hypergeometric functions and Legendre polynomials. The remaining integrals over the velocity distributions of the plasma ions are not difficult to perform numerically and can be done analytically under certain simplifying assumptions.

Our first test case, that of monoenergetic deuterium ions injected into a plasma of "cold" tritium ions and 1-keV temperature electrons, has been chosen with δ-function ion distributions so that all integrals can be evaluated analytically. Shown in Fig. 2 is a ratio comparing the rate of average energy loss due to the σ_{NI} component of the d-T cross section with the loss due to σ_R alone, plotted as a function of deuteron injection energy. The losses are for ion-ion collisions at center-of-mass angles up to 30°. This is perhaps a larger angular range than is typically considered in F-P calculations, but one should remember that we are not limited by the assumption that the cross section is pure Rutherford.

One sees that, at deuteron energies above ~ 4 MeV, significantly more energy is lost to the ions than would be predicted from considering Rutherford

scattering alone. The slight decrease in energy loss relative to Rutherford scattering at energies below 4 MeV is due to Coulomb-nuclear interference effects. These results were reported[6] recently at the Sherwood Plasma Theory Meeting in Alexandria, Virginia. We are presently considering more realistic cases having finite plasma ion temperatures.

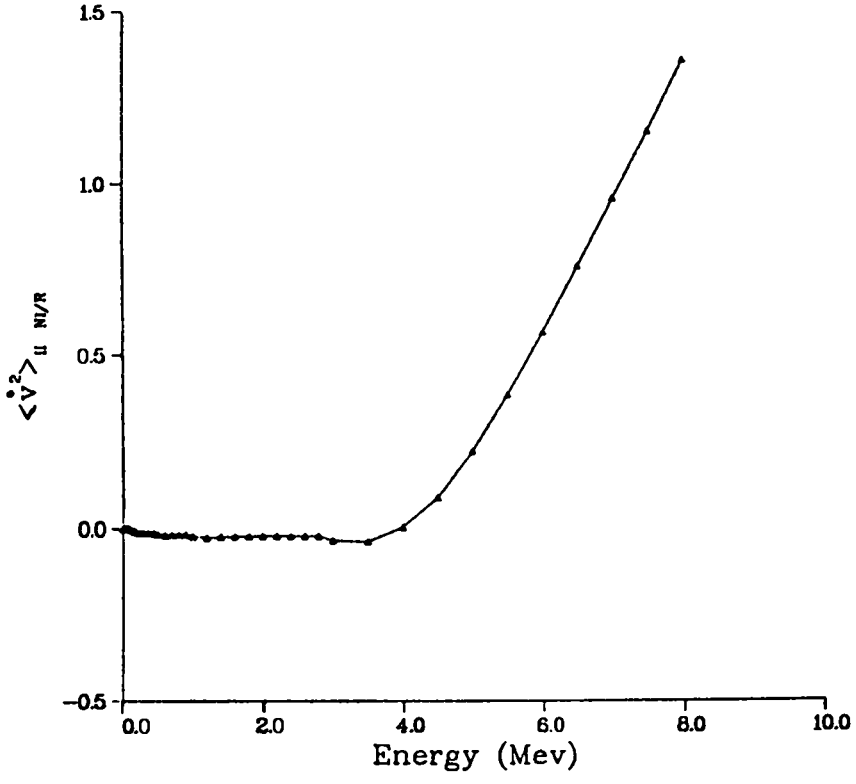

Fig. 2. Ratio of the average rate of energy loss due to σ_{NI} to the loss due to σ_R for a d-t plasma at deuteron injection energies below 8 MeV. Elastic collisions at center-of-mass scattering angles up to 30° have been included in the Fokker-Planck calculation.

D. Hauser-Feshbach Parameter Studies for Nitrogen and Oxygen Cross-Section Calculations (E. D. Arthur and P. G. Young)

Nuclear data evaluation for light elements often requires the use of theoretical models to provide cross sections for reaction channels or energy regions where experimental data do not exist. Hauser-Feshbach calculations are frequently used in such circumstances even though measured data show resonances and other features that indicate departures from the statistical assumption embodied in these models. Realizing these problems, we have derived input parameter sets that reproduce a variety of experimental data and which may offer some possibility for cross-section prediction.

Our most extensive effort has been concerned with the determination of spherical optical model parameters applicable to nitrogen and oxygen isotopes. We desired neutron optical parameters that could produce realistic compound-nucleus formation cross sections over an extended energy range, while simultaneously producing transmission coefficients suitable to the description of low-energy neutron emission. To derive such parameter sets, we simultaneously fitted the average behavior of total and integrated elastic cross sections for incident neutron energies between 0.1 and 16 MeV. We excluded explicit consideration of elastic angular distributions because of the effects of resonance structure on such data. However, we compared them later with results calculated using the final parameter sets, finding reasonable agreement. The optical parameters deduced from our fits appear in Table II. Figure 3 compares calculated shape elastic cross sections for oxygen with data measured at Duke University.[7]

We also investigated the behavior of other parameters for light nuclei, most notably those associated with the Gilbert-Cameron[8] level-density model. The Cook parameters[9] used in our Hauser-Feshbach calcuations do not extend below neutron or proton numbers less than 10. This situation affects primarily the determination of pairing energies applicable for use in light systems such as nitrogen or oxygen. To remedy this, we tabulated the proton and neutron pairing contributions [P(Z) and P(N), respectively], observed their systematic behavior, and extrapolated to Z or N = 5 on this basis. The results of this extrapolation appear in Figs. 4-a and 4-b, where the solid curves illustrate the existing P(Z) or P(N) values and the dashed regions indicate our extrapolation. A similar procedure was followed for the shell terms, S(Z) and S(N), used in the determination of the Fermi-gas parameter $\underline{a}$, through the Gilbert-Cameron expression

$$a/A = 0.00917[S(Z) + S(N)] + 0.142 \quad .$$

The smallness and opposite signs of S(Z) and S(N) cause their precise values to be of secondary importance when compared with the constant in the above expression. We did, however, check the inferred a values through comparison with observed resonance spacing data where possible.

TABLE II

OPTICAL MODEL PARAMETERS FOR NEUTRON REACTIONS ON LIGHT NUCLEI[a]

		r	a
Nitrogen			
	$V = 48. - 0.2E - 0.0008E^2$	1.35	0.70
	$V_{SO} = 7.0$	1.31	0.66
	$W_{SD} = 2.5 + 0.625E$	1.26	0.51
Above	E = 4.8 MeV		
	$W_{SD} = 5.5$		
Oxygen			
	$V = 47. - 0.28E - 0.02E^2$	1.38	0.71
	$V_{SO} = 7.0$	1.3	0.66
	$W_{SD} = 1. + 0.8E$	1.2	0.4
Above	E = 5 MeV		
	$W_{SD} = 5.$		

[a]All well depths in MeV, geometrical parameters in fermis, energies (E) are in the laboratory system.

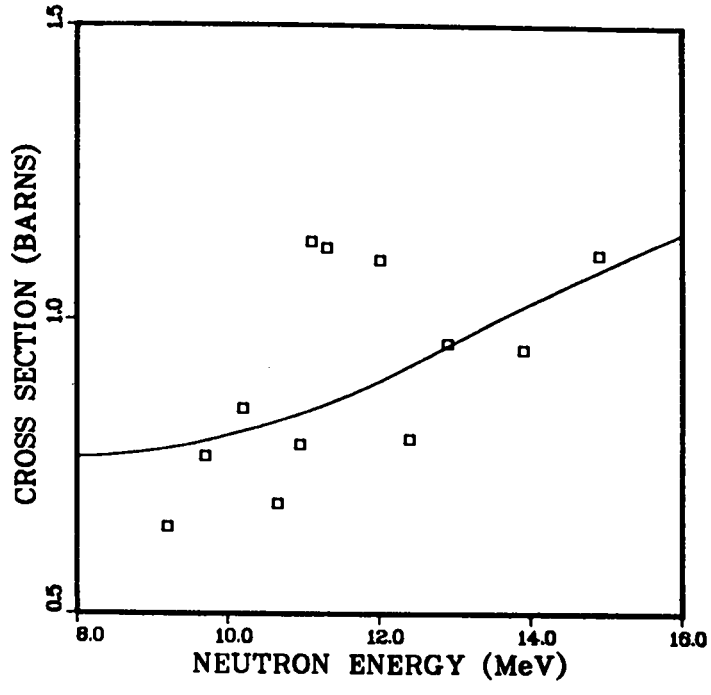

Fig. 3. Shape elastic cross sections for $n+^{16}O$ calculated with the optical parameters of Table II are compared with the data of Beyerele et al.[7]

Fig. 4-a.

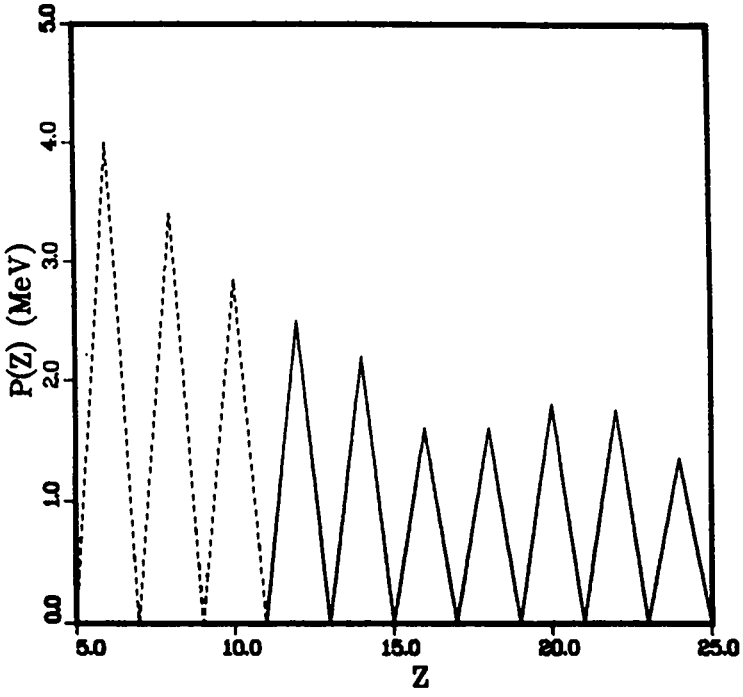

Fig. 4-b.

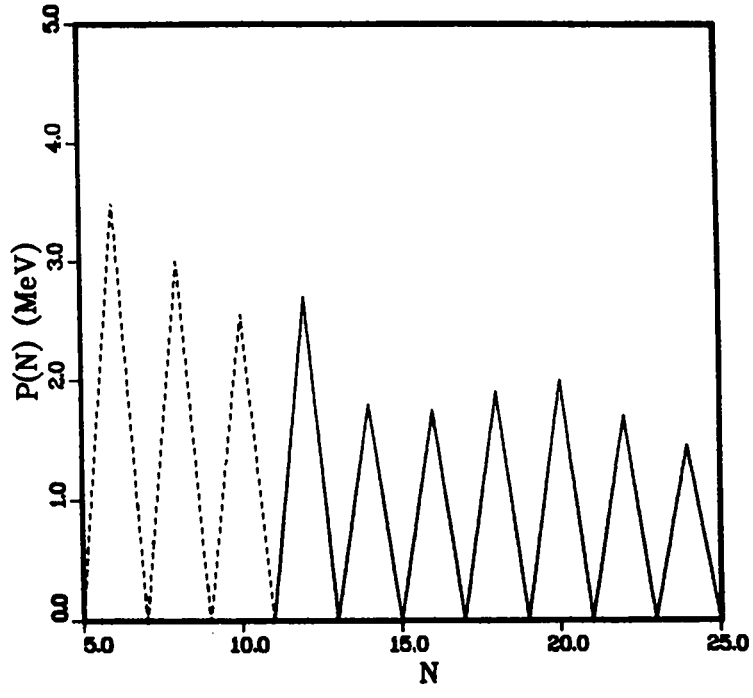

Fig. 4-a and 4-b. Trends in proton and neutron pairing contributions [P(Z) and P(N)] for level-density calculations employing the Cook parameter sets.[9] The dashed portions are our extrapolation of these parameters to smaller Z and N values.

E. Evaluation of Neutron-Induced Reactions on ^{15}N (P. G. Young and E. D. Arthur)

The evaluation of n+^{15}N data currently in the ENDF/B-V data library was completed in 1977.[10] Below E_n = 5.4 MeV, the evaluation is based on an R-matrix analysis of total and elastic scattering angular distribution measurements and is thought to be reasonably reliable. At higher energies, however, experimental data are more sparse and consist almost entirely of total cross-section data. In particular, at energies above 5.4 MeV the evaluation relies completely on Hauser-Feshbach statistical theory calculations to distribute the measured total cross sections among an abundance of partial reaction channels. Since 1977, considerable new information has become available on the nuclear level structure of nuclei in this mass region, and improved methods for applying Hauser-Feshbach statistical theory have been developed. The purpose of the present analysis is to apply these new methods and information to upgrade the ENDF/B-V evaluation above 5.4 MeV.

The Hauser-Feshbach statistical calculations were performed using the GNASH nuclear model code.[11] A schematic illustration of the various reaction sequences used in the calculation is included in Fig. 5, with Q-values and energy thresholds given in Table III. The input quantities required for the calculations were the transmission coefficients for neutrons, protons, deuterons, tritons, alpha particles, and gamma rays; energies, spins, parities, and gamma-ray branching ratios for discrete energy levels in each residual nucleus (see Fig. 5); nuclear level-density parameters to describe the "continuum" region of the residual nuclei where individual level data are incomplete; and parameters for preequilibrium corrections of the binary reaction channels for incident energies above ~ 10 MeV.

Discrete nuclear level information for the calculations was obtained from the recent compilations by Selove,[12,13,14] and the level-density formulation of Gilbert and Cameron[8] was utilized at higher excitation energies. This level-density model consists of a constant temperature form at low excitation energy joined smoothly to a Fermi-gas shape at higher energies. The total number of levels of ^{15}N, which is the most important residual nucleus in these calculations, is shown in Fig. 6. The solid curve indicates a constant temperature form, and the dashed curve is a Fermi-gas shape joined at E_x = 10.8 MeV. Below 10.8 MeV, the actual levels (points) were used in the calculation, and the Fermi-gas shape was employed at higher energies. Although level densities are usually quite important in calculations of this nature, their significance in

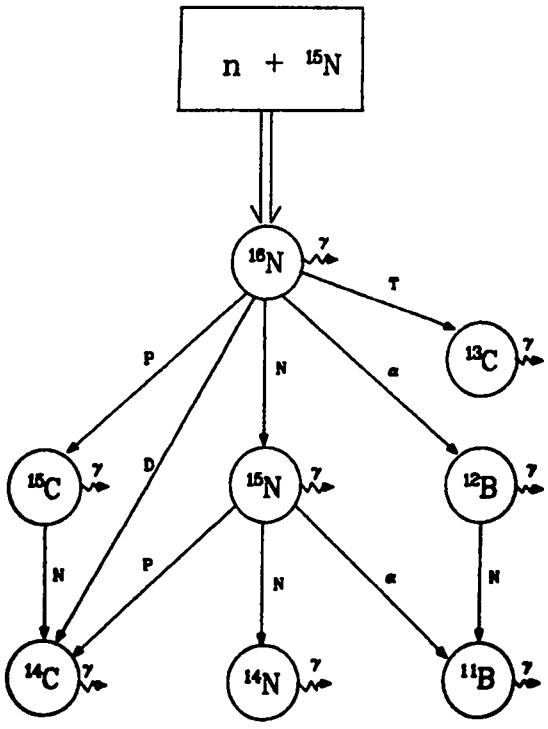

Fig. 5. Schematic diagram of the reaction sequences calculated for neutrons incident on ^{15}N.

Fig. 6. Cumulative number of nuclear energy levels in ^{15}N as a function of the excitation energy. The squares indicate measured data; the solid curve is calculated from a temperature (T = 2.6 MeV) level-density expression; and the solid curve is calculated using a Fermi-gas shape (a = 2.1 MeV^{-1}).

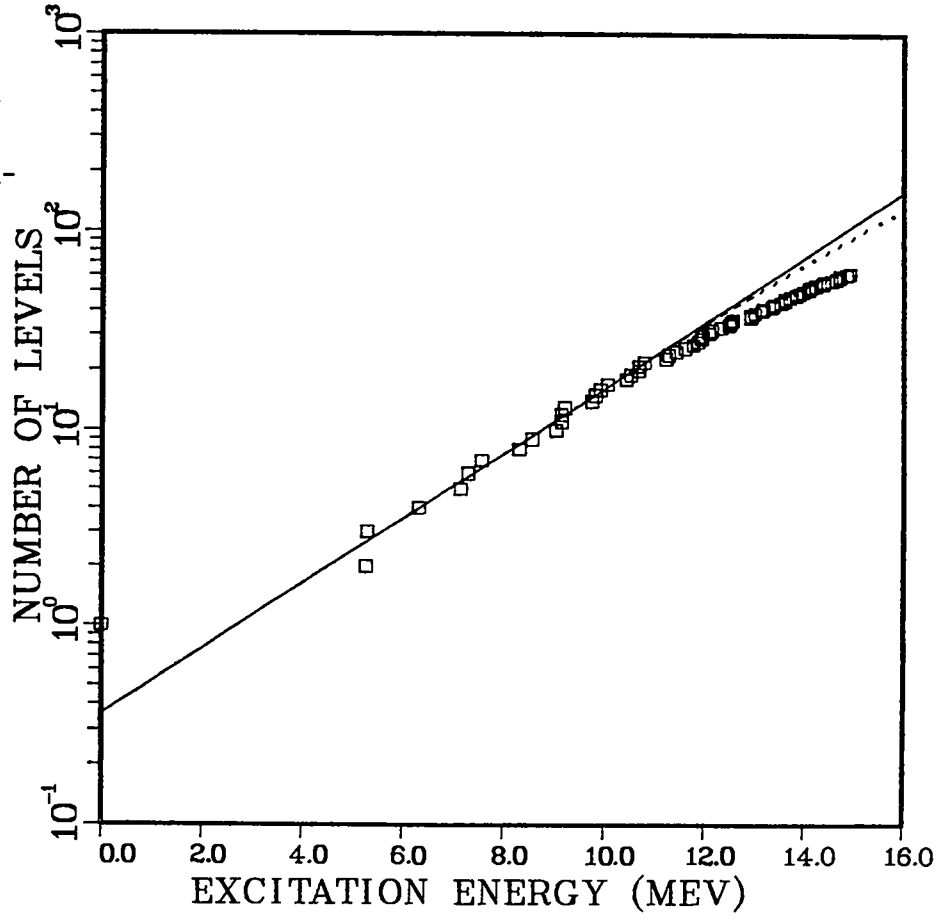

the present case is lessened by the large amount of discrete level data available for the relatively light nuclei involved. For example, with 14-MeV incident neutrons, we only have to extrapolate the ^{15}N level density ~ 2.3 MeV above the measured region.

The most important (variable) input for the calculations is the neutron transmission coefficients. These quantities were determined from spherical optical model calculations using the parameterization described in the previous article (Section D). Global spherical optical model parameters were used to calculate transmission coefficients for the proton,[15] deuteron,[16] triton,[17] and alpha[18] channels. Gamma-ray transmission coefficients were determined using a giant dipole resonance model,[19,20] with normalization inferred from comparisons of calculated $^{14}N(n,\gamma)$ cross sections with $^{14}N(p,\gamma)$ measurements. The result agreed approximately with that obtained from normalizing a calculated gamma-ray strength function to $2\pi\langle\Gamma_\gamma\rangle/\langle D_0\rangle$ values inferred from the measured ^{15}N-level structure.

Portions of the results of the new evaluation are shown in Figs. 7-12. In all cases, the solid curve indicates the present results and the dashed curve is ENDF/B-V.

Figure 7 compares the ENDF/B-V ^{15}N total cross-section evaluation, which was also used for the present evaluation, with the experimental data of Zeitnitz[21] from 6 to 20 MeV. The evaluated elastic cross sections are compared over the same energy range in Fig. 8. The new elastic results, which are $\cong$ 20% higher than ENDF/B-V above 11 MeV, are much more consistent with measured data for ^{14}N.

The (n,n') and (n,2n) cross sections are shown in Fig. 9, and the (n,p) and (n,d) cross sections are compared in Fig. 10 with the very limited experimental data[22,23] that are available. The increase in the elastic cross section above ENDF/B-V noted above was accompanied by significant decreases in the (n,2n), (n,p), (n,α), and (n,np) cross sections. Changes were less dramatic in the total (n,n') and (n,d) cross sections, although significant modifications did occur for (n,n') reactions to individual states.

The total gamma-ray production cross section is given in Fig. 11. Changes between evaluations are greatest in this quantity from 8-13.5 MeV. The spectra of secondary gamma rays from 14-MeV incident neutrons are compared for the two evaluations in Fig. 12. While the differences are not profound, the new calculations do result in a somewhat harder gamma spectrum.

TABLE III

Q-VALUES AND ENERGY THRESHOLDS FOR n+^{15}N REACTIONS BELOW 20 MeV

Reaction	Q-Value (MeV)	Threshold (MeV)
$^{15}N(n,\gamma)^{16}N$	2.491	——
$^{15}N(n,n')^{15}N^*$	-5.270	5.625
$^{15}N(n,2n)^{14}N$	-10.833	11.561
$^{15}N(n,p)^{15}C$	-8.989	9.594
$^{15}N(n,d)^{14}C$	-7.983	8.520
$^{15}N(n,t)^{13}C$	-9.902	10.568
$^{15}N(n,\alpha)^{12}B$	-7.621	8.134
$^{15}N(n,np)^{14}C$	-10.207	10.893
$^{15}N(n,nd)^{13}C$	-16.159	17.246
$^{15}N(n,nt)^{12}C$	-14.848	15.846
$^{15}N(n,n\alpha)^{11}B$	-10.991	11.730
$^{15}N(n,2np)^{13}C$	-18.384	19.620

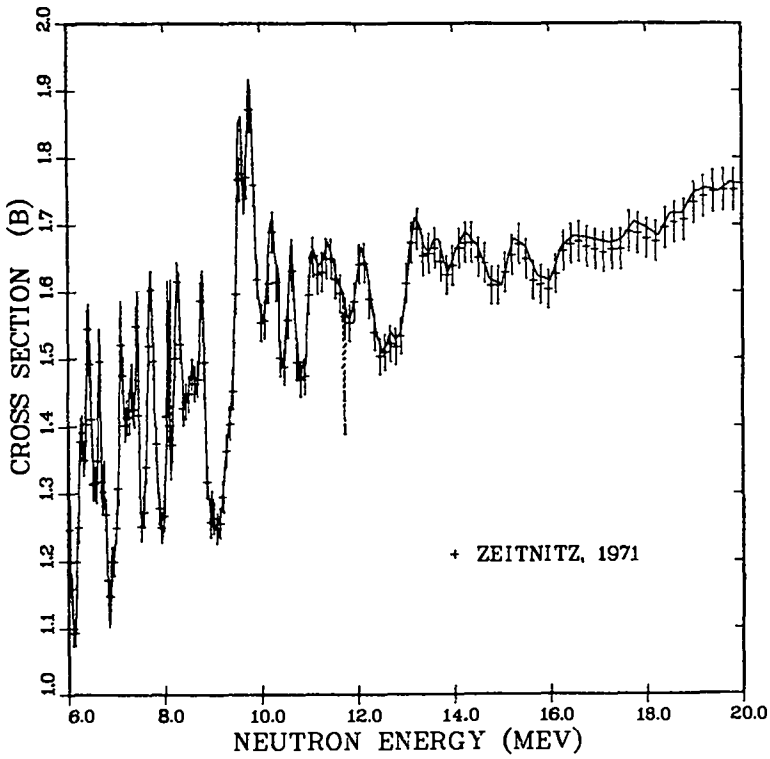

Fig. 7. Experimental and evaluated neutron total cross section of ^{15}N from 6 to 20 MeV. The solid curve is the present evaluation, the dashed curve is ENDF/B-V, and the points are the data of Zeitnitz et al.[21]

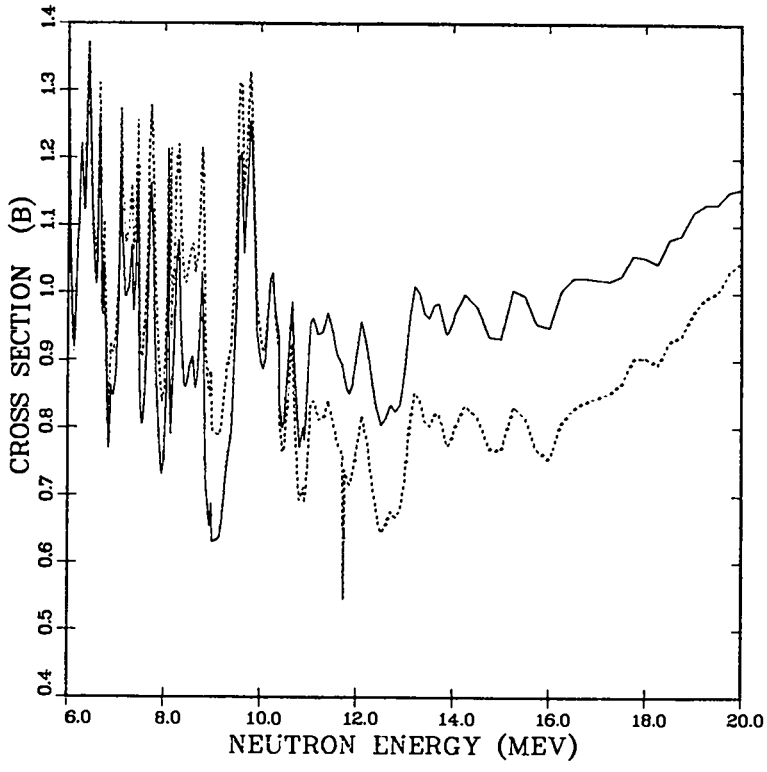

Fig. 8. Evaluated elastic cross section for n+^{15}N from 6 to 20 MeV. The solid curve is the present evaluation and the dashed curve is ENDF/B-V.

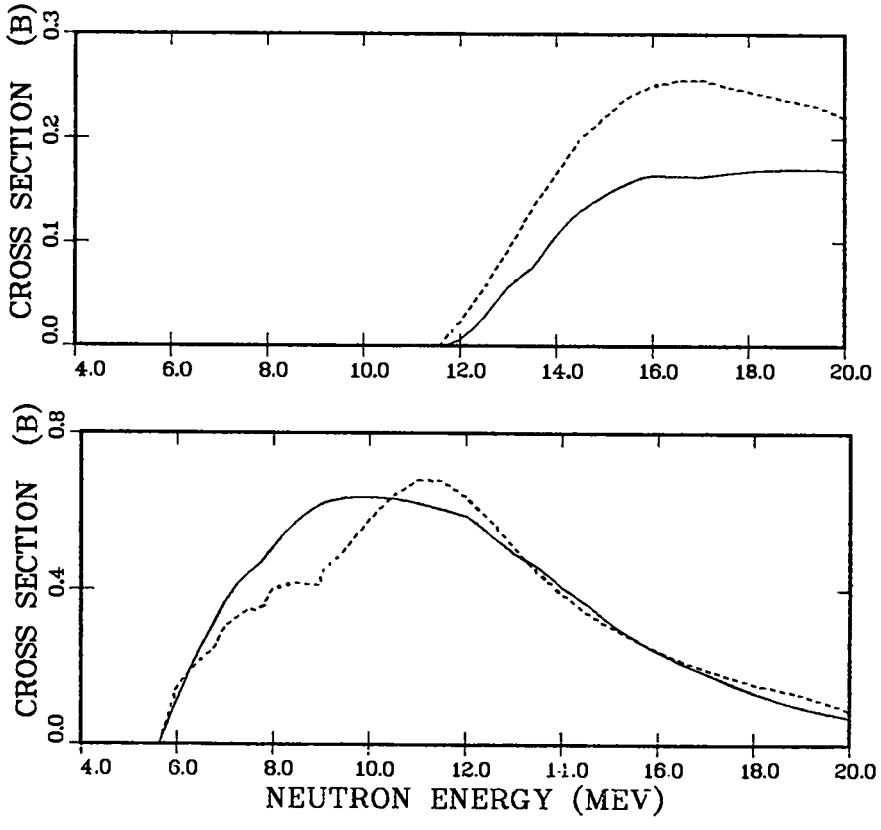

Fig. 9. Evaluated (n,2n) [upper] and total (n,n') [lower] cross sections of ^{15}N from threshold to 20 MeV. See caption to Fig. 7 for explanation of curves.

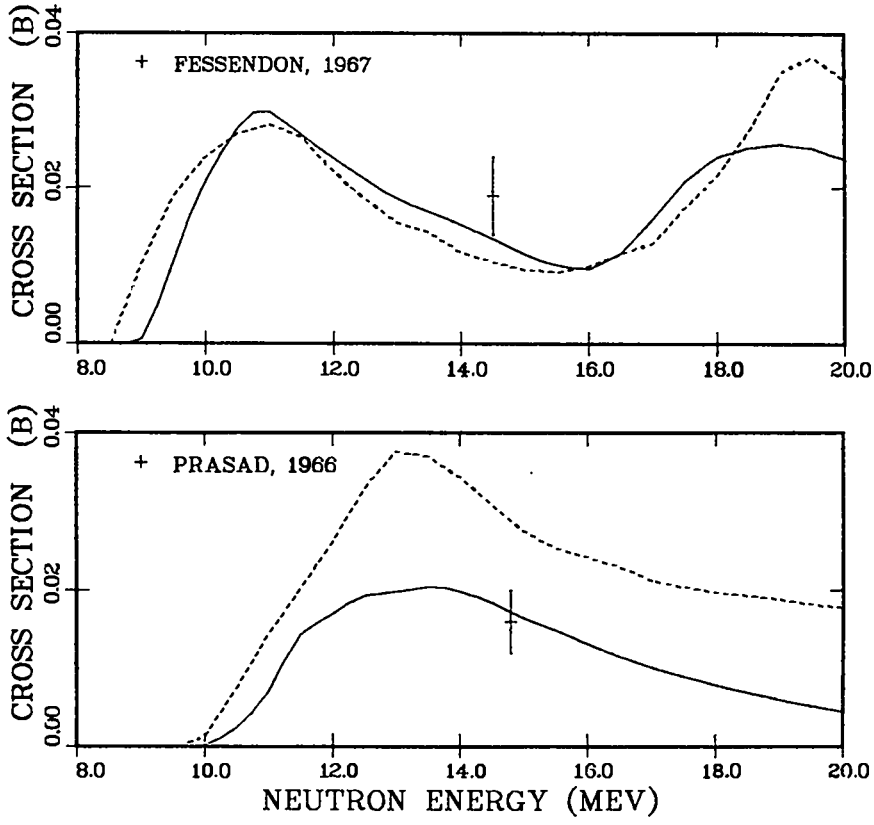

Fig. 10. Measured[22,23] and evaluated cross sections for the $^{15}N(n,p)$ [upper] and $^{15}N(n,d)$ [lower] reactions from threshold to 20 MeV. The solid curve is the present evaluation, the dashed curve is ENDF/B-V, and the points are experimental data.

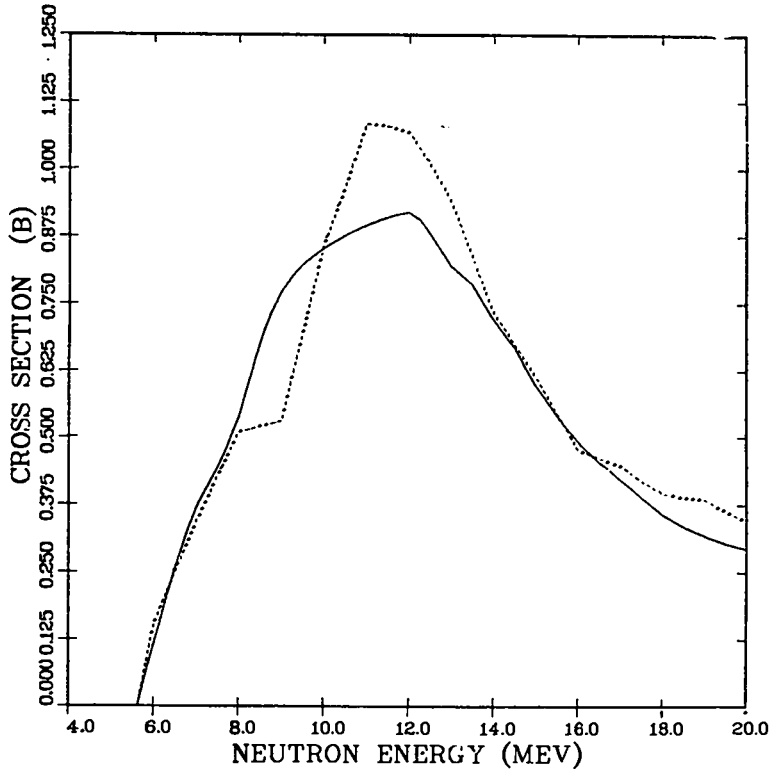

Fig 11. Evaluations of the total gamma-ray production cross sections for neutron reactions on ^{15}N. See caption to Fig. 10 for explanation of curves.

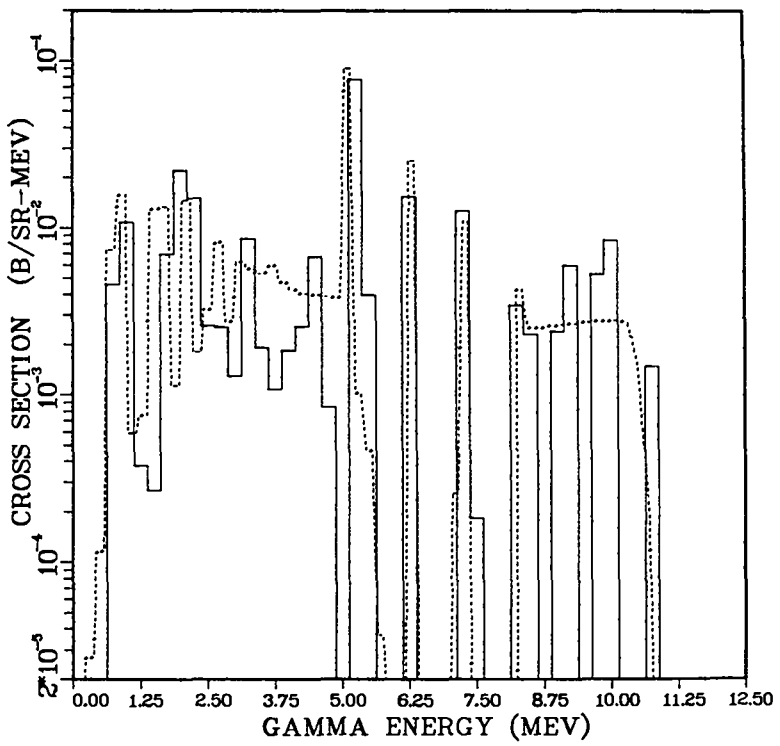

Fig. 12. Evaluated spectra of secondary gamma rays from 14-MeV neutron interactions on ^{15}N. The solid curve is the present evaluation, while the dashed curve is ENDF/B-V.

F. Calculation of n+^{239}Pu Cross Sections up to Neutron Energies of 20 MeV (E. D. Arthur)

Earlier (see Ref. 24, p. 28, and Ref. 25) we reported Hauser-Feshbach/coupled-channel calculations for n+^{239}Pu reactions over the neutron energy range from 0.001 to 5 MeV where the primary interest was the determination of realistic inelastic cross sections. We now report extension of these calculations up to 20 MeV where again the principal motivation was production of realistic inelastic cross sections that could be used in a new revision to the current ENDF/B-V evaluation for ^{239}Pu. We were also interested in (n,2n) and (n,3n) processes because of the scarcity of experimental measurements or theoretical calculations.

To perform most of the higher energy calculations we used the GNASH Hauser-Feshbach statistical model code,[11] which includes preequilibrium corrections necessary at higher energies. As we reported earlier (see Ref. 26, p. 18), the

code now includes a realistic fission model description for each compound nucleus occurring in a given calculation. This model allows us to describe the fission barrier using 2 or 3 uncoupled oscillators and includes suitable flexibility needed to describe the fission transition state spectrum at each barrier as well as level-density enhancements that may occur there. We also extended our ECIS[27] coupled-channel calculations to 20 MeV in order to determine direct-reaction contributions to inelastic scattering as well as to provide neutron transmission coefficients for use in the GNASH calculations. To do so we employed the deformed neutron optical model parameters we reported earlier (see Ref. 28, p. 15).

Multichance fission contributions [(n,nf), (n,2nf), etc.] occurring at higher incident energies introduce complications into Hauser-Feshbach calculations of the total fission cross section. Their presence leads to conditions in which the adjustment of numerous fission parameters is required. Because of unknowns associated with the higher energy behavior of these various components, shape uncertainties can be introduced into the total calculated fission cross section. Finally, because higher energy Hauser-Feshbach calculations can be time consuming and costly to perform, reliable fission parameter adjustments can be difficult to achieve, especially in the cases in which not enough information is available for parameter constraint.

To minimize such difficulties, we used, as independent sources of data, direct-reaction fission probabilities (P_f) and newly measured[29] neutron-induced fission cross sections on ^{238}Pu. Such data sources allowed us to introduce additional constraints for barrier parameter determination associated with the ^{239}Pu and ^{238}Pu compound nuclei occurring in second- and third-chance fission. In the analysis of these data, we employed fission models identical to the ones we ultimately used in our calculation of the total n+^{239}Pu fission cross sections. Additionally, in the case of P_f data, we accounted explicitly for spin population differences occurring between direct-reaction and neutron-induced reactions. The net result of these analyses was a reliable set of starting barrier parameter values for use in our higher energy n+^{239}Pu calculations.

Examples of fits to these data types appear in Figs. 13-15. In Fig. 13 we compare our calculated ^{238}Pu(n,f) value with the recent data of Budtz-Jørgensen et al.[29] In this case we did not attempt to optimize the fit to the data below 0.1 MeV because our application of the barrier parameters to the ^{239}Pu(n,n'f) reaction is not particularly sensitive to this behavior. The barrier parameters

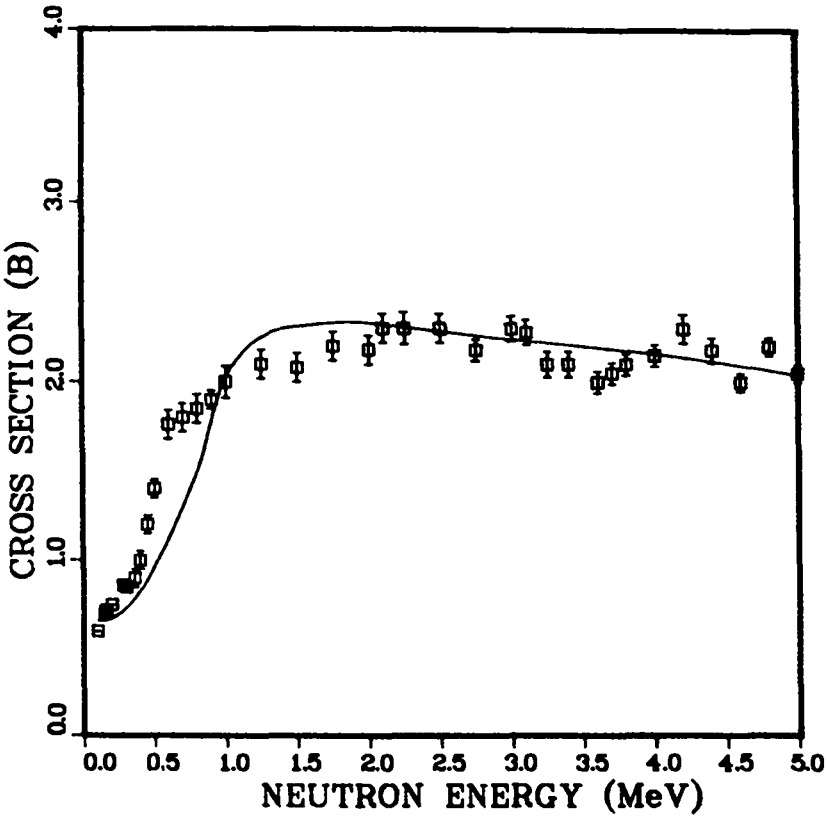

Fig. 13. Calculated $^{238}Pu(n,f)$ cross sections used to obtain initial values for the ^{239}Pu barrier parameters appearing in Table IV are compared with the data of Budtz-Jørgensen et al.

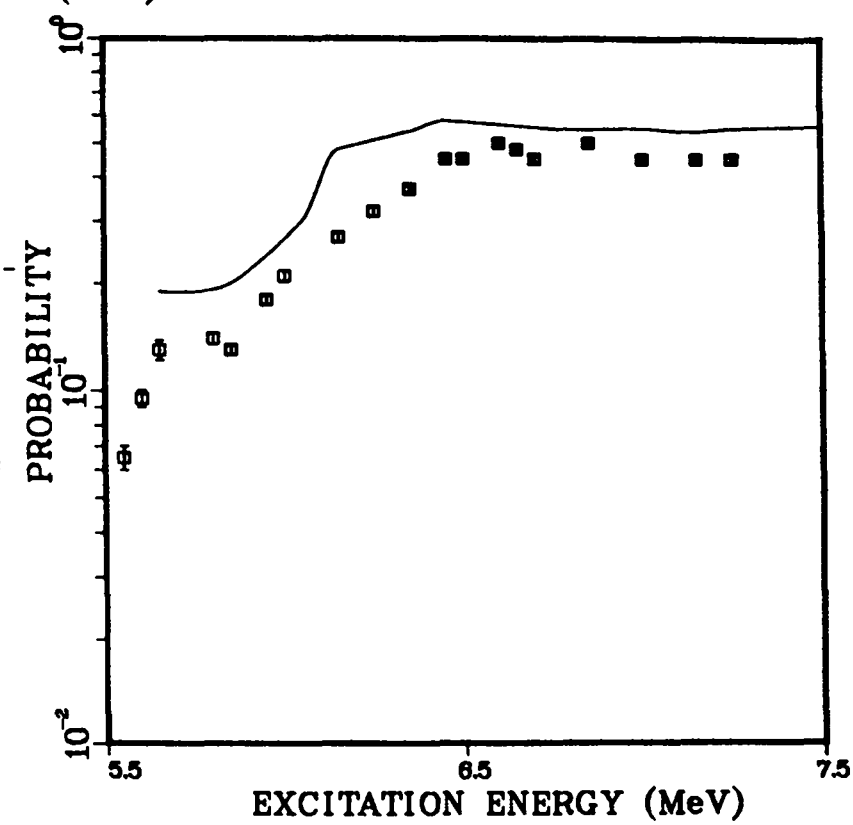

Fig. 14. Fission probabilities (Pf) for ^{239}Pu measured using the $^{238}Pu(d,pf)^{239}Pu$ direct reaction* are compared with the Pf deduced from new $^{238}Pu(n,f)$ measurements[29] (solid curve). The probabilities given by the curve are more consistent with data needed to fit second-chance fission contributions in our $n+^{239}Pu$ fission calculations.

*H. C. Britt, Los Alamos National Laboratory, provided this information in September 1982.

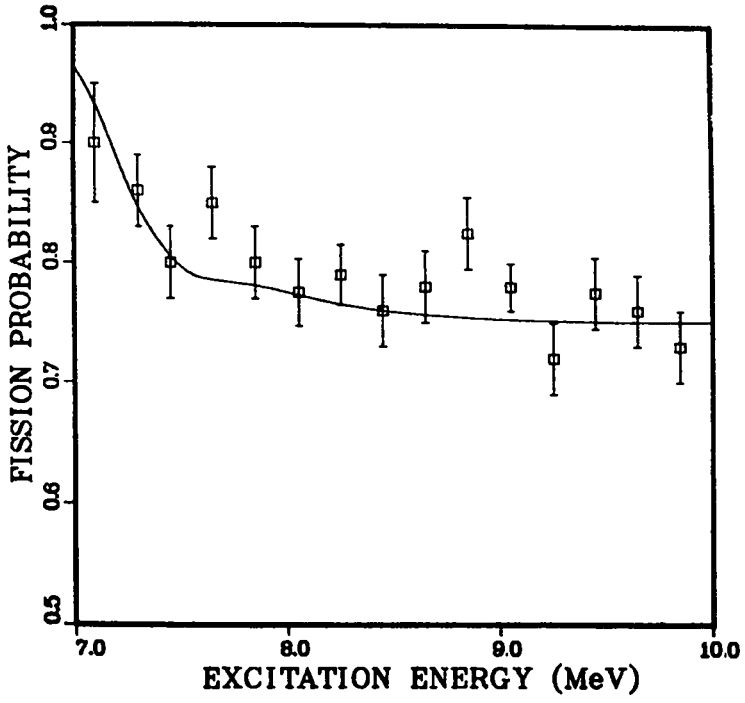

Fig. 15. Our fits to fission probabilities (P_f) measured in the $^{238}Np(^3He,df)$ ^{238}Pu reaction, which were used to determine ^{238}Pu barrier parameters appearing in Table IV, are compared with data.* In these calculations, explicit account was taken of the compound nucleus spin populations produced in this direct reaction.

deduced from the data fit the onset of the $^{239}Pu(n,n'f)$ cross section reasonably well, as we will show later. However, they disagree substantially with parameters required to fit fission probabilities for ^{239}Pu, as determined from use of $^{238}Pu(d,pf)$ reaction data. This situation is illustrated in Fig. 14. We suspect that this disagreement stems from problems in deuteron breakup corrections applied in the analysis of this reaction. More reliable P_f data exist for the ^{238}Pu compound nucleus, as obtained through the $^{237}Np(^3He,df)$ reaction.* Figure 15 shows our fit to these data after explictly accounting for the spin population produced in the $(^3He,df)$ direct reaction.

Small adjustments were made in the barrier parameters obtained from these analyses to optimize agreement to measured data in our calculations of the total fission cross section for ^{239}Pu. These adjustments were small and our

*H. C. Britt, Los Alamos National Laboratory, provided this information in September 1982.

final parameters are summarized in Table IV. Figure 16 compares our calculation (solid curve) with data measured by Kari.[30] The dashed and dotted curves illustrate the higher energy behavior that we calculated for the (n,n'f) and (n,2nf) contributions to the total fission cross section.

TABLE IV

FISSION PARAMETERS FOR n+^{239}Pu CALCULATIONS[a]

		Barrier Height (MeV)	ħω (MeV)	Density Enhancement
^{240}Pu	A	5.8	0.8	16
	B	5.45	0.6	2
^{239}Pu	A	5.7	0.60	2.5
	B	5.05	0.50	2.5
^{238}Pu	A	6.1	0.9	5.
	B	5.55	0.85	2.

[a]The nuclei appearing in the table are compound nuclei populated in the multichance fission of n+^{239}Pu. The inner and outer fission barriers are labeled A and B, respectively. The density enhancement shown is multiplied by $U^{\frac{1}{4}}$ for excitation energies, U > 1 to obtain an overall level-density enhancement.

A main purpose for the extension of these calculations to higher energies was determination of inelastic-scattering cross sections from threshold to 20 MeV. For low-lying levels that occupy the ground-state rotational band, the main contribution for neutron energies above a few MeV comes from direct-reaction contributions that we calculated using the ECIS code. For higher lying levels, including those built on other bandheads, we assumed only compound nucleus contributions, so that their inelastic cross sections are essentially negligible above 5-6 MeV. However, there are significant contributions to continuum inelastic scattering occurring from preequilibrium corrections applied in our calculations. This behavior is illustrated in Fig. 17. More details concerning these calculated inelastic cross sections appear in the following section that deals with changes incorporated in the revision to the ^{239}Pu ENDF/B-V evaluation.

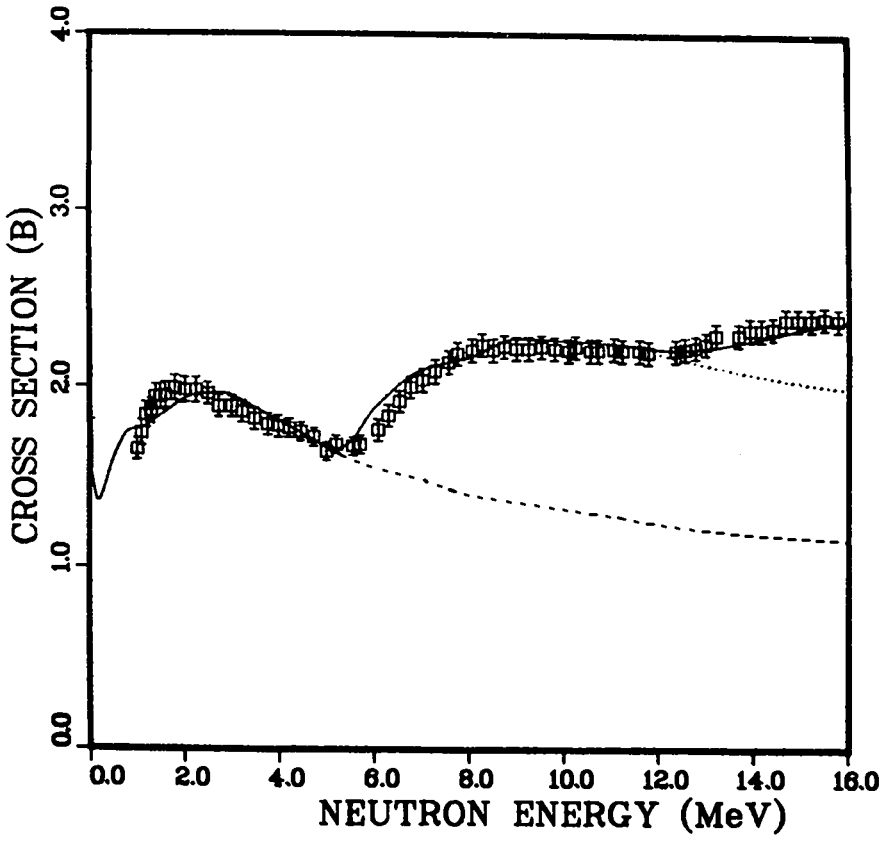

Fig. 16. Our calculation of the $n+^{239}Pu$ total fission cross section (solid curve is compared with the data of Kari et al.[30] The dashed and dotted curves indicate the calculated behavior of the second-chance fission and the second- and third-chance fission sum at higher neutron energies.

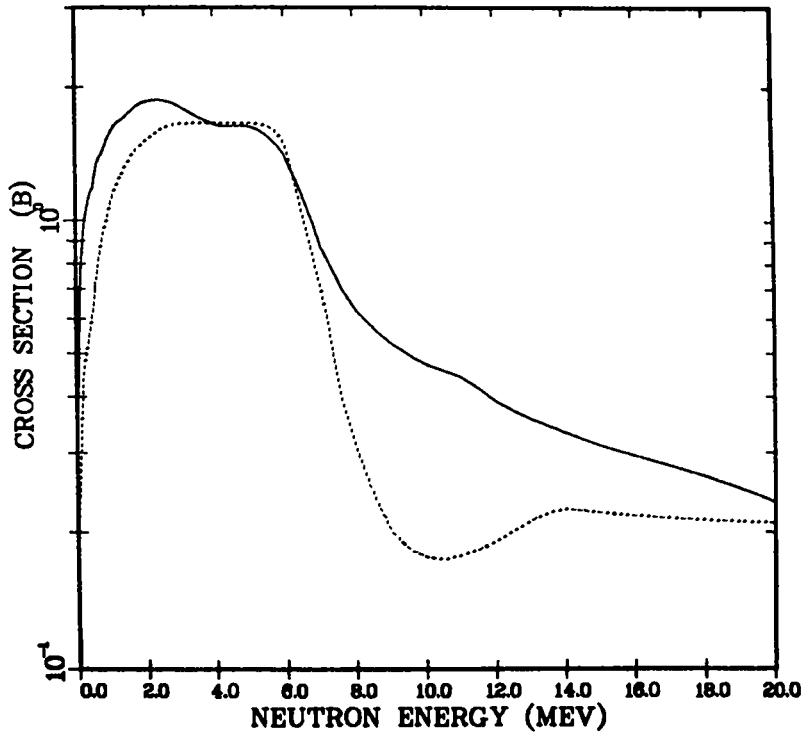

Fig. 17. A comparison of our total calculated inelastic cross section for ^{239}Pu (solid curve) with the evaluated results currently contained in ENDF/B-V.

Other reactions of interest are those involving (n,xn) processes. In our calculations their magnitudes are quite sensitive to the description of the competing fission process occurring for a particular compound nucleus. Thus, for example, the calculated (n,2n) cross sections depend significantly upon the theoretical description of the (n,n'f) competing reaction. In the past, we have achieved good success in the description of the energy behavior of the $^{235}U(n,2n)$ cross section using a somewhat cruder fission model. Even though ^{239}Pu experimental data exist only around 14 MeV, comparison with them provides a measure of the reliability of the calculation. Figure 18 shows the agreement obtained in this instance.

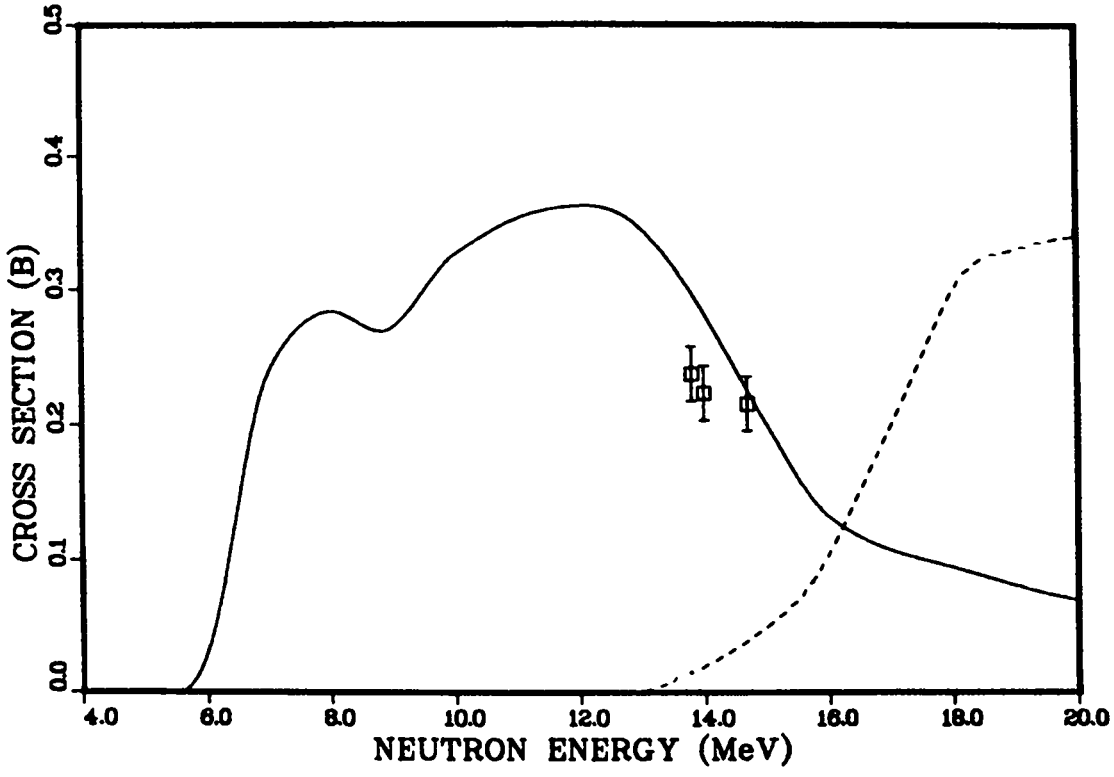

Fig. 18. A comparison of calculated $^{239}Pu(n,2n)$ and (n,3n) cross sections with (n,2n) data available around 14 MeV.*

*R. Lougheed, Lawrence Livermore National Laboratory, provided this data in October 1982.

G. n+^{239}Pu Evaluation for Revision 2 of ENDF/B-V (E. D. Arthur, P. G. Young, R. E. MacFarlane, D. G. Madland)

A major updating of the ENDF/B-V evaluation of neutron-induced reactions on ^{239}Pu was performed in conjunction with issuance of Revision 2 of ENDF/B-V. The primary motivation for updating the ^{239}Pu evaluation was to incorporate results from the theoretical analysis by Arthur (previous article, Sect. F), which corrected serious inconsistencies between ENDF/B-V and the measurements of the total cross section by Poenitz[31] and scattering cross sections by Smith.[32] Additionally, serious discrepancies between the Version V evaluation and new measurements of the prompt fission neutron multiplicity ($\bar{\nu}_p$) by Gwin[33] and by Frehaut[34] were corrected; and the shape of the fission neutron spectrum was changed from a Watt representation to the newly developed Madland-Nix formulation,[35] which gives a more reliable description of the spectra, particularly for secondary neutrons above 10 MeV.

Inclusion of the new theoretical calculations resulted in significant changes in the ^{239}Pu total and inelastic cross sections. Comparisons of the newly evaluated total cross sections with ENDF/B-V (dashed curve) and measurements by Poenitz,[31] Smith,[36] and Schwartz[37] are given in Fig. 19. Changes as large as 7% resulted in the total cross section between 25 and 500 keV.

Similarly, changes of up to a factor of 2 were required in the total inelastic cross section, shown in Fig. 17 of Section F, to correct ENDF/B-V. With the fission cross section for ^{239}Pu left unchanged from ENDF/B-V, the elastic cross section was adjusted to obtain consistency between the new partial and total cross sections. The elastic and inelastic neutron angular distributions from the new calculations were also incorporated into the revised evaluation, together with new inelastic continuum energy and angular distributions.

The $\bar{\nu}_p$ evaluation from ENDF/B-V was revised for incident neutron energies above 0.4 MeV using the experimental data of Gwin[33] and Frehaut.[34] A comparison of the new evaluation with ENDF/B-V (dashed curve) and the experimental data is shown in Fig. 20. The new results are as much as 3% lower than ENDF/B-V in the few-MeV region. Below 0.4 MeV and above 11.5 MeV, the $\bar{\nu}_p$ values were left unchanged from Version V. The ENDF/B-V values at low energy are compared in Fig. 21 with Gwin's measurements.

Because the scope of this work did not permit a thorough reevaluation of neutron-induced fission neutron spectra from ^{239}Pu, an improved shape resulting from the Madland-Nix[35] theory was incorporated by adjusting the level density

parameter in that theory to produce the same average secondary neutron energy for thermal incident neutrons as results from the ENDF/B-V evaluation. The ratio of the new fission neutron spectrum to ENDF/B-V for thermal incident neutrons is shown in Fig. 22. At higher incident energies, the energy dependence given from the theory is included in the first-chance fission neutron spectrum evaluation. The resulting average secondary neutron energies are compared with ENDF/B-V in Fig. 23 up to the second-chance fission threshold.

In summary, significant modifications were made in the total, elastic, inelastic, $\bar{\nu}$, and secondary neutron files for Revision 2 of ENDF/B-V. In addition to correcting several known discrepancies with differential data, the changes are expected to result in substantial improvement in agreement between measured and calculated quantities from integral experiments with the JEZEBEL assembly.

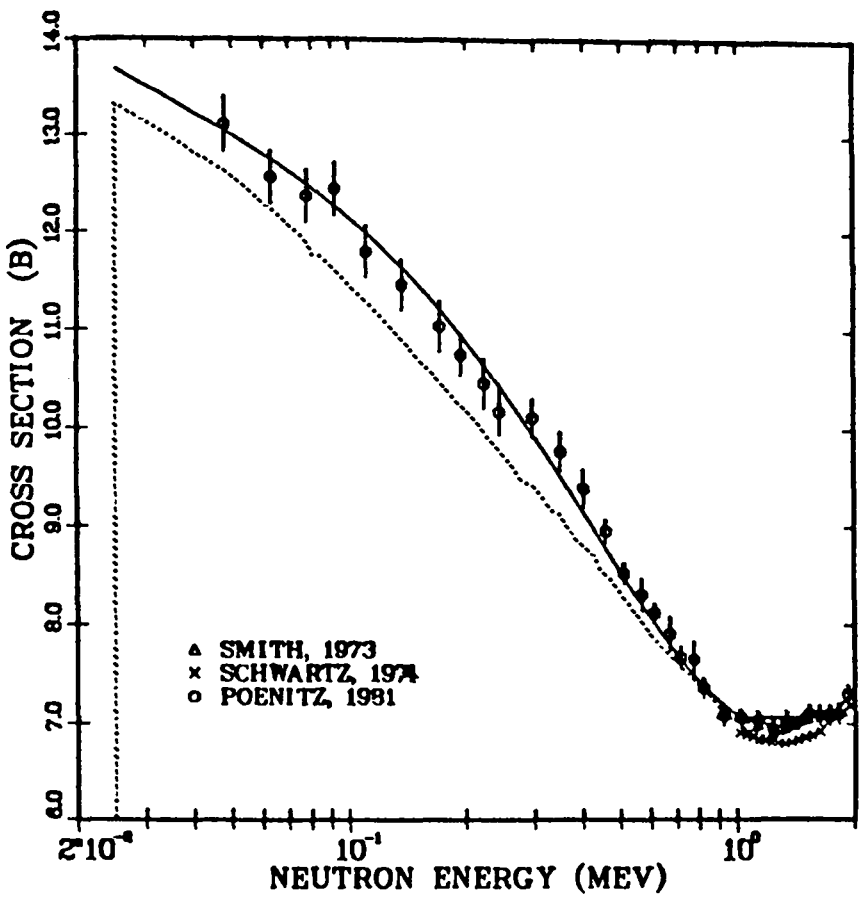

Fig. 19. Measured and evaluated neutron total cross sections of ^{239}Pu for energies between 25 keV and 2.0 MeV. The solid curve is the present evaluation, the dashed curve is ENDF/B-V, and the points represent experimental data.[31, 36, 37] Below 25 keV, the evaluated cross sections are given by resonance parameters and are not described here.

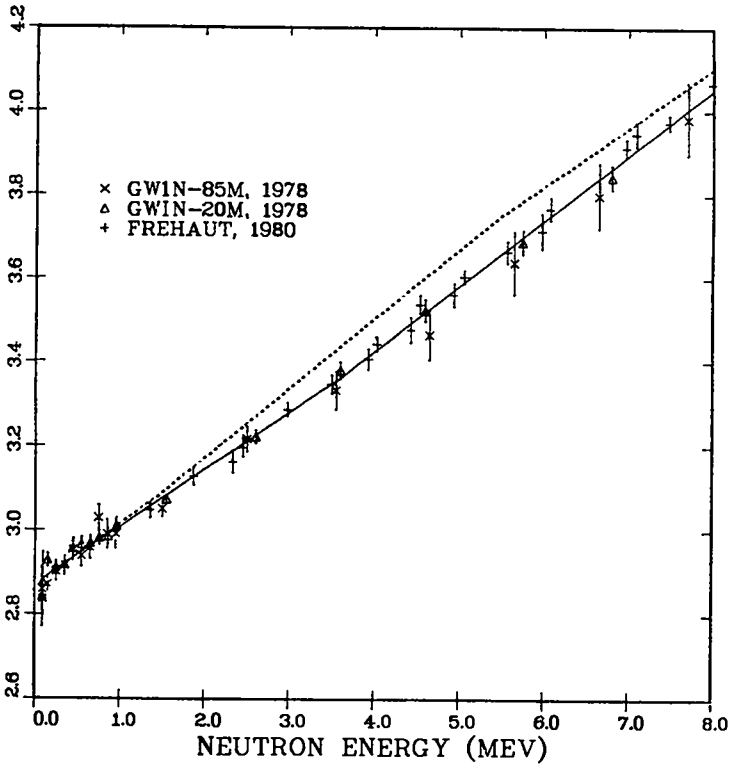

Fig. 20. Measured[33,34] and evaluated values of the prompt neutron multiplicity $\bar{\nu}_p$ for neutron-induced fission of ^{239}Pu. See caption to Fig. 19 for explanation of the curves.

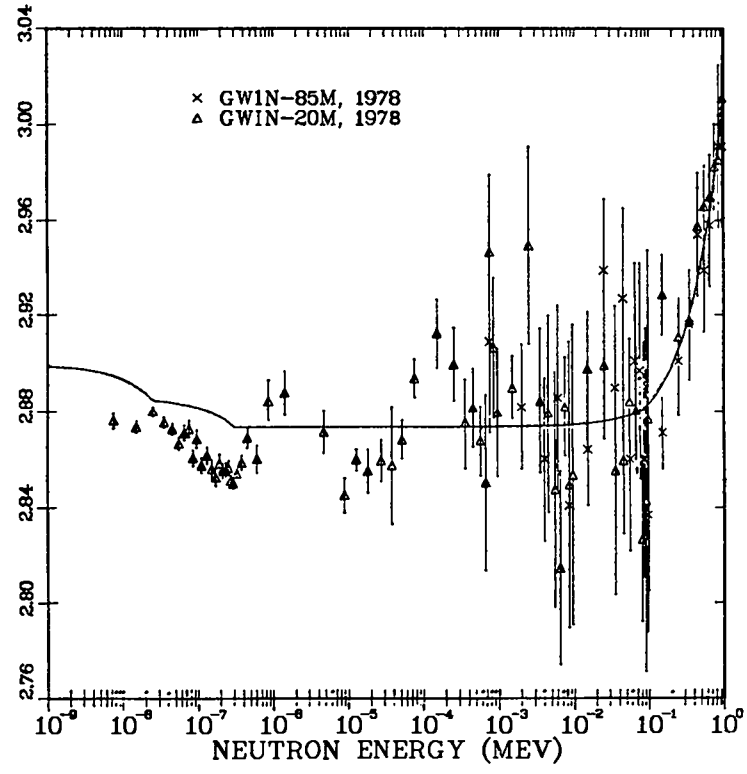

Fig. 21. Measured[33] and evaluated prompt fission neutron multiplicity for ^{239}Pu at low neutron energies. The solid curve represents both ENDF/B-V and the present evaluation below 0.4 MeV.

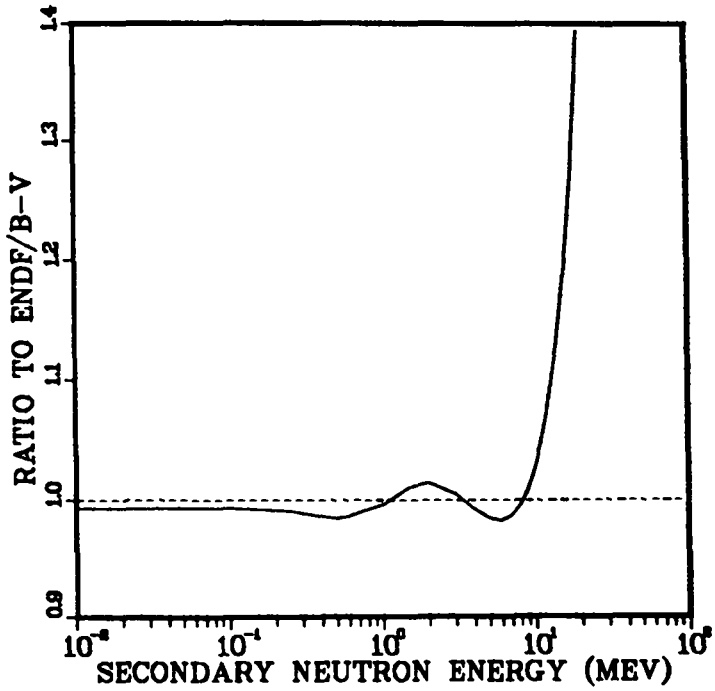

Fig. 22. Ratio of the present evaluated fission neutron spectrum to ENDF/B-V for thermal incident neutrons on ^{239}Pu. The dashed curve indicates a ratio value of unity.

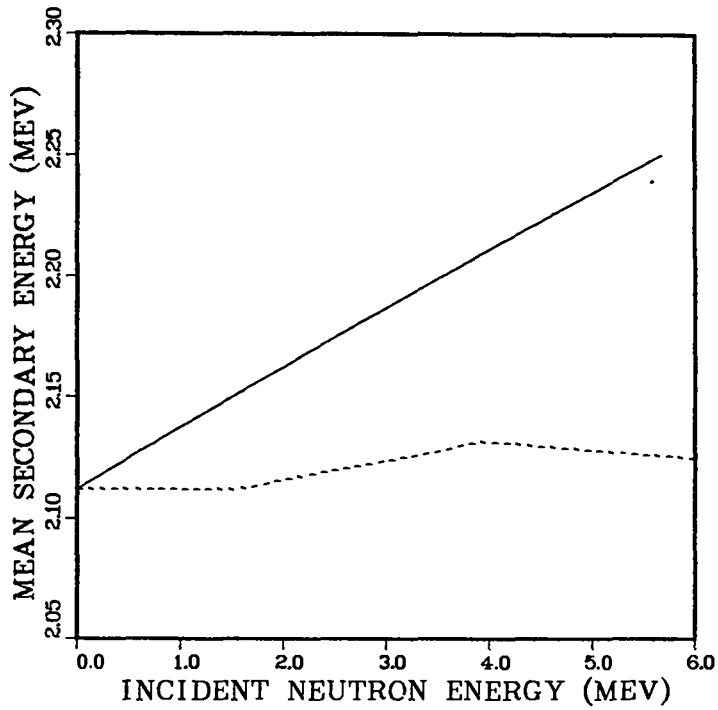

Fig. 23. Average secondary neutron energy from neutron-induced fission of ^{239}Pu as a function of incident neutron energy. The solid curve is the present evaluation and the dashed curve is ENDF/B-V.

H. Cross Sections Calculated Using Microscopic and Other Level-Density Models (E. D. Arthur)

We have made comparisons of cross sections and particle emission spectra that result from Hauser-Feshbach statistical model calculations employing several different level-density formalisms. These were the Gilbert-Cameron,[8] backshifted Fermi-gas,[38] and microscopic Fermi-gas[39] level-density models. Results from this comparison formed the basis for a paper[40] presented at the International Atomic Energy Agency (IAEA) Advisory Group Meeting on Basic and Applied Nuclear Level Densities held recently at Brookhaven National Laboratory.

These three models were chosen because two of them, the Gilbert-Cameron and the backshifted Fermi-gas models, are phenomenological formulations widely used in applied calculations. The third, the microscopic Fermi-gas model, has a more realistic physical basis but has not been generally subjected to the scrutiny that has been applied to the first two in terms of use in nuclear data calculations. Such applied calculations often provide conditions in which cross-section data must be reproduced or predicted for complicated reaction chains over extensive ranges of incident and secondary particle energies.

The Gilbert-Cameron formalism employing the Cook[9] parameters was already an integral part of our Hauser-Feshbach codes, GNASH[11] and COMNUC.[41] To test the other two models, we altered the GNASH code to accept an external file containing state densities and spin cutoff parameters as a function of excitation energy. Spline functions were fitted to these values and were used to determine interpolated densities at the necessary excitation energy occurring in the calculations.

To perform the Fermi-gas microscopic calculations, we modified the code NILSSIG* to write onto disk the state densities and spin cutoff parameter information. The code uses realistic single-particle levels together with a BCS Hamiltonian[42] to determine the state density, $\omega(E)$. The use of the superconductivity formalism includes pairing effects at low excitations and produces state densities having roughly a constant temperature shape. At energies above the transition point, superconductivity effects disappear, and the results return to the Fermi-gas form. The code allows a choice of options for the single-particle levels to be used (Nilsson,[43] Seeger-Perischo,[44] and Seeger-Howard[45]),

*This information was provided by S. Grimes, Ohio University, in 1982.

and produces state densities, spin cutoff parameters, and positive/negative parity ratios as a function of excitation energy.

In our initial application of the level-density models discussed here, we limited ourselves to regions of spherical nuclei, in particular A = 50-60 and A = 90-100. These regions encompass the Z = 28 and N = 50 closed shells and include materials that have been of interest to us previously.[46,47] Nuclei in these regions have varied experimental data applicable to the testing of nuclear level-density models. These include numerous reaction cross-section and particle emission spectra, s-wave (D_0) resonance spacings for several isotopic chains, and direct measurements of level densities up to rather high excitation energies. The availability of D_0 information for several isotopic chains provides a starting point for tests of the microscopic Fermi-gas level-density model. This situation parallels one often found in Hauser-Feshbach calculations of reaction paths involving isotopic chains reached, for example, in (n,2n) and (n,3n) reactions. In such cases large differences in binding energies may exist, along with odd-even effects, that provide stringent conditions under which microscopic-density calculations can be tested. So, for elements ranging from chromium to zinc, we made calculations of the level density occurring at the neutron-binding energy. We used the single-particle levels of Seeger-Perischo[44] and neutron and proton pairing gap values, adjusted to match Gilbert-Cameron data[8] at zero excitation energy. The results of these calculations appear in Table V in which D_0 values are compared with experimentally determined ones.[48] The agreement is very good, generally within a factor of two, which is significant considering the lack of adjustable parameters occurring in this model.

Further tests of this model (along with the Gilbert-Cameron and backshifted Fermi-gas models) appear in Fig. 24 where a comparison is made with directly measured ^{60}Ni level densities available for excitation energies up to around 25 MeV. All three models reproduce the data in a reasonable fashion, although there are shape differences not easily observable in this comparison. These are better illustrated in Fig. 25 where the ratio of the Gilbert-Cameron (dashed curve) and the backshifted Fermi-gas (dotted curve) model results are compared with those obtained from microscopic calculations. All three models were normalized to each other around 11 MeV. The backshifted Fermi-gas results most nearly approximate the microscopic level-density model values, whereas the

differences occurring with the Gilbert-Cameron formalism for energies below 8 MeV can largely be attributed to the constant temperature form employed in this region.

TABLE V

COMPARISON OF S-WAVE RESONANCE SPACINGS CALCULATED USING THE MICROSCOPIC FERMI-GAS LEVEL-DENSITY MODEL WITH EXPERIMENTAL VALUES[14]

Target	<D> (Calculated) (keV)	<D> (Experimental) (keV)	Ratio (C/E)
Cr^{50}	18.8	15 ± 2	1.25
Cr^{52}	41.8	42 ± 5	1.
Cr^{53}	3.8	7.1 ± 1.2	0.54
Cr^{54}	39.4	26 ± 7	1.5
Mn^{55}	0.9	2.7 ± 0.4	0.33
Fe^{54}	38.5	13 ± 2	2.96
Fe^{56}	30.	17 ± 2	1.7
Fe^{57}	4.5	6 ± 1	0.75
Fe^{58}	28.2	35 ± 15	0.8
Co^{59}	0.96	1.1 ± 0.1	0.81
Ni^{58}	19.8	13.7 ± 2	1.4
Ni^{60}	14.9	16 ± 2.5	0.93
Ni^{61}	1.5	1.8 ± 0.3	0.85
Ni^{62}	16.7	19.1 ± 3.6	0.87
Ni^{64}	31.	19.9 ± 3.6	1.3
Cu^{63}	0.26	0.32 ± 0.03	0.81
Cu^{65}	0.48	0.51 ± 0.06	0.95
Zn^{64}	1.02	3.4 ± 0.2	0.29
Zn^{66}	1.9	4.7 ± 0.4	0.4
Zn^{67}	0.21	0.51 ± 0.02	0.42
Zn^{68}	4.2	5.77 ± 0.7	0.73
Zn^{70}	3.3	6.9 ± 1	0.5

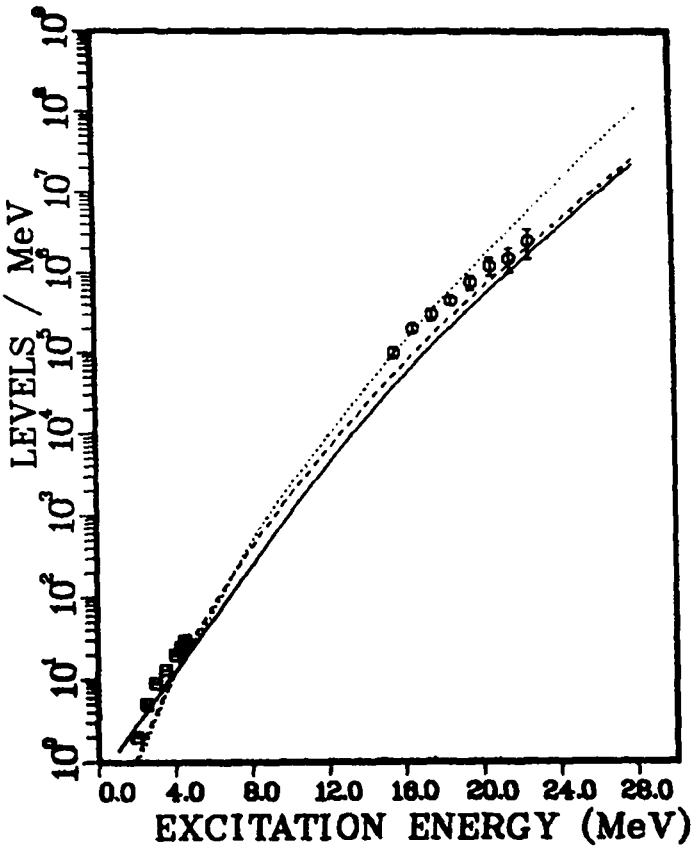

Fig. 24. Comparison of the calculated nuclear level density with experimental data for ^{60}Ni. The solid curve represents the Gilbert-Cameron results; the dashed curve, the backshifted Fermi-gas model; and the dotted curve, microscopic calculations.

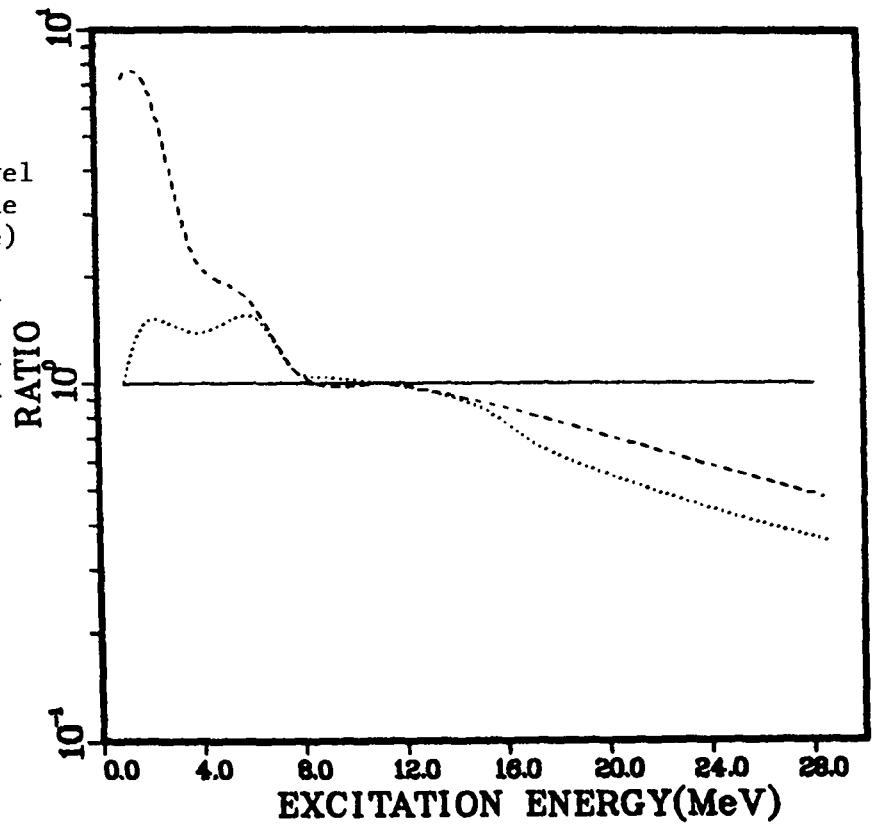

Fig. 25. The ratio of the level densities calculated using the Gilbert-Cameron (dashed curve) and backshifted Fermi-gas (dotted curve) phenomenological models are compared with results from microscopic calculations for ^{60}Ni. All calculations were normalized at 11 MeV.

Further tests of these models, particularly the microscopic Fermi-gas model, were made through their use in the calculation of neutron-induced cross sections and particle emission spectra. Data for channels that are relatively minor constituents of the total reaction cross section can be particularly sensitive to level densities occurring explicitly in that channel or in competing ones. One such example is shown in Fig. 26 in which the calculated proton emission spectra induced by 14.8-MeV neutrons on ^{65}Cu are compared with the data of Grimes et al.[49] The results obtained using the Gilbert-Cameron and microscopic level-density models (solid and dotted curves, respectively) reproduce these data reasonably well in contrast to the overprediction achieved using the backshifted Fermi-gas model. This is traceable to the lower ^{65}Cu level density predicted by this model because residual nuclei occurring in all other major reaction channels (^{65}Ni, ^{64}Ni, ^{64}Cu) have experimental data that can be used to constrain their level-density values. This failure to predict correctly the ^{65}Cu level density produces an underprediction of (n,n'γ) competition so that proton emission from (n,p) and (n,np) reactions is too large. Figure 27 explicitly compares the ^{65}Cu level density calculated using the models discussed here. All three results agree reasonably well at lower excitations. At higher energies that more directly impact the calculated proton emission spectrum, the level-density results diverge with a sizable underprediction occurring for the backshifted Fermi-gas results. This problem appears related to the small value for the Fermi-gas parameter a derived by Dilg et al.[50]

Other data suitable for level-density tests include those providing information concerning the spin cutoff parameter occurring in these models. This information can be inferred from calculations of isomeric state production cross sections or, more directly, from incorporation of discrete level spin data through use of a maximum likelihood estimator. Such an example appears in Fig. 28 where the histogram represents the cutoff parameters deduced directly from ^{98}Mo discrete level data. Curves 1 and 2 are spin cutoff values obtained from the Gilbert-Cameron and backshifted Fermi-gas models. Curve 3 was obtained from microscopic level-density calculations that used the Seeger-Howard[11] single-particle levels.

In summary, we have begun tests of the microscopic Fermi-gas level-density model through direct comparison with s-wave resonance spacing data and with other level-density information measured explicitly. Futhermore, our use of it

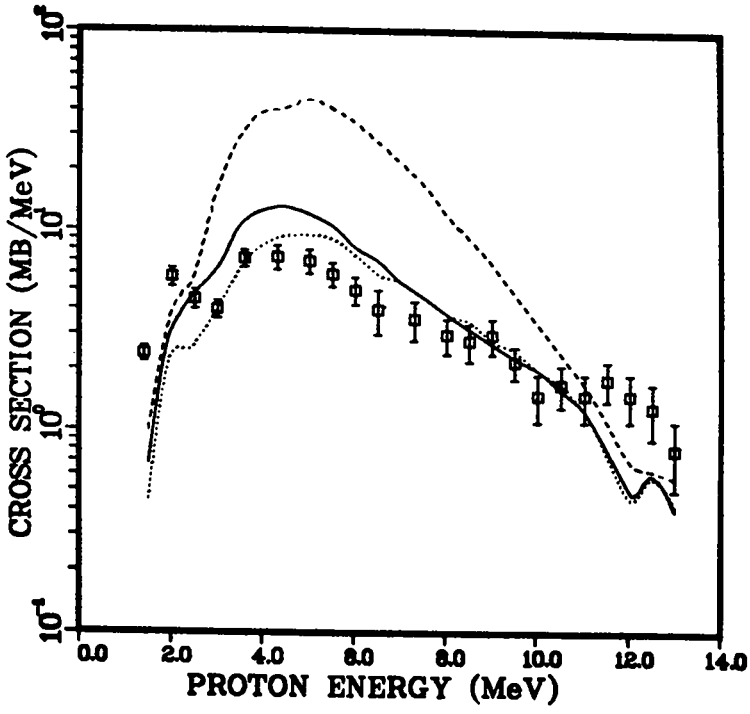

Fig. 26. The calculated proton emission spectra induced by 14.8-MeV neutrons on ^{65}Cu are compared with the data of Grimes et al.[49] The level-density models associated with each curve are identified in Fig. 24.

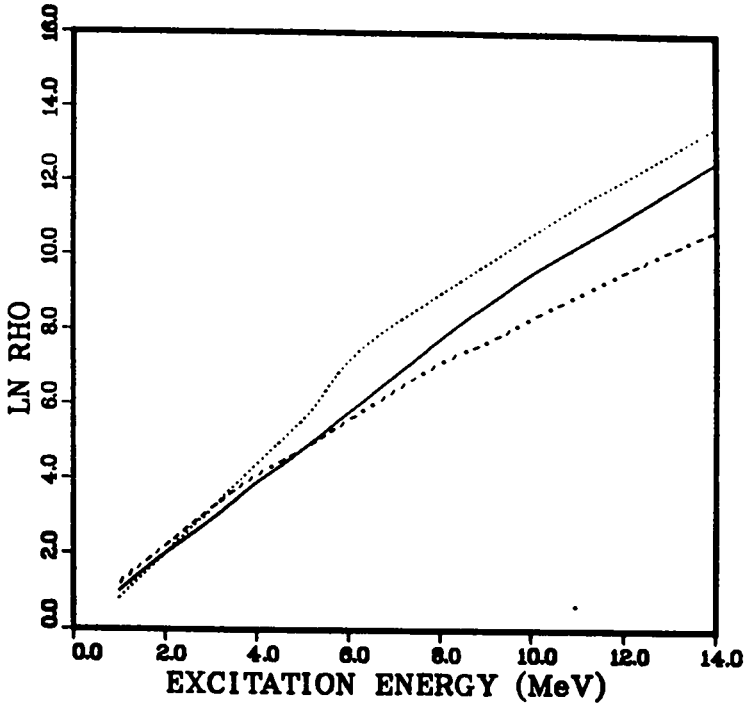

Fig. 27. Calculated level densities for ^{65}Cu. The natural logarithm is shown and the curves are identified as in Fig. 24.

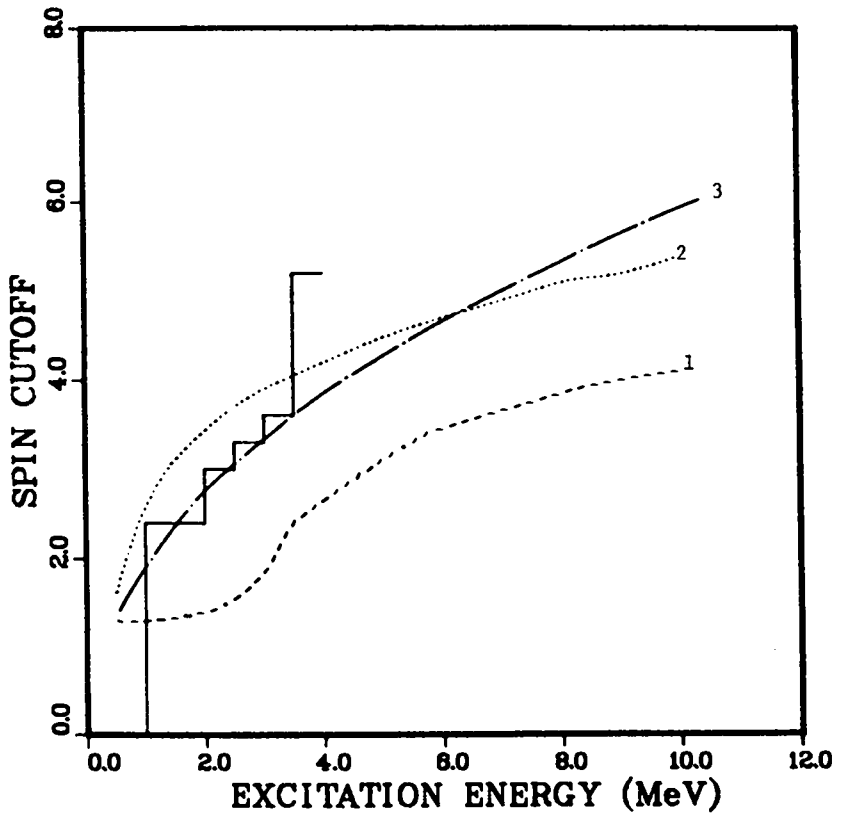

Fig. 28. Spin cutoff parameters calculated for ^{98}Mo are compared with the histogram that was determined from discrete level data. The curves labeled 1 and 2 represent the Gilbert-Cameron and backshifted Fermi-gas models, while Curve 3 was obtained from the microscopic model described in the text.

in Hauser-Feshbach calculations of cross sections and emission spectra provides an expanded basis sensitive to level-density effects, not only around the neutron-binding energy but at other excitation energies as well. Generally these initial tests have resulted in good agreement when this microscopic model was used. There are, however, some indications of problems that could affect routine application in our Hauser-Feshbach calculations. One such example appears in Fig. 29 where the level density of ^{60}Co that one might employ in ^{60}Ni(n,p) calculations is shown. The solid curve results from the Gilbert-Cameron model, whereas the dashed curve was obtained from microscopic calculations that used the Seeger-Perischo[11] single-particle levels. Both calculations reproduce experimental D_0 values (D_0 = 1.1 keV) well at the neutron binding energy, but the microscopic results, when extrapolated to lower excitation energies, lie significantly above the Gilbert-Cameron values, as well as those inferred from discrete level data. This, in turn, produces calculated ^{60}Ni(n,p) cross sections that substantially overpredict experimental results. Efforts to

lower the microscopic results in this excitation energy region by adjustment of proton and neutron pairing gaps were not successful, probably due to the odd-odd nature of the ^{60}Co nucleus. This example illustrates a potential problem that can occur in the use of microscopic level densities in applied calculations in which the flexibility to adjust the level density to reproduce relevant experimental data is not available.

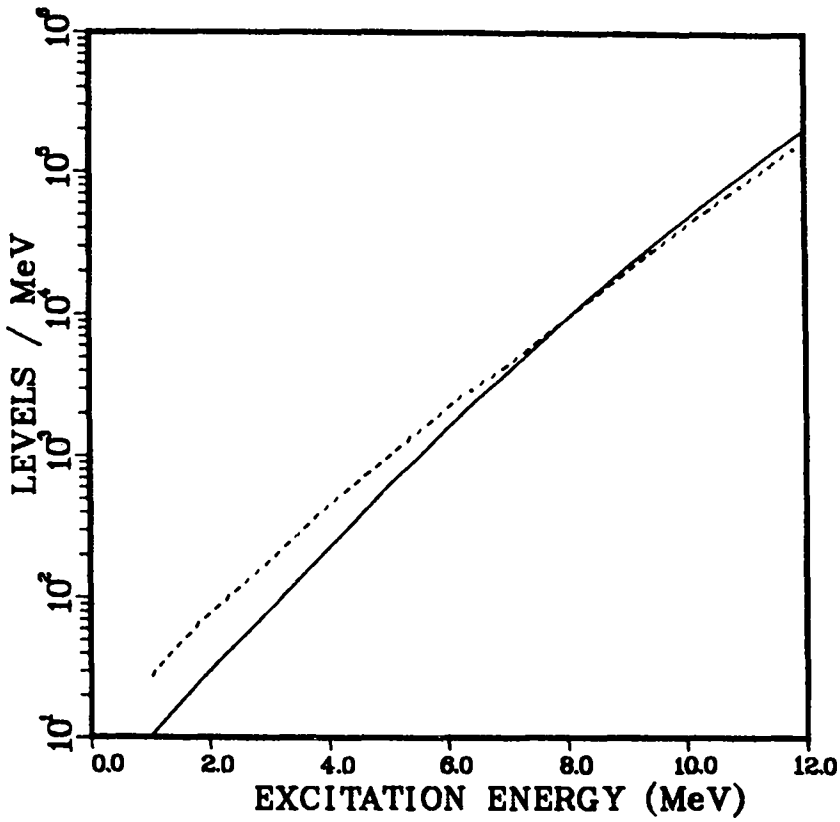

Fig. 29. Level densities calculated for ^{60}Co. The solid curve was obtained from the Gilbert-Cameron level-density model and includes both constant temperature and Fermi-gas contributions. The dashed curve results from microscopic calculations made using the Seeger-Perischo single-particle levels.[44]

I. Addition of Gamma-Ray Production Data to the ENDF/B-V ^{197}Au Evaluation

(P. G. Young and E. D. Arthur)

The ENDF/B-V evaluation[51] of neutron-induced reactions on ^{197}Au was modified to include gamma-ray production data. The revision is based primarily on the experimental data of Orphan et al.[52] for thermal incident neutrons and the measurements of Morgan and Newman[53] from 0.2 to 20 MeV. Theoretical calculations with the GNASH code[11] were used in the range of 10 to 800 keV to supplement the Morgan data. The evaluated gamma-ray-production data were put into ENDF/B format and combined with the ENDF/B-V Au evaluation.

Neutron transmission coefficients for the GNASH calculations were obtained using the spherical optical model parameters of Delaroche et al.[54] Discrete level information for ^{197}Au and ^{198}Au was taken from the compilations of Harmatz.[55,56] The level-density formulation and parameters of Gilbert and Cameron[8] were employed, with pairing and shell corrections from Cook.[9] A giant dipole resonance model[19,20] was used to calculate gamma-ray strength functions, with a 75% step reduction in the shape below 4 MeV required to match Morgan's[53] spectra below an incident energy of 1 MeV. A similar step was required in calculations of a gamma-ray strength function for thermal incident neutrons by Gardner.[57]

At low energies the gamma-ray spectral shape measured by Orphan et al.[52] was used in the evaluation, with the lowest secondary energy group (E_γ = 0-375 keV) adjusted to match Gardner's calculations. Energy conservation was used to obtain the gamma-ray multiplicity up to the inelastic neutron threshold at E_n = 78 keV.

Calculated absolute spectra were employed between 10 and 800 keV. These results joined reasonably smoothly onto the experimental results of Morgan and Newman[3] at higher energies. The calculated spectrum at 800 keV is compared with the experimental data in Fig. 30. At energies above 800 keV, the absolute gamma-ray production cross sections and shapes from Morgan's experiment were used directly in the evaluation.

Because no effort was made to ensure consistency between the neutron and gamma-ray files, total energy conservation is not built into the evaluation. For this reason, the revised evaluation is regarded as interim until we can complete a thorough analysis of all the nuclear data available.

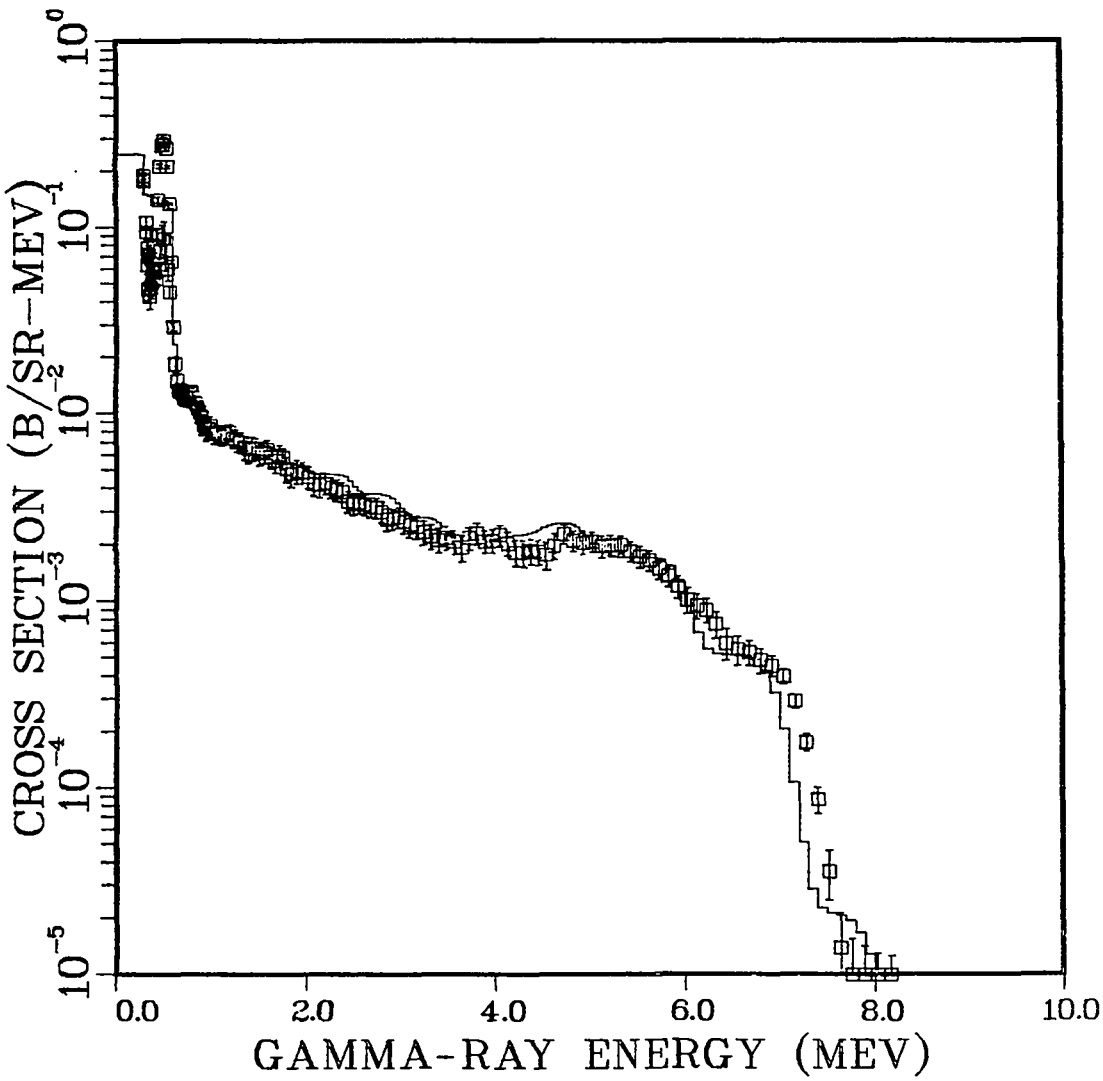

Fig. 30. Measured[53] and calculated absolute ^{197}Au gamma-ray production spectra for incident neutrons in the energy range 0.6-1.0 MeV.

J. Control Materials and Light Coolant Cross-Section Data (P. G. Young and L. Stewart)

The status of nuclear cross-section data for fission reactor control and light coolant materials is reviewed in an article submitted to Progress in Nuclear Energy, with particular emphasis on Version V of the U. S. Evaluated Nuclear Data File (ENDF/B-V). Under control materials, the neutron-induced reactions on ^{10}B and ^{11}B are highlighted, covering the energy range from thermal to 20 MeV. The status of radiative capture data for Ag, In, Cd, Gd, and Hf isotopes in the thermal and resonance regions is also included. Under coolants and moderating materials, the nuclear data for H, D, He, C, and O are reviewed, as well as the ENDF/B-V thermal data for H_2O, D_2O, and graphite. Comparisons

between evaluated results and both recent and older experimental data are given in all cases. Assessments are made of the adequacy of the data for reactor applications, and recommendations for needed improvements in the data are presented.

The most significant data problems uncovered in the review occur for the ENDF/B-V evaluation[58] of ^{11}B. This evaluation actually dates back to Version III of ENDF/B, which in turn is based on a modification of the then existing United Kingdom Atomic Energy Agency ^{11}B evaluation. Significant new experimental data have become available since that time, and there is an urgent need to update the ENDF/B-V file.

In addition to not containing gamma-ray production or covariance data files, certain of the evaluated neutron cross sections are also seriously discrepant with newer data. Figure 31 illustrates one of the more serious discrepancies in which the ENDF/B-V[58] evaluated total cross section differs from experiment[59-64] by 20-40% near 1 and 2.5 MeV and is systematically ≅ 10%

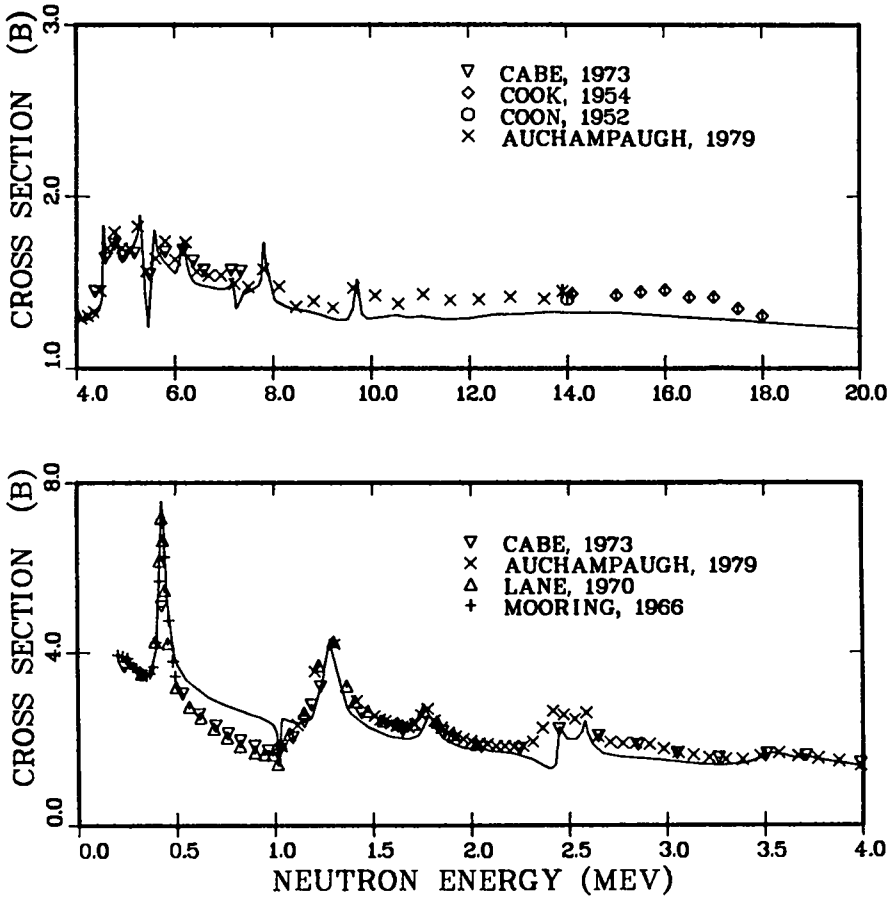

Fig. 31. Neutron total cross sections of ^{11}B from 0.2 to 20 MeV.

lower than the measured data above 9 MeV. These same problems can be seen in comparisons of the evaluated and measured[60,65-73] elastic cross section over the same energy range, given in Fig. 32. Finally, discrepancies of the order of 50% to a factor of 2 are seen in Fig. 33, in which comparisons of measured[71-74] and evaluated elastic angular distributions between 9 and 14 MeV are given. Here the difference is nearly a factor of 3 at back angles for 14-MeV incident neutrons.

In addition to the ^{11}B discrepancies, the article also notes serious problems in the ^{10}B, In, and thermal neutron data evaluations in ENDF/B-V. Somewhat lower priority problems are also discussed for the Version V evaluations of ^{2}H, ^{16}O, Cd, $^{152,154}Gd$, and $^{174,176,178,179}Hf$.

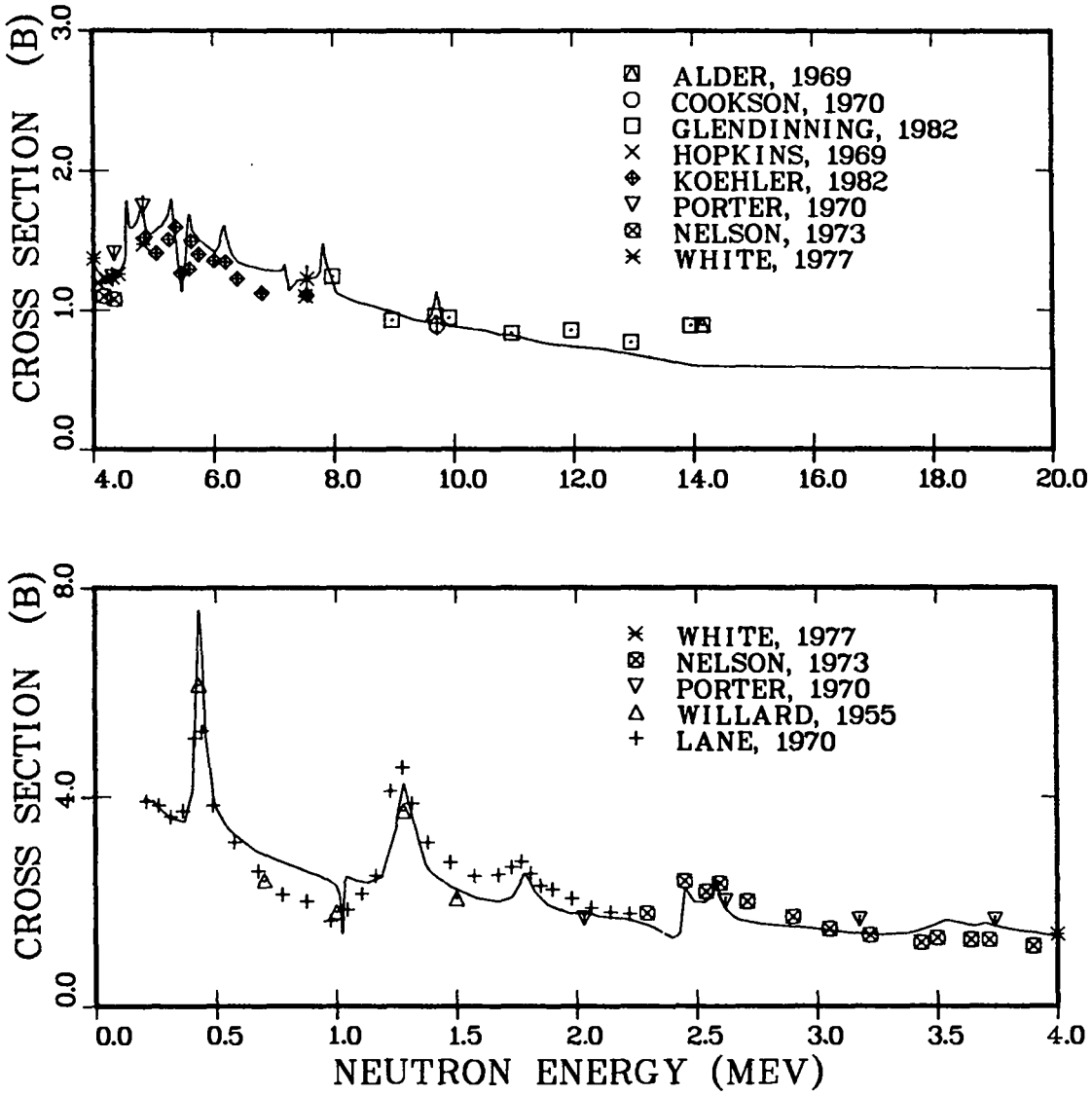

Fig. 32. Elastic neutron cross section for ^{11}B from 0.2 to 20 MeV.

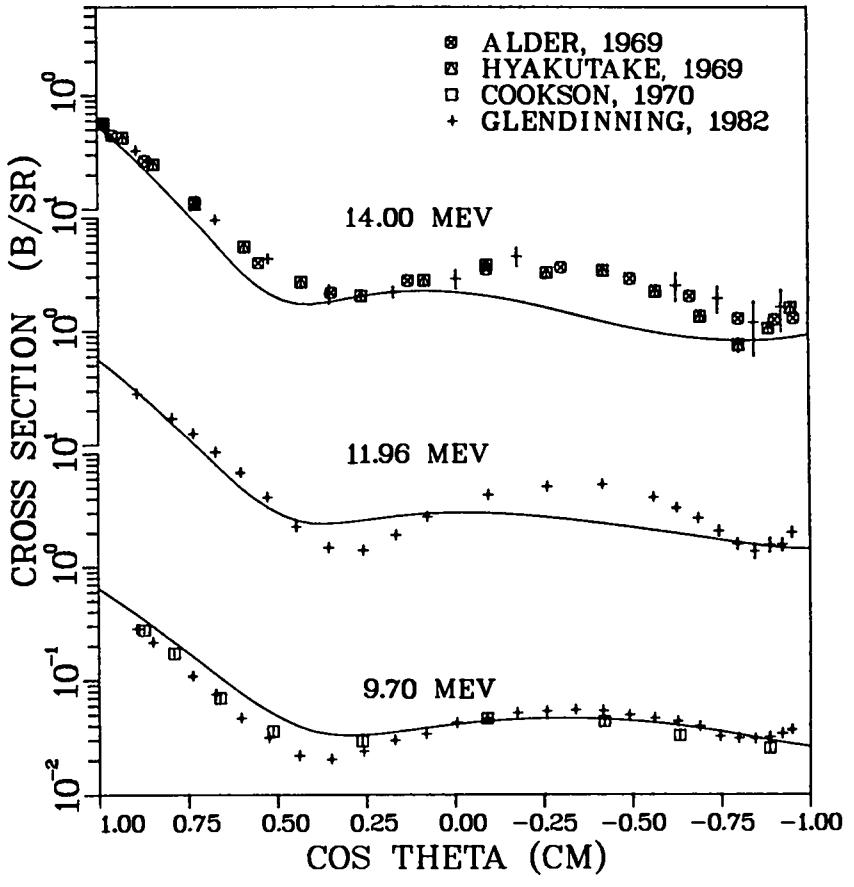

Fig. 33. Measured and evaluated elastic neutron angular distributions for ^{11}B at 9.7, 11.96, and 14.0 MeV.

K. Calculation of Excited-State Cross Sections for ^{169}Tm (D. G. Madland)

Preliminary coupled-channel and Hauser-Feshbach statistical-model calculations have been performed for the scattering of neutrons by ^{169}Tm, with the target nucleus existing in the ground state and in the first-excited state.

The coupled-channel calculations were performed using the code JUPXST (Ref. 26, pp. 28-30) to obtain the total, shape elastic, reaction, direct inelastic, and compound-nucleus formation cross sections, together with the corresponding compacted transmission coefficients $T(n,\ell,j)$, as a function of incident neutron energy over the range 1 keV to 20 MeV.

Pertinent details of the calculations are as follows. The coupled-channel potential of Young et al.[75] was used throughout. In particular, the first-excited state calculations were carried out by use of this potential together with an energy transformation that is determined from reciprocity. The de-

formation parameters of the potential are $\beta_2 = 0.31$ and $\beta_4 = -0.01$. The expansion order of the complex form factor used in JUPXST is $\lambda = 8$ (Legendre polynomial P_8). A matching radius of 13.8 F was chosen; and the algorithm for the maximum projectile orbital angular momentum, ℓ_{max}, is $\ell_{max} + 1 = 2.5\ (kR + 1) + I_{max}$, where k is the neutron wave number, R is the nuclear radius, and I_{max} is the maximum spin occurring (9/2) in the set of coupled states. The first five members of the ground-state band were included in the calculations for both target states.

Results from the coupled-channel calculations are illustrated in Figs. 34 through 37 where comparisons of ground-state and first-excited-state cross sections are made. Considering the few-MeV region, one observes that the total cross section for the target in the first-excited state is first smaller and then larger, with increasing neutron energy, compared with that for the target in the ground state. In this same region the elastic cross section is smaller and the compound-nucleus formation cross section is larger for scattering from the first-excited state. The direct-summed inelastic-scattering cross section, shown in Fig. 36, is almost always smaller for scattering from the target in the first-excited state. These effects are summarized quantitatively in Table VI for incident neutron energies of 10 keV, 100 keV, 1 MeV, and 5 MeV.

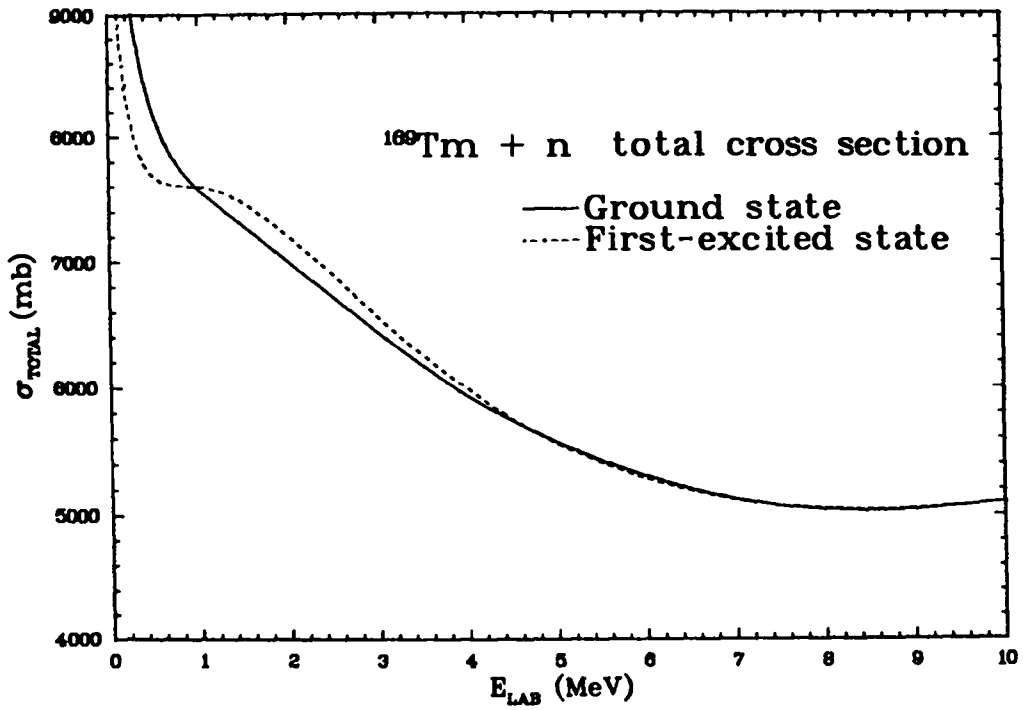

Fig. 34. Total cross section for the scattering of neutrons by ^{169}Tm in the $1/2^+$ 0.00 ground state and in the $3/2^+$ 0.00841 first-excited state, as a function of the incident neutron energy.

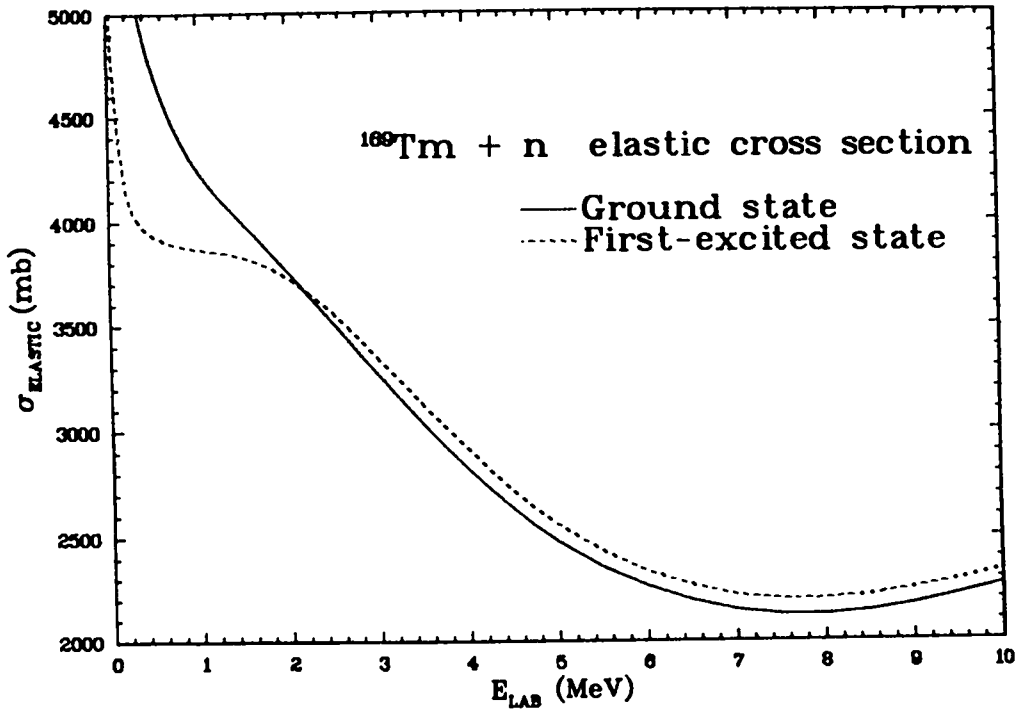

Fig. 35. Elastic cross section for the scattering of neutrons by ^{169}Tm in target states identical to those of Fig. 34.

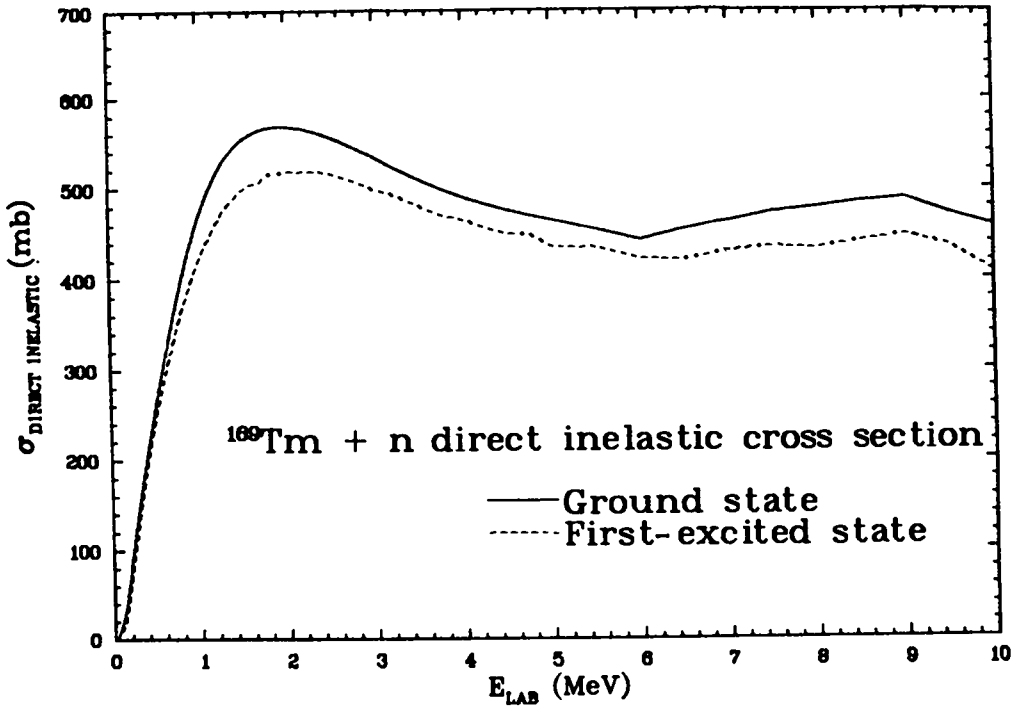

Fig. 36. Direct inelastic cross section for the scattering of neutrons by ^{169}Tm in target states identical to those of Fig. 34. Note that the absorptive part of the coupled-channel optical potential used in the calculations is only piecewise continuous at neutron energies of 6 and 9 MeV.

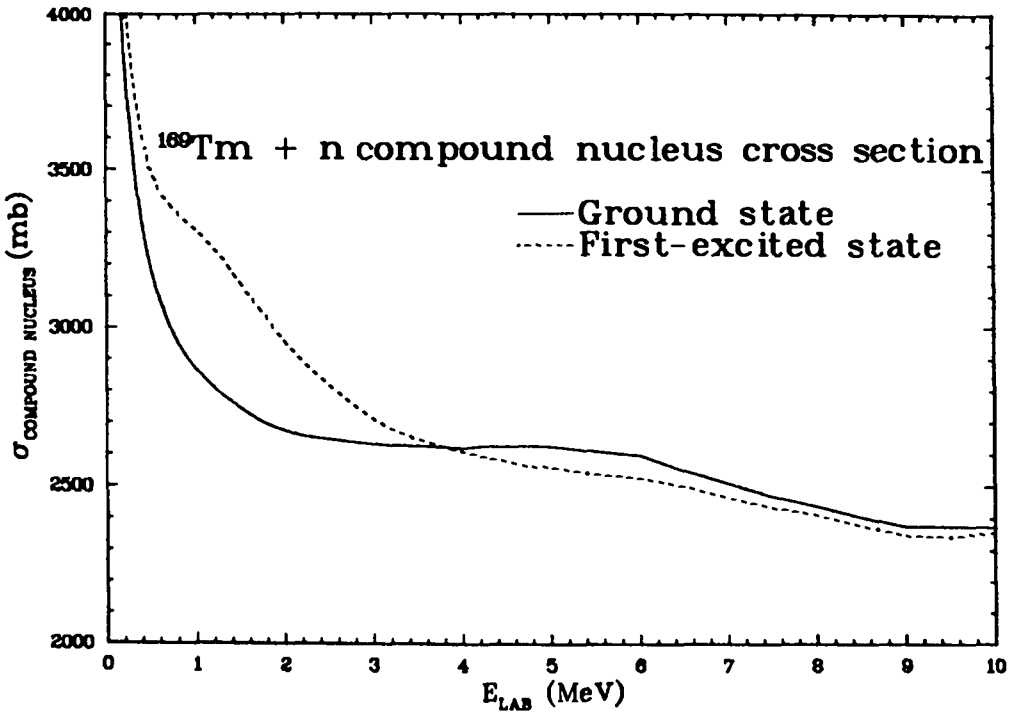

Fig. 37. Compound-nucleus formation cross section for the scattering of neutrons by ^{169}Tm in target states identical to those of Fig. 34.

TABLE VI

NEUTRON CROSS-SECTION COMPARISONS FOR ^{169}Tm

Incident Neutron Energy = 10 keV

Cross Section	Ground State (mb)	1st-Excited State (mb)	Difference (%)
Total	14877	13975	-6.1
Elastic	7070	5234	-26.0
Reaction	7807	8741	12.0
Comp. Nuc.	7807	8740	12.0
Total Inel.	697	907	30.1
Capture	2146	2817	31.3

Incident Neutron Energy = 100 keV

Cross Section	Ground State (mb)	1st-Excited State (mb)	Difference (%)
Total	10282	8978	-12.7
Elastic	5905	4448	-24.7
Reaction	4377	4530	3.5
Comp. Nuc.	4354	4516	3.7
Total Inel.	1166	650	-44.3
Capture	625	941	50.6

TABLE VI (Cont.)

NEUTRON CROSS-SECTION COMPARISONS FOR ^{169}Tm

Incident Neutron Energy = 1 MeV

Cross Section	Ground State (mb)	1st-Excited State (mb)	Difference (%)
Total	7577	7595	0.2
Elastic	4240	3866	-8.8
Reaction	3337	3729	11.7
Comp. Nuc.	2869	3310	15.4
Total Inel.	2775	3088	11.3
Capture	140	154	10.0

Incident Neutron Energy = 5 MeV

Cross Section	Ground State (mb)	1st-Excited State (mb)	Difference (%)
Total	5569	5556	-0.2
Elastic	2479	2559	3.2
Reaction	3090	2997	-3.0
Comp. Nuc.	2626	2562	-2.4
Total Inel.	3065	2975	-2.9
Capture	9	8	-11.1

The Hauser-Feshbach statistical-model calculations were performed using the code COMNUC[76] to obtain the compound elastic, compound inelastic, and capture cross sections as a function of incident neutron energy over the range 1 keV to 8 MeV where the (n,2n) reaction channel opens. The compacted coupled-channel transmission coefficient sets $T(n,\ell,j)$ for ground-state and first-excited-state scattering described above were used in the calculations. The capture cross section was calculated in the Brink-Axel giant dipole model approximation for the gamma transmission coefficient. A value of $2\pi\langle\Gamma_\gamma\rangle/\langle D\rangle$ = 0.07953 was used and 27 discrete capture states were included. No direct capture component was calculated.

Results from the statistical-model calculations are illustrated in Figs. 38 and 39 and are given quantitatively in Table VI for four incident neutron energies. The total inelastic-scattering (direct plus compound) cross section is shown in Fig. 38 for the target in the ground state and in the first-excited state. One observes, in the first-excited-state case, an "accelerator" cross section varying from ~ 3.5 barns to ~ 0.6 barns as the neutron energy increases from 1 keV to 109.8 keV, the excitation energy of the $5/2^+$ state relative to

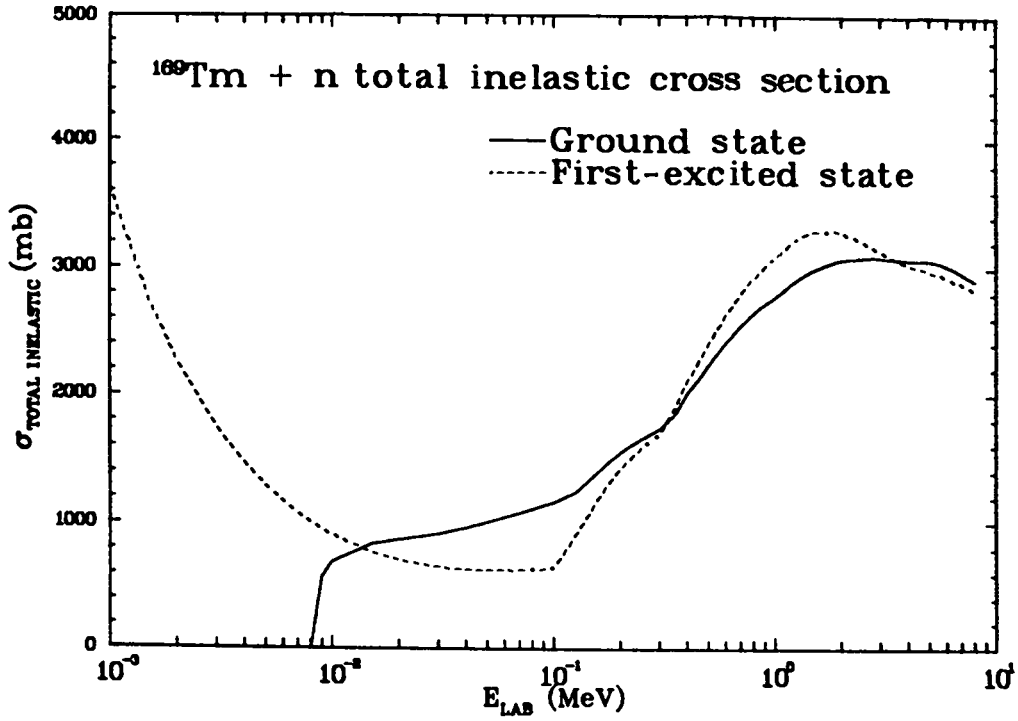

Fig. 38. Total inelastic cross section (direct plus compound) for the scattering of neutrons by ^{169}Tm in target states identical to those of Fig. 34.

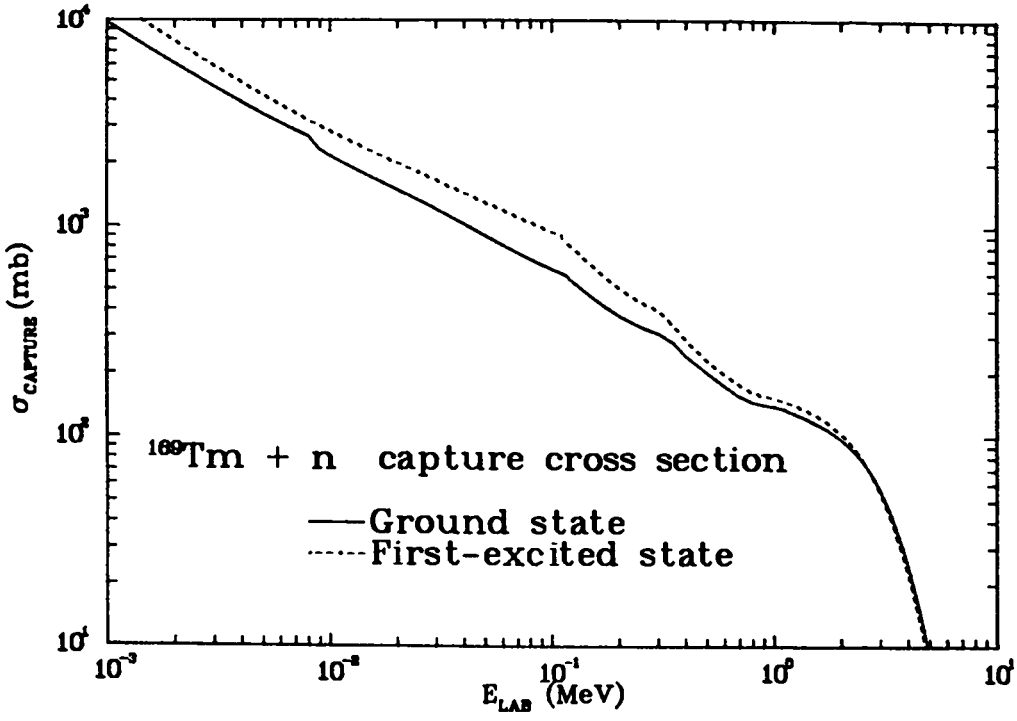

Fig. 39. Capture cross section for the scattering of neutrons by ^{169}Tm in target states identical to those of Fig. 34.

that of the $3/2^+$ state. The "accelerator" cross section is just the inelastic transition from the $3/2^+$ target state to the $1/2^+$ true ground state, in which the neutron gains the energy of the transition. The "accelerator" cross section exists for all neutron energies, but it is the only allowed inelastic transition for $E_n < 109.8$ keV in the first-excited-state target case. One also observes in Fig. 38 that the thresholds for exciting successively higher lying states in inelastic scattering always differ by the same amount, 8.41 keV, in comparing corresponding thresholds for ground-state and first-excited-state target scattering. This is, of course, because the excitation energy difference between the two target states is 8.41 keV.

The capture cross sections are shown in Fig. 39. Here, the capture cross section from the target in the first-excited state dominates that from the target in the ground state over most of the energy range considered. One also observes the 8.41-keV shift in the thresholds of corresponding inelastic scattering transitions, described above, which are seen here via competition with inelastic scattering.

One of the most interesting aspects of studying the total inelastic and capture cross sections in ground-state and first-excited-state target configurations is that the magnitudes of these cross sections can be quite different for the two configurations, when at the same time the magnitudes of the corresponding compound-nucleus formation cross sections are almost the same. As Table VI shows for $E_n = 100$ keV, the compound-nucleus formation cross sections differ by 3.7%, while the total inelastic and capture cross sections differ by -44.3% and 50.6%, respectively. Thus, it is not correct to assume that nearly equal compound-nucleus formation cross sections imply nearly equal components of the compound-nucleus formation cross sections.

L. Calculation of Excited-State Cross Sections for Actinide Nuclei (D. G. Madland)

Coupled-channel calculations have been performed for the scattering of neutrons by ^{238}U and ^{239}Pu, with these targets existing in the ground state and in the first-excited state. The calculations were performed using the code JUPXST (see Ref. 26, pp. 28-30). The total, shape elastic, reaction, direct inelastic, and compound-nucleus formation cross sections were calculated, together with the corresponding compacted transmission coefficients $T(n,\ell,j)$, as a function of incident neutron energy over the range 10 keV to 10 MeV. The

resulting transmission coefficient sets, for both ground-state and first-excited-state cases, will be used in Hauser-Feshbach statistical-model calculations.

Pertinent details of the calculations are as follows. The actinide coupled-channel potential of Madland and Young[77] was used throughout. In particular, the first-excited-state calculations were carried out by use of this potential together with an energy transformation that is determined from reciprocity. The deformation parameters used for ^{238}U are $\beta_2 = 0.200$ and $\beta_4 = 0.058$, from Ref. 77, and those used for ^{239}Pu are $\beta_2 = 0.220$ and $\beta_4 = 0.070$, from Ref. 78. The expansion order of the complex form factor used in JUPXST is $\lambda = 8$ (Legendre polynomial P_8). A matching radius of 14.0 F was chosen and the algorithm for the maximum projectile orbital angular momentum, ℓ_{max}, is $\ell_{max} + 1 = 2.5(kR + 1) + I_{max}$, where k is the neutron wave number, R is the nuclear radius, and I_{max} is the maximum spin occurring in the set of coupled states. In the case of ^{238}U, three states of the ground band were coupled with $I_{max} = 4$, whereas in the case of ^{239}Pu, five states of the ground band were coupled with $I_{max} = 9/2$.

Results from the calculations are illustrated in Figs. 40 through 47, where comparisons of ground-state and first-excited-state cross sections are made for both ^{238}U and ^{239}Pu. Considering the few-MeV region, one observes that the total and compound-nucleus formation cross sections are smaller if the target nuclei are in the first-excited state instead of the (usual) ground state, whereas the elastic cross sections are larger. The summed direct inelastic-scattering cross sections are smaller for the target nuclei in the first-excited state over most of the energy range considered. Perhaps the most interesting curves are those of compound nucleus formation shown in Figs. 46 and 47. These indicate, in the few-MeV region, that the combined compound elastic, compound inelastic, capture, and fission cross sections are approximately 10 to 15% less for the two target nuclei in the first-excited state compared with being in the ground state. This result was also obtained in the early JUPXST test calculations[79] for the case of ^{238}U. Thus, the fission cross sections for ^{238}U and ^{239}Pu in their first-excited states may be somewhat less than the corresponding fission cross sections for these nuclei in their ground states. We intend to test this supposition using the calculated transmission coefficient sets $T(n,\ell,j)$ in statistical-model calculations of the cross sections for fission and competing reactions.

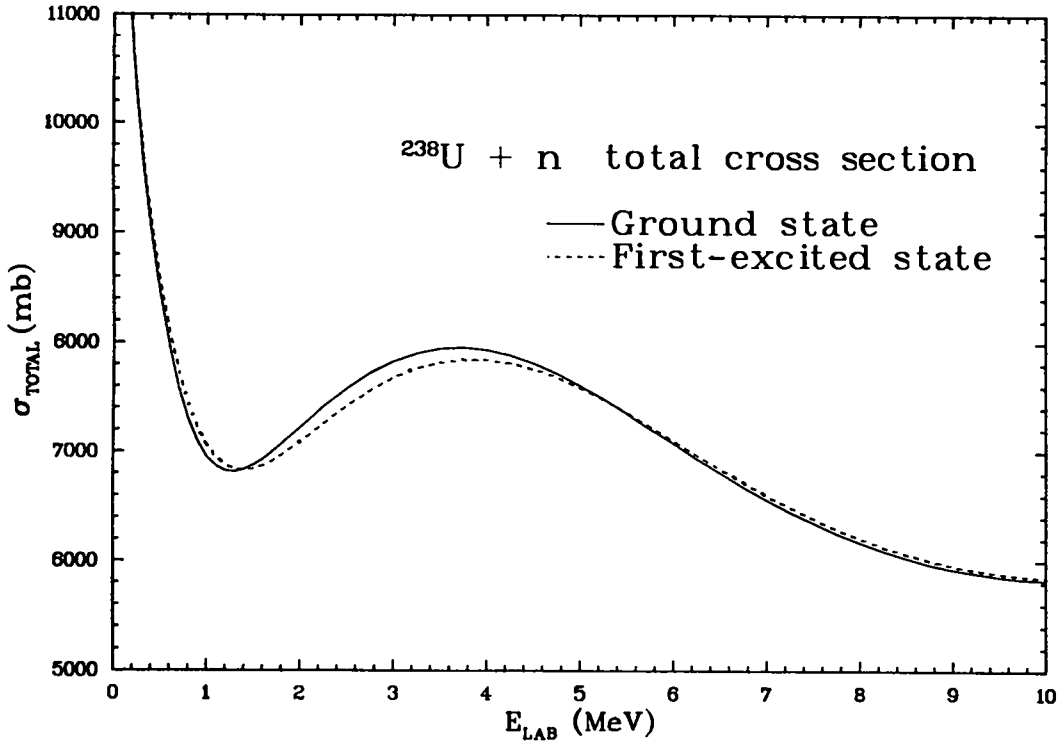

Fig. 40. Total cross section for the scattering of neutrons by ^{238}U in the 0^+ 0.00 ground state and in the 2^+ 0.0449 first-excited state, as a function of the incident neutron energy.

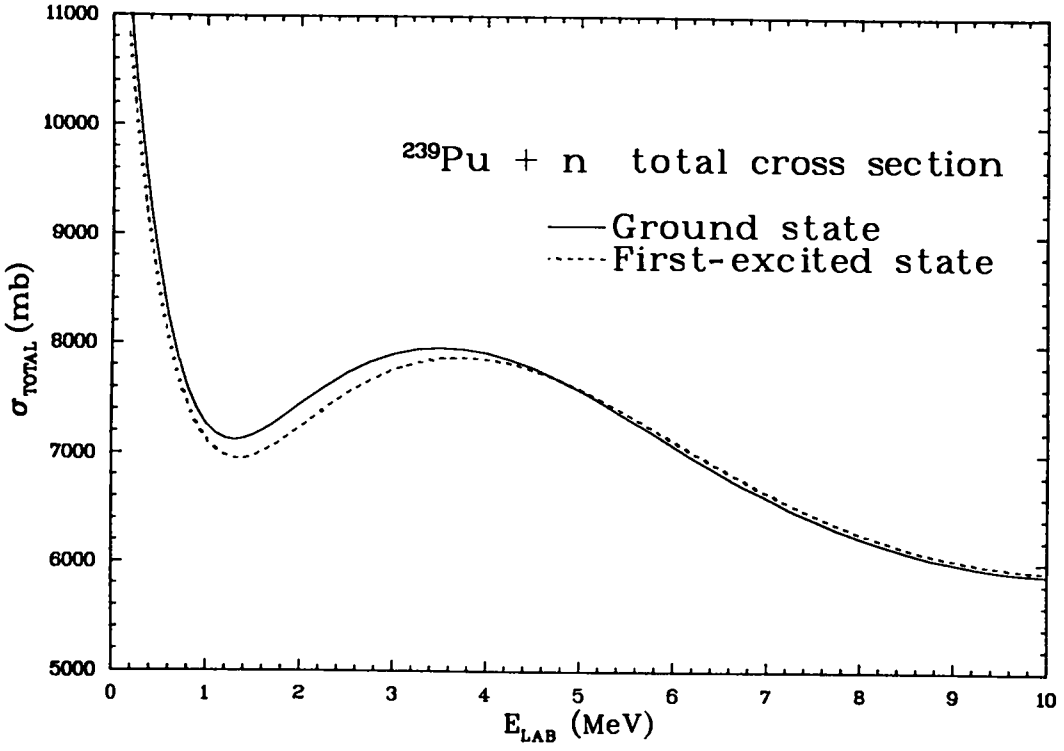

Fig. 41. Total cross section for the scattering of neutrons by ^{239}Pu in the $1/2^+$ 0.00 ground state and in the $3/2^+$ 0.00786 first-excited state, as a function of the incident neutron energy.

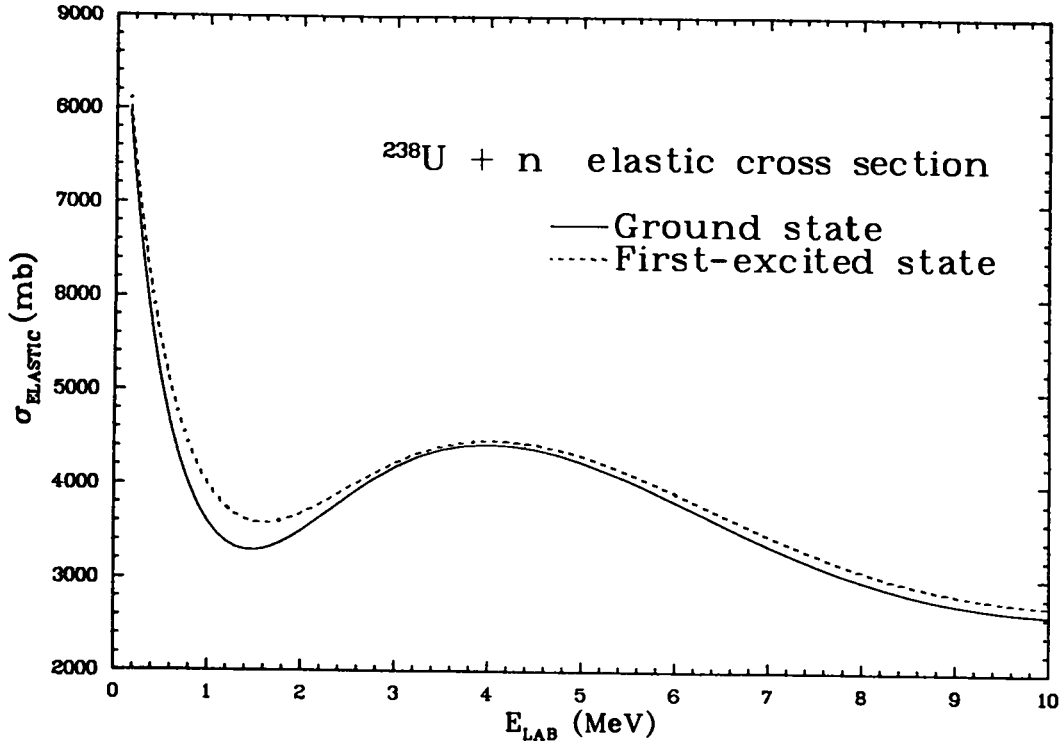

Fig. 42. Elastic cross section for the scattering of neutrons by ^{238}U in target states identical to those of Fig. 40.

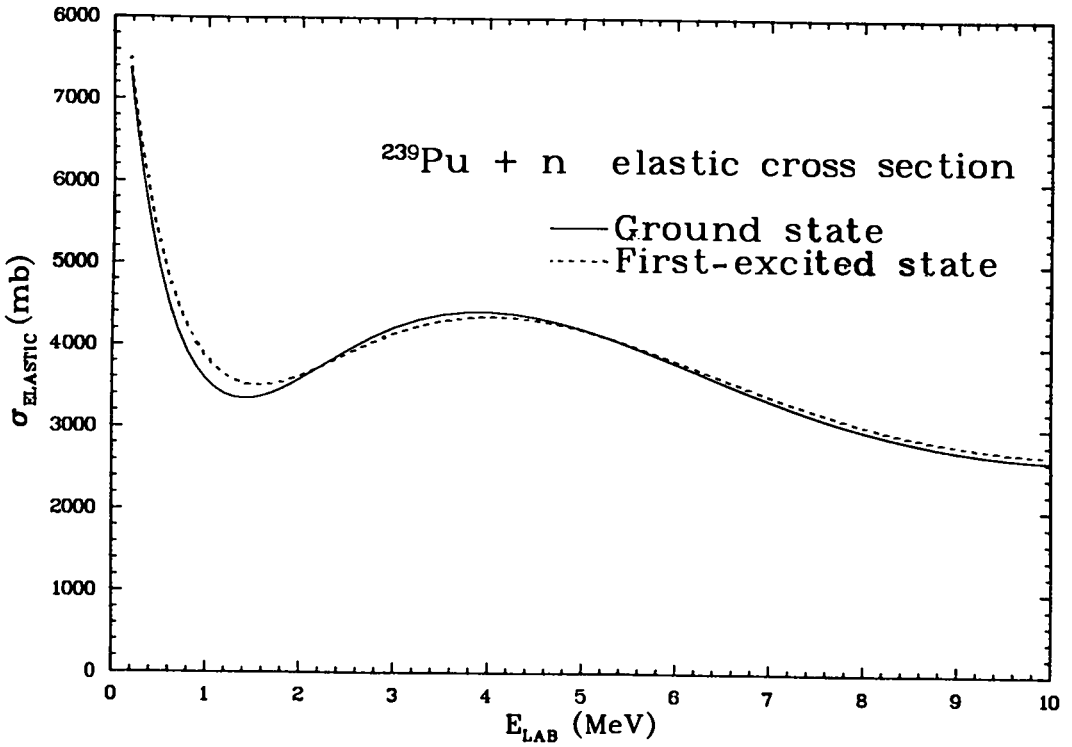

Fig. 43. Elastic cross section for the scattering of neutrons by ^{239}Pu in target states identical to those of Fig. 41.

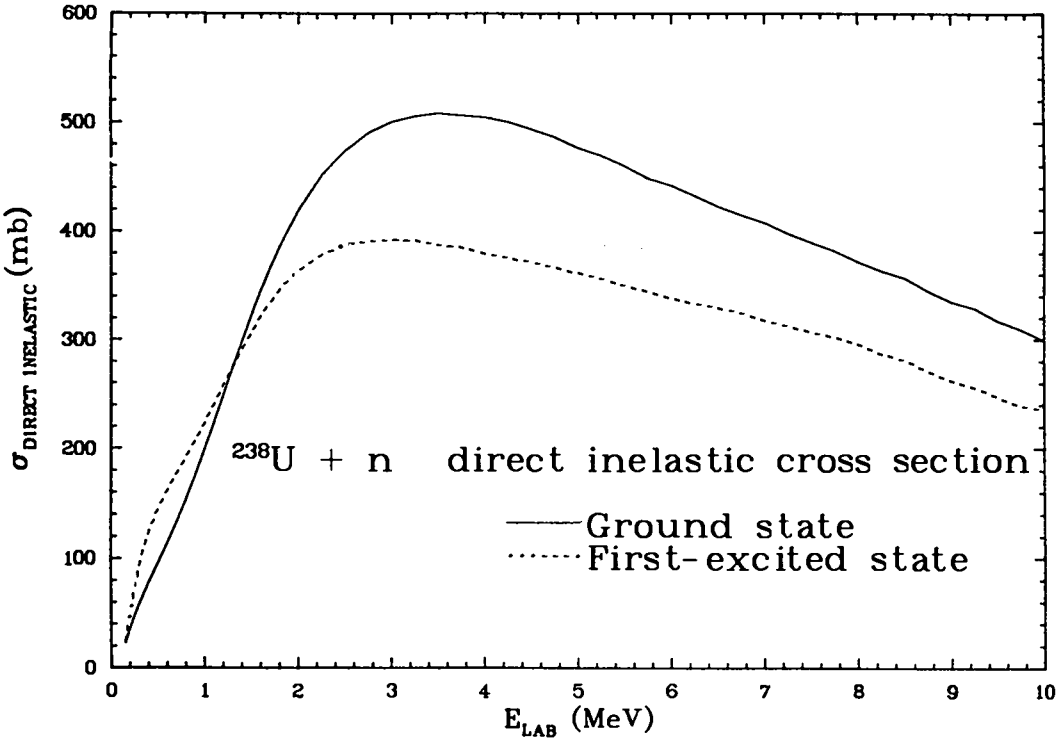

Fig. 44. Direct inelastic cross section for the scattering of neutrons by ^{238}U in target states identical to those of Fig. 40.

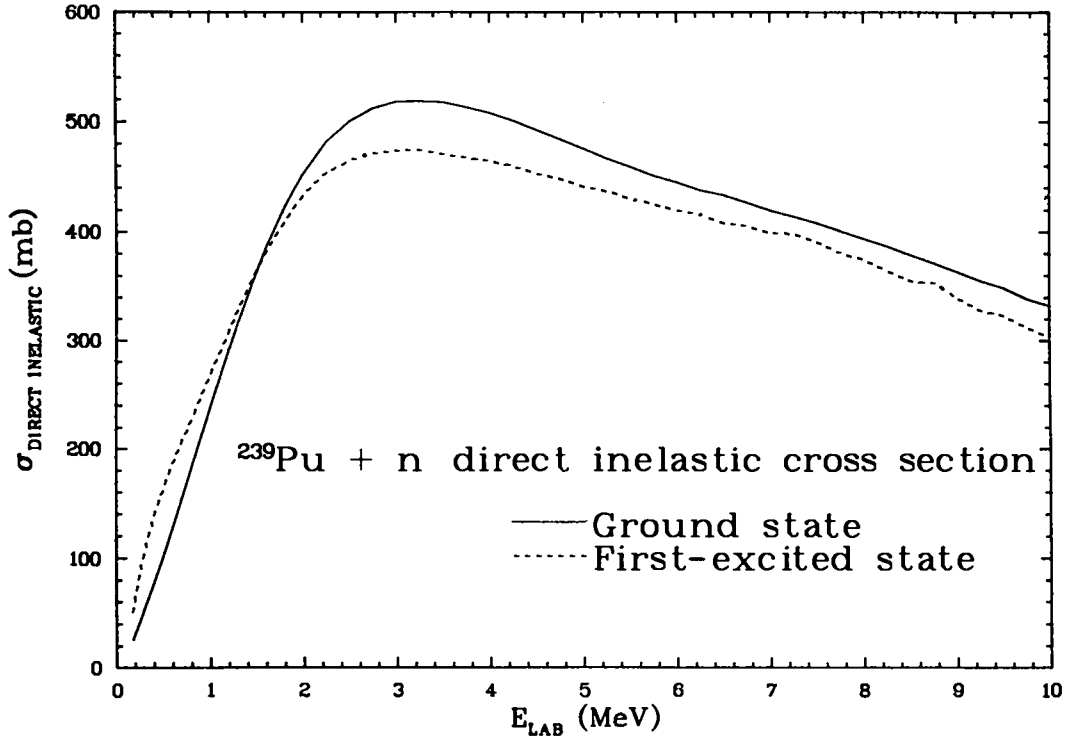

Fig. 45. Direct inelastic cross section for the scattering of neutrons by ^{239}Pu in target states identical to those of Fig. 41.

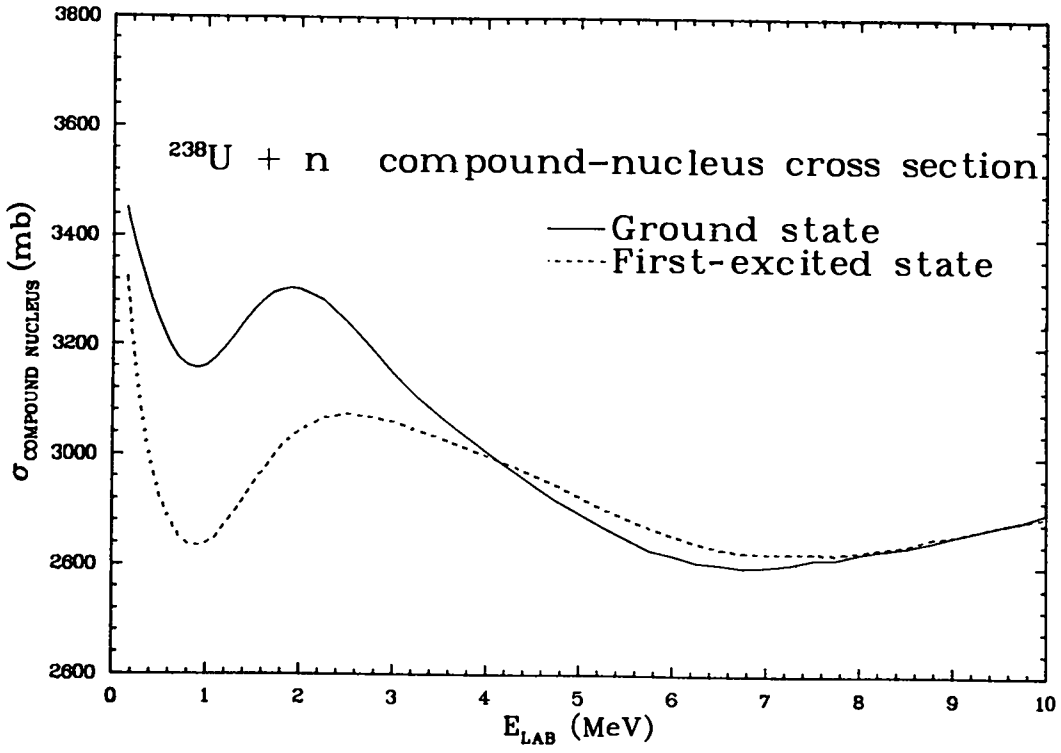

Fig. 46. Compound-nucleus formation cross section for the scattering of neutrons by ^{238}U in target states identical to those of Fig. 40.

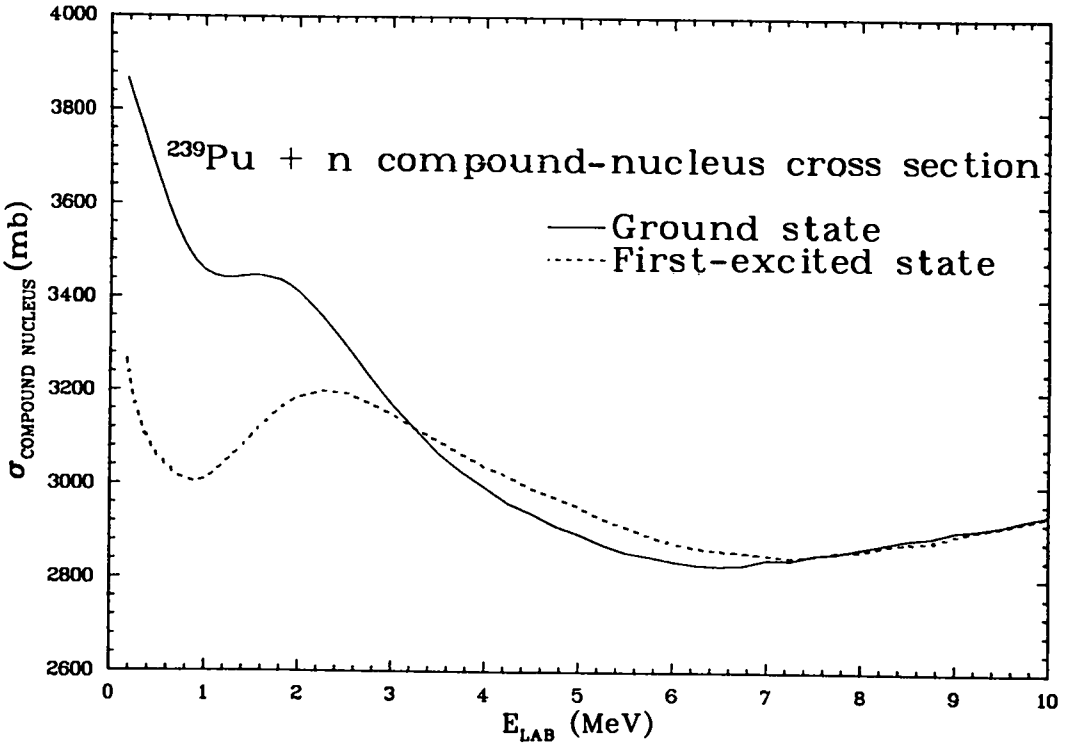

Fig. 47. Compound-nucleus formation cross section for the scattering of neutrons by ^{239}Pu in target states identical to those of Fig. 41.

M. Coupled-Channel Calculations for n + ^{237}Np Scattering (D. G. Madland)

Preliminary coupled-channel calculations have been performed for the scattering of neutrons by ^{237}Np. The calculations were performed using the code JUPXST.[26] The total, shape elastic, reaction, direct inelastic, and compound-nucleus formation cross sections were calculated, together with the corresponding compacted transmission coefficients $T(\ell,j)$, as a function of incident neutron energy over the range 1 keV to 20 MeV. The resulting transmission coefficient sets will be used in Hauser-Feshbach statistical-model calculations.

Pertinent details of the calculations are as follows. The actinide coupled-channel potential of Madland and Young[77] was used throughout. The deformation parameters used are $\beta_2 = 0.214$ and $\beta_4 = 0.074$. These are obtained from the theoretical calculations of Möller and Nix[80] and Möller, Nilsson, and Nix.[81] However, the value of β_4 was scaled downward from the theoretical value 0.104 to the above value using a scale factor obtained from comparing theoretical and experimental (neutron scattering) β_4 values for ^{238}U and ^{239}Pu. This procedure was followed because there are no known experimental values of β_4 for ^{237}Np. The theoretical value of β_2 was not similarly adjusted because the scaled value (0.210) is only slightly different. The expansion order of the complex form factor used in JUPXST is $\lambda = 8$ (Legendre polynomial P_8). A matching radius of 14.0 F was chosen and the algorithm for the maximum projectile orbital angular momentum, ℓ_{max}, is $\ell_{max} = 2.5\ (kR+1) + I_{max}$, where k is the neutron wave number, R is the nuclear radius, and I_{max} is the maximum spin occurring in the set of coupled states. For these calculations the first three members of the ground-state rotational band were coupled. These are the ($5/2^+$, 0.00), ($7/2^+$, 0.0332), and ($9/2^+$, 0.0758) states.

The results of these preliminary calculations are shown in Figs. 48-51 where, respectively, the total, elastic, summed direct inelastic, and compound-nucleus formation cross sections are shown.

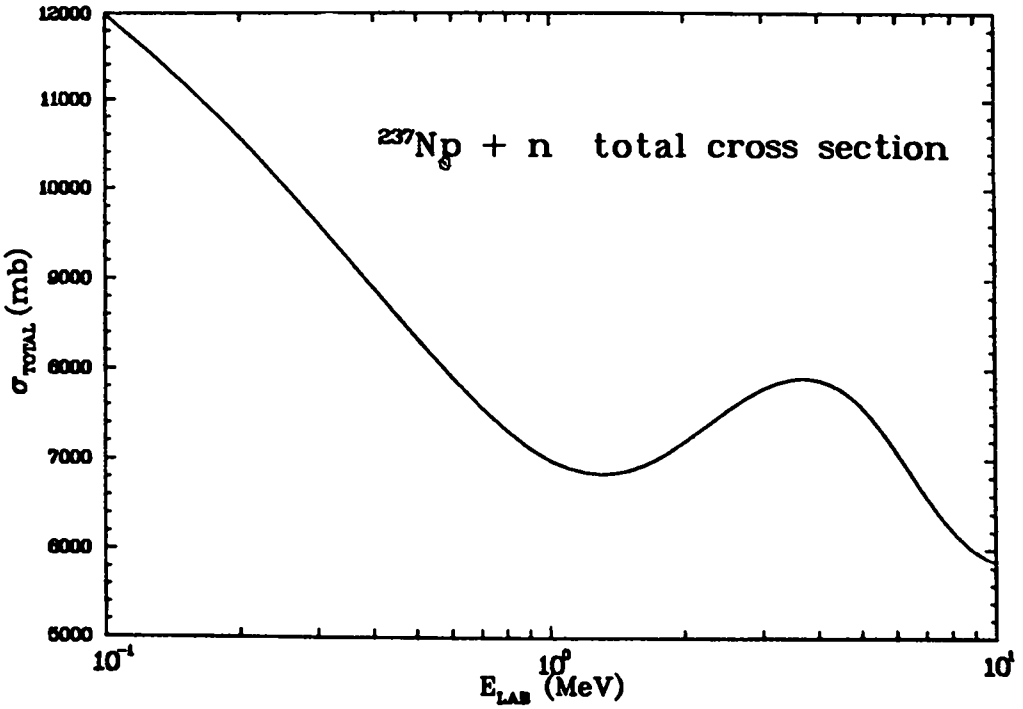

Fig. 48. Calculated total cross section for the scattering of neutrons by ^{237}Np as a function of the incident neutron energy.

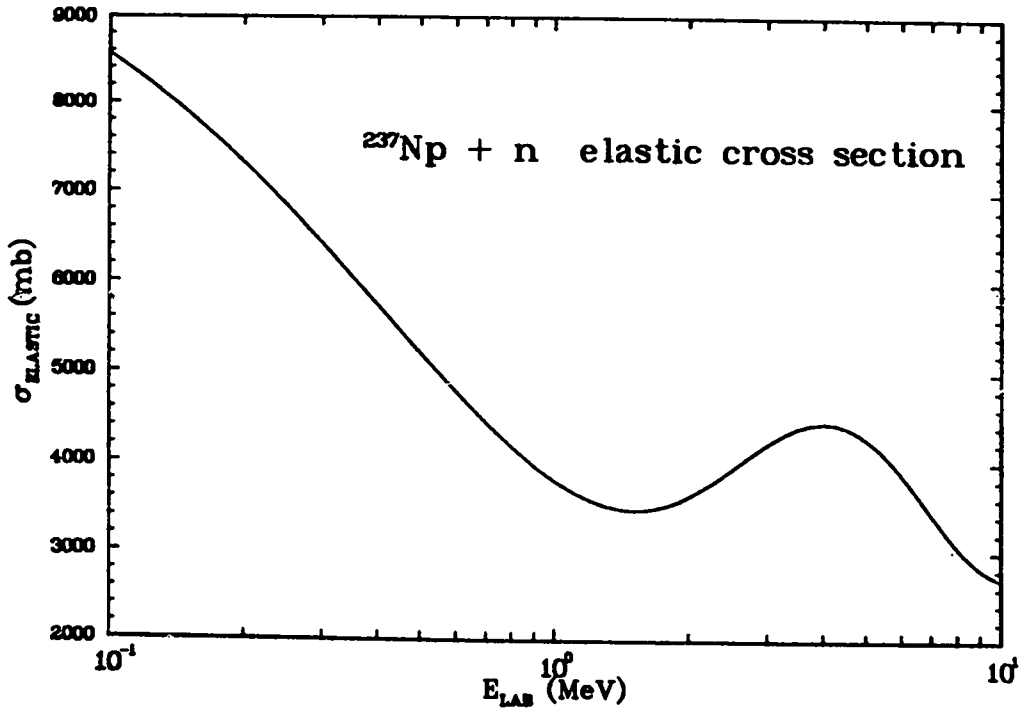

Fig. 49. Calculated elastic cross section for the scattering of neutrons by ^{237}Np as a function of the incident neutron energy.

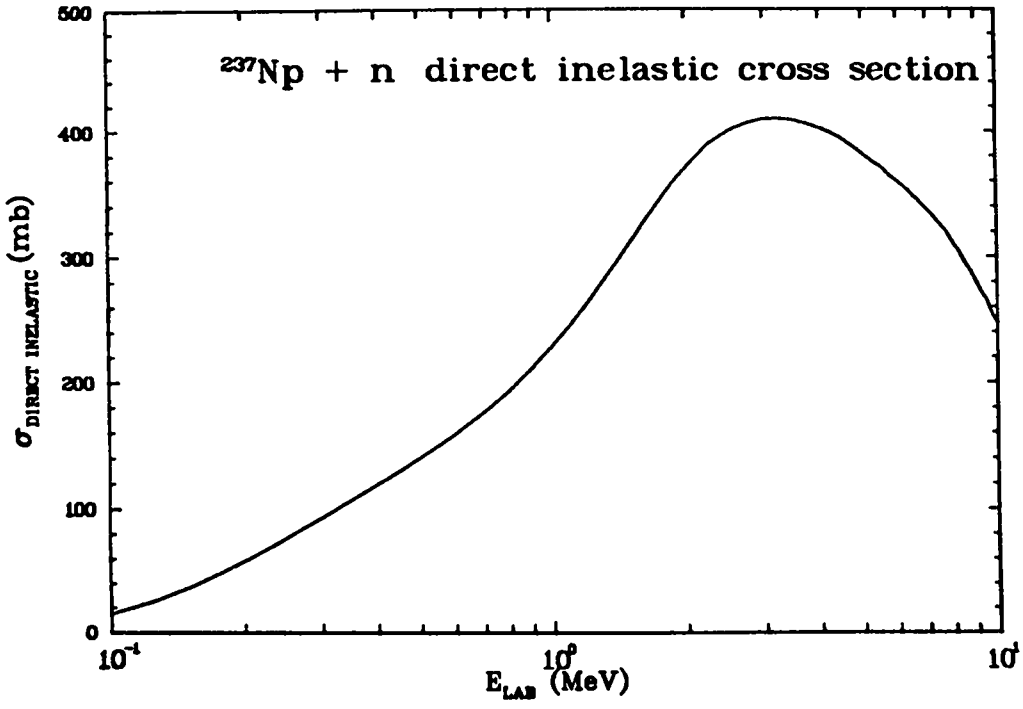

Fig. 50. Calculated direct inelastic cross section for the scattering of neutrons by ^{237}Np as a function of the incident neutron energy.

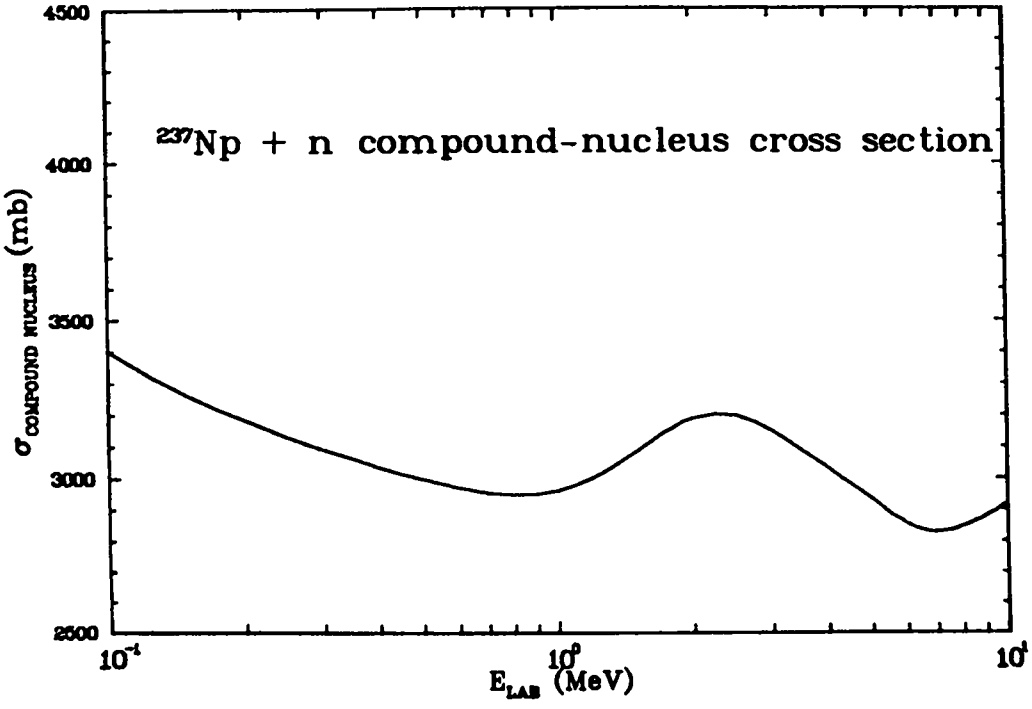

Fig. 51. Calculated compound-nucleus formation cross section for the scattering of neutrons by ^{237}Np as a function of the incident neutron energy.

N. Initial Calculation of Prompt Fission Neutron Spectra and $\bar{\nu}_p$ for the Neutron-Induced Fission of ^{237}Np (D. G. Madland)

Preliminary calculations of the prompt fission neutron spectrum N(E) and the average prompt neutron multiplicity $\bar{\nu}_p$ have been carried out for the ^{237}Np + n system. Although fairly complete measurements of $\bar{\nu}_p$ have been made, very little data exist on the prompt fission neutron spectrum for this nucleus. Moreover, the ENDF/B-V representation of the fission spectrum is inadequate, consisting of a simple Maxwellian with a single temperature parameter, 1.315 MeV, for all incident neutron energies. Since the fission spectrum N(E) and $\bar{\nu}_p$ are strongly coupled, we calculate both in order to obtain the best physical representation.

Pertinent details of the calculations are as follows. The constant compound-nucleus cross section approximation[35] was used in the calculation of both N(E) and $\bar{\nu}_p$. The seven-point approximation[35] was used in the calculation of the average energy release in fission $\langle E_r \rangle$ and the average neutron separation energy $\langle S_n \rangle$. The peaks of the fragment mass distribution were taken as $^{100}_{39}$Y and $^{138}_{54}$Xe, based on systematics of nearby actinides and the empirical result of an average departure of 1/2 charge unit from the unchanged charge density assumption in fission fragment formation. The total average fission fragment kinetic energy $\langle E_f^{tot} \rangle$ and total average prompt gamma energy $\langle E_\gamma^{tot} \rangle$ were calculated to have the values 174.3 MeV and 6.754 MeV, respectively. The effective level-density parameter used in the calculations is a_{eff} = A/(10.0 MeV), from Ref. 35.

Some of the results thus far are illustrated in Figs. 52 and 53, where comparisons of our calculated spectra and the ENDF/B-V Maxwellian are made for neutron energies of 1 and 3 MeV. These comparisons show the energy dependence of our spectrum (the ENDF/B-V spectrum is independent of energy), and they show that our spectrum is, in general, harder than the ENDF/B-V spectrum. The calculations performed thus far have used default parameter values. Our next step is to take into account the influence of the $\bar{\nu}_p$ experimental data.

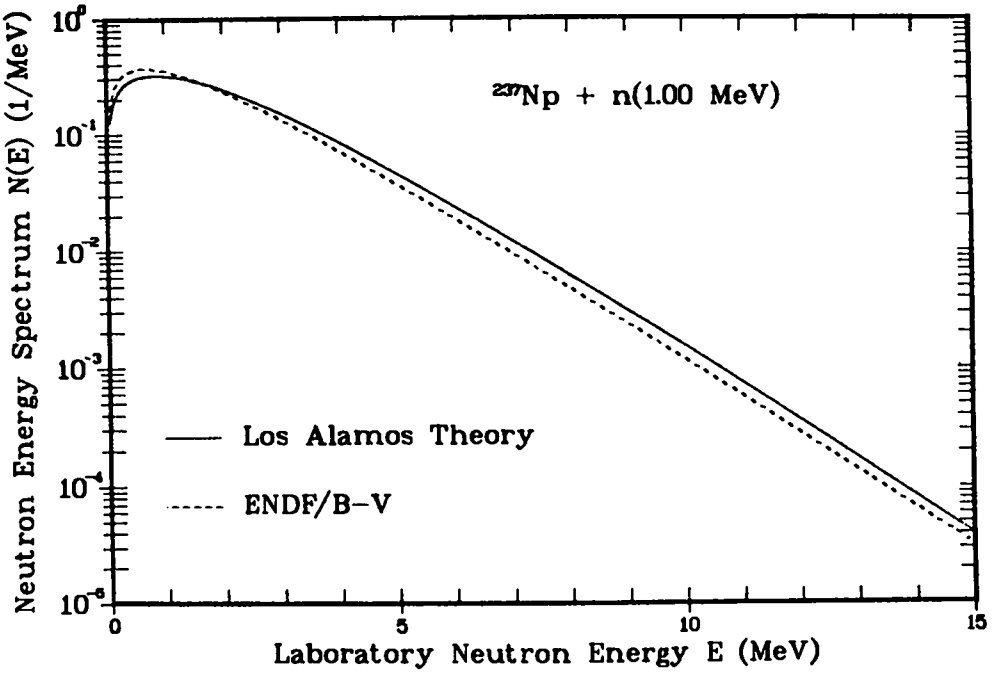

Fig. 52. Comparison of calculated prompt fission neutron spectra for the neutron-induced fission of ^{237}Np by 1 MeV neutrons.

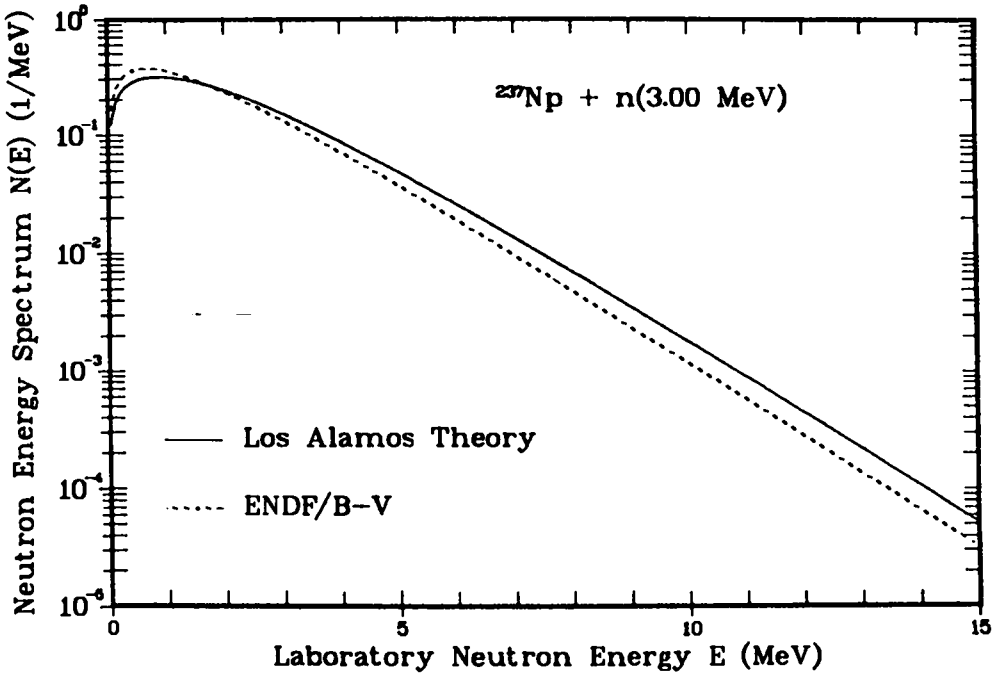

Fig. 53. Comparison of calculated prompt fission neutron spectra for the neutron-induced fission of ^{237}Np by 3 MeV neutrons.

II. NUCLEAR CROSS-SECTION PROCESSING AND TESTING

A. Time-Dependent Photon Spectra from Fission of ^{235}U and ^{239}Pu (D. G. Foster)

At the request of P-15, we have resurrected a small computer program, FISGAM, that calculates prompt-photon yields and time-dependent delayed-photon intensities following fission of ^{235}U and ^{239}Pu. This work is described in Ref. 82, p. 3, which discusses the sources of the data and the manner in which they were adapted for this use. Briefly, the prompt spectrum is represented in histogram form, and the delayed intensities are reconstructed from the half-lives and initial intensities of discrete emission lines. We approximate unresolved continuum emission with a two-term exponential series fitted to each original broad experimental bin. This technique allows one to calculate the spectra and their integrals over time from less than 1 ns to 50 s after fission, with an estimated accuracy of 20%.

In the process of resurrecting FISGAM, we have also made some needed improvements. The input data now reside in a FORTRAN block-data subroutine, instead of being read from an external file. The original routine for rebinning histograms has also been replaced with an improved version of REBIN (see Ref. 83, pp. 29-30). All of the input data are now represented in the energy grids that were used in the original measurements. The user now supplies a spectrum grid suitable to the application, and FISGAM converts all sources of input to this grid.

B. New Version of NJOY (R. E. MacFarlane and D. W. Muir)

Work continues on correcting and refining the most recently released version of the NJOY nuclear data processing system, NJOY (10/81). The latest set of corrections, reported in NJOY Note 10/81-4, are summarized in the following paragraph. In addition, a number of new capabilities have been implemented in the Los Alamos version of NJOY. These new capabilities, because of the substantial number of line changes required, have not yet been released to the NJOY general-user community. A new resequenced version, NJOY (6/83), which incorporates all current code corrections, as well as these new capabilities, will be released to the code centers in June 1983. The new capabilities of NJOY (6/83) are also described below.

The corrections reported in NJOY Note 10/81-4 fix a number of minor errors and improve transportability to IBM, VAX, and FORTRAN-77 systems. Other updates affect the calculation of gamma production for K and Cl in ENDF/B-V, the linearization of small cross sections in RECONR, the subdivision of the unresolved energy range in RECONR and UNRESR, discrete scattering from the highest energy group in GROUPR, and the control of precision (SIGFIG).

The additional changes in NJOY (6/83) include many "clean-up" and IBM- and FORTRAN-77-compatibility updates. Significant new capabilities include: addition of the Los Alamos 80-group, SAND-II 640-group, and EURLIB 100-group "built-in" structures, plus 80-group and CLAW weight functions in GROUPR; a full treatment of ratio-to-standard covariances (see Ref. 26, pp. 45-49) in ERRORR, as well as new lumped-partial, LB=4, and LB=6 covariance capabilities in that module; a new compressed-library output format (the BOXER format[84]) in COVR; a new photon production format and FORTRAN-77 output in ACER; delayed neutron output in POWR; and finally, better fission-matrix packing in NMATXS.

Changes were also made in GROUPR, ERRORR, COVR, and MODER to support full use of large group structures (up to 640 groups) in these modules. Anyone intending to use NJOY on IBM or VAX machines, as well as users needing ERRORR, COVR, ACER, POWR, or NMATXS, should move to the new version as soon as possible.

C. IAEA Processing Code Comparison (R. E. MacFarlane and D. W. Muir)

Since June 1981, we have been participating in a nuclear data processing code verification project,[85,86] organized by the Nuclear Data Section of the International Atomic Energy Agency (IAEA/NDS). The first round of comparisons required the calculation of the 36 reactions on the ENDF/B-V Dosimetry Tape (Tape 531). All cross sections were linearized and resonance-reconstructed at zero degrees Kelvin, both to an accuracy of 0.1%, using the RECONR module of NJOY. Then, infinite-dilution, flat-weighted cross sections were calculated with the GROUPR module in the 640-group SAND-II group structure, as a means of reducing the volume of data to be compared. These results were sent to the IAEA/NDS for comparison with the results of similar calculations performed at other research installations.

Overall, the results from these comparisons have been reassuring. Some disagreements were found for very small cross sections, for example, near reaction thresholds. As a result, we have tightened somewhat the linearization

accuracy criterion used in RECONR. Also some 1-2% disagreements occurred in the unresolved-resonance range because of the use of parameter interpolation instead of cross-section interpolation. As discussed in the following section, both RECONR and UNRESR now use cross-section interpolation for materials with energy-dependent unresolved parameters. A minor exception is that parameter interpolation is retained in any unresolved "panel" that is unusually wide, because the 1/v behavior of low-energy cross sections would be poorly represented there by linear cross-section interpolation. The situation is somewhat different in the case of materials with energy-independent unresolved parameters. At least some of the codes in use elsewhere have been using (incorrectly) cross-section interpolation for these materials, rather than parameter interpolation, as is done in NJOY.

As a by-product of this work, a complete 640-group library of ENDF/B-V dosimetry cross sections has been generated with the latest NJOY version and is available from the Los Alamos Nuclear Data group.

D. Energy-Dependence of Unresolved-Region Cross Sections (R. E. MacFarlane and D. W. Muir)

Cross sections in the unresolved energy range are computed from average resonance parameters given by the evaluator. The parameters are either (1) independent of energy within the given energy range or (2) they are given on a particular grid of energies in this range. For earlier versions of the ENDF/B format, the full energy dependence of the cross sections was defined by either (1) computing the cross sections from the energy-independent parameters at each energy or (2) computing the cross section from parameters obtained by interpolating between the values given at the adjacent energy grid points.

For ENDF/B-V, it was decided to use cross-section interpolation instead of parameter interpolation in many cases. However, the procedures written into the format manual[87] were ambiguous (see especially p. 2.20 and pp. 2.23-2.25). This ambiguity showed up in the IAEA-processing code comparisons discussed above. The following comments are intended to call attention to the differences seen, and to suggest the best procedure to use for each case.

When energy-independent parameters are given, the manual states clearly that the cross section must be computed from the parameters at intermediate energies and not obtained by interpolating between the cross sections at the ends of the unresolved range (p. 2.23). Some versions of some of the processing codes have incorrectly used cross-section interpolation in this case.

For evaluations using energy-dependent parameters, cross-section interpolation should be used. However, some evaluations do not have a "dense enough" mesh (see p. 2.24) to represent the approximate 1/v energy dependence of the capture and the possibly more complicated shape of the fission at the same time. Using the "official" cross-section interpolation can lead to errors as large as 50% for ^{238}Pu and 25% for ^{237}Np. For such evaluations, parameter interpolation gives better answers.

The ultimate solution to this problem is to re-evaluate the unresolved resonance parameters for the problem isotopes. This will take several years at current levels of activity. In the meantime, we are recommending to the Cross Section Evaluation Working Group (CSEWG) that the procedures be changed. We suggest that any energy interval in the unresolved range that is wider than some specified value (for example, a factor of 3) should be subdivided using parameter interpolation. This procedure gives reasonable results for all the materials of ENDF/B-V.

E. New Nonlinear Capability in ALVIN (D. W. Muir)

In least squares data-adjustment studies, the measured integral data can be strongly non-linear functions of the cross sections. The most common non-linearity occurs when the integral quantity $T(\Sigma)$ is approximately an exponential function,

$$T(\Sigma) \cong a \exp(-\Sigma r) \quad ,$$

where Σ is the macroscopic cross section and r is the spatial location. If the cross section Σ has an uncertainty $\Delta\Sigma$, then the condition for linearity of $T(\Sigma)$ over the range of adjustment of Σ is, in this case,

$$\Delta\Sigma \cdot r << 1 \quad . \qquad (1)$$

This condition is not satisfied in typical neutron-shielding integral experiments,[88] for example. In a linear least squares adjustment program such as ALVIN,[89] a linear model is used to approximate $T(\Sigma)$ in the neighborhood of the evaluated cross-section values, but, in these nonlinear problems, the model breaks down before the solution point is reached. Because it is the linear model, and not $T(\Sigma)$, that is actually used to calculate the calculation/measurement discrepancies in the least squares method, deficiencies of the model will

distort the adjusted data in the same way as systematic errors in the integral measurement.

Fortunately, this calculational bias can be reduced to negligible proportions by an iterative procedure, wherein the least squares solution from the first pass is used as the reference point for the linear model for the second pass, and so on. Such a procedure can now be followed, using a new user-selected option in ALVIN. With this option, a distinction is drawn between the evaluated nuclear data set and the reference nuclear data set. The evaluated set (for example, ENDF/B-V) is based solely on differential measurements and does not change from one iteration to the next. The input cross-section covariances are a property of the evaluated set and, likewise, do not change. The reference set, on the other hand, is simply the mathematical reference point for a Taylor-series expansion of $T(\Sigma)$, and this point is allowed to vary.

The input sensitivity coefficients are evaluated at the reference point, and thus they must be recalculated for each iteration. By convention, sensitivities are normalized (whether produced by the sensitivity module of ALVIN or by a separate sensitivity code) by dividing the fractional change in the integrals by the fractional change in the reference cross sections. Thus, the reference set must be supplied explicitly to ALVIN, when using the new option, so that ALVIN can renormalize the sensitivities to the evaluated set.

To explain this step in more detail, the relationship between the nonlinear function $t_i(x)$ and the cross-section data can be expanded in a Taylor series about the reference point x^{ref},

$$t_i(x)\Big|_{lin} = t_i(x^{ref}) + \sum_j \left.\frac{\partial t_i(x)}{\partial x_j}\right|_{ref} (x_j - x_j^{ref}) \quad .$$

Next, divide through by the evaluated (that is, measured) values of the integral and differential data,

$$\left.\frac{t_i(x)}{t_i^{eval}}\right|_{lin} = \frac{t_i(x^{ref})}{t_i^{eval}} + \sum_j \left[\frac{x_j^{eval}}{t_i^{eval}} \left.\frac{\partial t_i}{\partial x_j}\right|_{ref}\right] \left(\frac{x_j}{x_j^{eval}} - \frac{x_j^{ref}}{x_j^{eval}}\right) \quad .$$

Denoting the quantity in square brackets S_{ij}, we obtain the explicit form of the linear model used in ALVIN,

$$\left.\frac{t_i(x)}{t_i^{eval}}\right|_{lin} = \frac{t_i(x^{ref})}{t_i^{eval}} + \sum_j S_{ij}\left(\frac{x_j}{x_j^{eval}} - \frac{x_j^{ref}}{x_j^{eval}}\right) \quad .$$

The sensitivity codes do not provide the elements of S directly, but rather $\tilde{S}$, where

$$\tilde{S}_{ij} = \frac{x_j^{ref}}{t_i(x^{ref})} \left.\frac{\partial t_i(x)}{\partial x_j}\right|_{ref} \quad . \tag{2}$$

Thus, ALVIN performs the following renormalization of the input sensitivities,

$$S_{ij} = \tilde{S}_{ij} \frac{t_i(x^{ref})}{t_i^{eval}} \frac{x_j^{eval}}{x_j^{ref}} \quad .$$

The user input is only slightly changed from that described in Ref. 89. First, the control-parameter card, which previously contained 4 parameters (KSENS, KADJST, MI, MJ), now contains 5 parameters (KSENS, KADJST, KREF, MI, MJ). KREF=1 means use the original calculational path where the reference data are identical with the evaluated data, and KREF=2 means that the reference data may be different from the evaluated data, as in the case of non-linear iteration. If KREF=2, one enters (with title cards) two new arrays, namely, XR(J) and YR(I), and not YC(I). XR(J) is the reference differential data vector, expressed as ratios to the evaluated (measured) differential data, and YR(I) is the integral data vector calculated at the reference point, expressed as ratios to the evaluated (measured) integral data. Upon input, the array DYDX(I,J) in ALVIN is equal to the relative sensitivity, Eq.(2), as calculated at the evaluated data point (KREF=1) or the reference data point (KREF=2).

In all test calculations performed to date using the new option, the reference data set is observed to approach the solution set very rapidly. Adjustment factors (adjusted data ÷ evaluated data) approach asymptotic values, reaching four-place agreement after just 3 or 4 iterations. The new ALVIN version is available on request from the Los Alamos Nuclear Data Group.

III. FISSION PRODUCTS AND ACTINIDES: YIELDS, DECAY DATA, DEPLETION, AND BUILDUP

A. Summary Fission-Product and Actinide Data [T. R. England, W. B. Wilson (R. E. Schenter, and F. Mann, Hanford Engineering Development Laboratory)]

A summary report of the fission-product and actinide data contained in the ENDF/B-V data files has been prepared.[90] An expansion of the descriptive text of this report will be added, along with an Appendix identifying errors and data corrections to ENDF/B-V; it will be issued as a report by the Electric Power Research Institute.

Summary data for all 877 fission products and 60 actinides in Rev. "0" are included in Ref. 90. Appendices contain some additional augmentation of the data; these are noted on schematics of all coupled fission products and actinides (a total of 144 actinides). The main text consists of Rev. "0" data. (In the case of group cross sections processed from Rev. "0," error corrections are discussed in the main text.) Mass chain yields, decay parameters (half-lives; branchings; beta-, gamma-, and alpha-energies), processed one-group cross sections for fast reactors, and the resonance integrals and 2200-m/s cross sections are included, as well as other information pertinent to the ENDF/B-V files. We have prepared this document to serve as a relatively concise source for the most frequently requested data and as a convenient reference for the fission-product and actinide data contained in ENDF/B-V.

As noted, the report contains processed group cross sections for typical fast- and thermal-reactor spectra. The thermal spectrum used is given in Ref. 91, and three diverse fast spectra are plotted in Fig. 54. These spectra were used with the 154-multigroup cross sections originally processed with NJOY[92] and to collapse the cross sections to four groups for thermal reactors and one group for the three fast-reactor spectra, in the manner described in the TOAFEW-V manual.[92]

B. Delayed Neutron Data and Spectra [T. R. England, W. B. Wilson (R. E. Schenter, and F. M. Mann, Hanford Engineering Development Laboratory)]

Revised precursor spectra (15 in number) were used in the 105-precursor library described in Ref. 93, and all calculated aggregate spectra and comparisons were redone. The calculations and comparisons with evaluated spectra are extensive. Equilibrium spectra in the conventional six-time groups and total spectra are included for eleven fissionable nuclides at one or more neutron fission energies. The results are summarized in Ref. 94, a paper accepted for

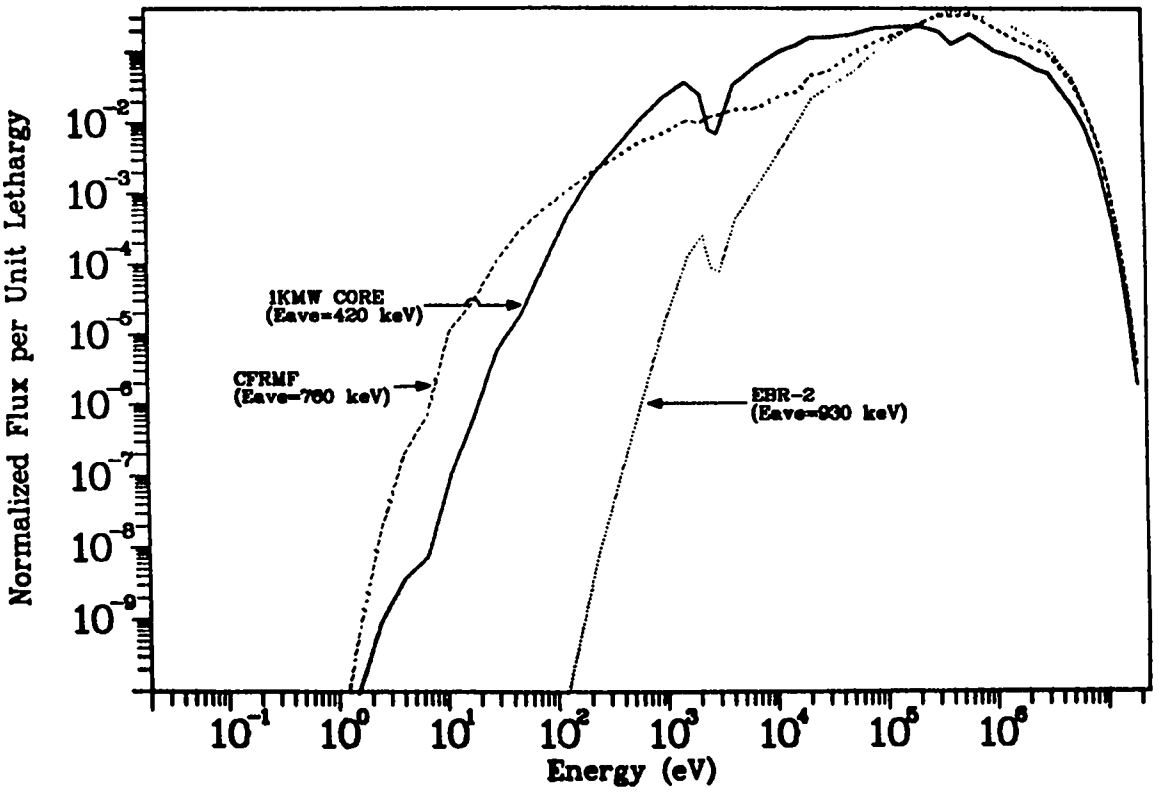

Fig. 54. Fast flux spectra used for one-group cross sections.

publication in Nuclear Science and Engineering, and all results are available in an Appendix to the Los Alamos National Laboratory document.[94]

Pn values were revised and preliminary values published.[95] Final values are being prepared for publication.

C. Fission Product Yield Status [T. R. England, D. C. George, and B. F. Rider (General Electric Co., retired)]

The effort to get codes operational and to correct the master data libraries for 50 yield sets was described in the last progress report (see Ref. 26, p. 63). That effort has continued for a short time into the current reporting period. All master data sets have now been corrected and the first ten yield sets for Version D have been produced. A draft manual describing the use of the evaluation codes has also been prepared as well as additional recent data in the required format for use with the codes. We anticipate an increased effort to add new data and to complete an evaluation for ENDF/B-VI during the last half of calendar year 1983.

D. Development of CINDER-2 Libraries for Special Purpose Calculations [W. B. Wilson, T. R. England, D. Davidson (MP-3), R. A. Michelotti (AT-4), C. A. Mangeng (S-4), M. A. Battat (T-Div. Consultant), and G. R. Thayer (S-4)]

1. Eight-hundred-MeV Proton Accelerator Target Inventory Calculations.

Experiments are planned with the Los Alamos Meson Physics Facility (LAMPF) accelerator for 800-MeV protons on targets of $CaCO_3$, Al, and W. Calculations by Group MP-3 performed with the HETC Monte Carlo transport code, incorporating intranuclear-cascade and evaporation reaction calculations, have identified 328 reaction product nuclides for the three target materials. An additional 117 nuclides are produced by radioactive decay. A 246-chain library of 1158 linear nuclides has been constructed to describe the temporal inventory of the 445 nuclides. Many of the nuclides are far above the line of stability and have unmeasured half-lives and/or decay modes. One-second half-lives were asigned to 40 nuclides without measured values, and decay modes were assumed for 42 nuclides.

Reaction nuclide yields from HETC and average decay energies remain to be added for irradiation/decay studies. Radionuclide inventory calculations are planned for the identification of major radiation contributors at cooling times exceeding one hour following typical irradiation periods. Multigroup spectral data will be accumulated for these major contributors for the description of the radiation sources of the three target materials following irradiation.

2. FMIT Prototype Accelerator Targets.

The prototype of the Fusion Materials Irradiation Test Facility (FMIT) accelerator is under construction by Los Alamos Group AT-4. Acceleration of 0.1 A of 2-MeV H_2^+ ions on a Cu-beam dump is planned for the near future, and acceleration of 0.1 A of 5-MeV H_2^+ ions on a C-beam dump is proposed for FY 84. Each beam is assumed to contain 300 ppm contamination of $^2H^+$ ions. We have examined the nuclear reactions associated with each of the beam/target systems relative to the radiation hazards of the prototype operation.

The low-energy beam will deliver 1.23×10^{18} 1-MeV protons, each assumed to react independently of its loosely burned neighbor and 1.85×10^{14} 2-MeV deuterons on the Cu beam stop each second. These have approximate ranges of 13 μm and 25 μm, respectively. The ^{63}Cu and ^{65}Cu of the beam stop have 16 nuclear reactions with positive Q-values or thresholds below the incident proton and deuteron energies; however, the potential barrier of each particle/target combination far exceeds the incident particle energy.

The higher energy beam will deliver 2.5-MeV protons and 5-MeV deuterons on C with approximate ranges of 60 μm and 110 μm, respectively. The ^{12}C and ^{13}C of the beam stop have 13 nuclear reactions with positive Q-values or thresholds below the incident proton and deuteron energies, and none of these reactions are precluded by the lower potential barrier of the light target nuclides. The products of these reactions are $^{10,11}B$, ^{14}C, and $^{13\text{-}15}N$.

The high intensity of the beam leads to the consideration of 58 additional reactions on these product nuclides. This system of incident protons and deuterons on principal and first-generation product nuclides results in the production of 13 radionuclides: tritium, $^{7,8,10}Be$, $^{9,12}B$, $^{11,14,15}C$, $^{13,16}N$, and $^{14,15}O$.

The temporal description of these radionuclides requires the formation of a library of radioactive decay and reaction cross-section data. Proton and deuteron cross sections for most of these reactions have not been measured over the energy range of interest. Cross-section calculations and library formation have been proposed for future consideration.

The production of x rays by the intense beams has not yet been addressed.

3. ^{241}Am Irradiation in Thermal Reactors.

Group S-4 is studying the economy of the irradiation of ^{241}Am, separated from spent fuel, for the production of ^{238}Pu via ^{242}Cm decay. A library for these calculations has been prepared to define the importance of all irradiation/decay paths to ^{238}Pu and fissionable nuclides and of the contribution of each fissionable nuclide to sample power. The actinide library contains 13 linear chains and 103 linear nuclides to describe 20 actinides. The standard fission-product library is used to sample power. Fission of Am and Cm nuclides in reactor fuels is not typically considered. ENDF/B-V does not contain fission-product yields for these nuclides, and they have been approximated in the library with the substitution of fission yields of related fissionable nuclides.

Our initial calculations of a 245-day irradiation of ^{241}Am in a BWR flux show that the fissions in $^{241,242g+m}Am$, ^{239}Pu, and ^{243}Cm result in initial, average, and peak power densities of 24 W/ghm, 154 W/ghm, and 179 W/ghm, respectively, compared with 24 W/ghm within the BWR fuel.

4. ICF Blanket Studies for Pu Production.

The CINDER-2 code and library are being used to calculate the production of Pu in an ICF Li/U blanket in a group S-4 study. Cross sections for each of eleven regions of the blanket are obtained with the TOAFEW-V collapsing code and library of 154-group processed ENDF/B-V cross sections,[91] using regional multigroup fluxes obtained in transport calculations.

E. Development of the SOURCES Code and Data Library for the Calculation of Neutron Sources and Spectra from (α,n) Reactions, Spontaneous Fission, and β^- Delayed Neutrons [W. B. Wilson, R. T. Perry (Texas A & M Univ.), J. E. Stewart (Q-1), T. R. England, D. G. Madland, and E. D. Arthur]

During the past three years we have calculated neutron sources from the spontaneous fission (SF) of actinide nuclides and from the (α,n) reactions of their decay α-particles with light nuclides. Neutron source materials studied include oxide fuels, carbide fuels, plutonium metal with contaminants, plutonium aqueous process solutions, uranium enrichment process constituents, and others. These calculations have required the accumulation and evaluation of measured and calculated (α,n) reaction cross-section, threshold, potential-barrier, and thick-target neutron yield data for a variety of target nuclides. Also accumulated were α-particle stopping cross-section data (describing the slowing of α-particles in various materials) and actinide decay constants, α-spectra, SF branchings, and $\bar{\nu}$ values. These data permit the calculation of the magnitude of a wide variety of SF and (α,n) sources.

This effort has recently been expanded to include β^- delayed neutron source multigroup spectra calculations for neutrons from SF, (α,n) reactions and β^- delayed neutron emission. SF neutron spectra are calculated from Watt Spectrum descriptions using A_{WATT} and B_{WATT} parameters obtained for 15 principal SF actinides from fits to more precise spectral descriptions or using parameters for 41 additional SF actinides obtained from fits based on the 15 nuclides. Neutron spectra for (α,n) sources are calculated using the simplifying assumption of isotropic neutron emission in the center-of-mass system attributed to Whitmore and Baker.[96] These calculations require α-particle energy-dependent branchings for the compound-nucleus decay to product nuclide energy levels. These branchings have been evaluated for a number of (α,n) reactions from available measured partial cross-section data, reciprocal (n,α_0) data, and/or GNASH[11] nuclear model code calculations. GNASH calculations, in turn, have required the accumulation of a library of optical model parameters and nuclear energy level data for target, compound nucleus, and product nuclides for (α,n) and competing α reactions. A typical multigroup (α,n) neutron spectrum is shown in Fig. 55 for $^{234}UF_6$ gas, calculated with α-particle stopping cross-section data of Ziegler[97] and (α,n) reaction cross-section data of Balakrishnan, Kailas, and Mehta.[98] The spectrum calculation was performed using product nuclide level branching data from both the partial cross sections

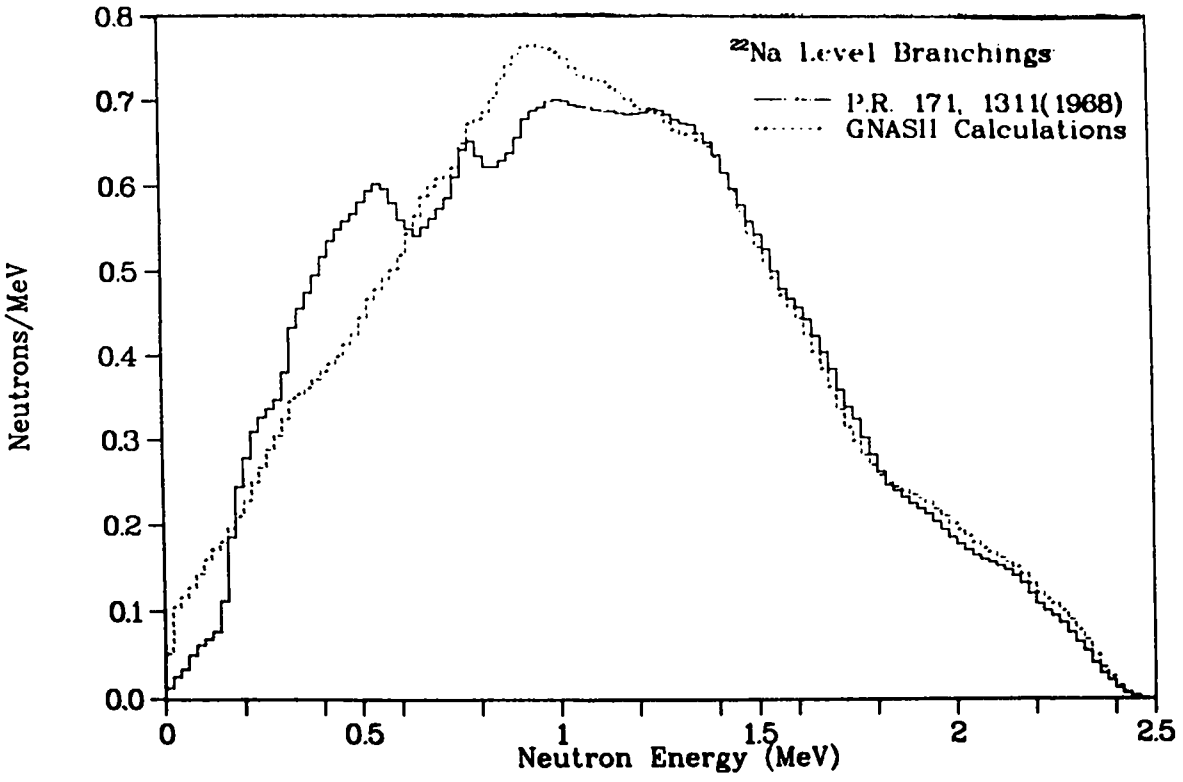

Fig. 55. Normalized $^{234}UF_6$ (α,n) neutron spectrum calculated with SOURCES code.

of Lehman[99] and the partial cross sections from GNASH calculations.[11] The data of Lehman, though smoothed, show considerable structure, are limited to energy levels of ^{22}Na at or below 1.54 MeV, and combine data associated with branchings to the lowest two excited states at 0.59 MeV and 0.66 MeV. The GNASH calculation includes all 8 levels at or below 1.98 MeV that may be excited by ^{234}U α-particles but cannot represent the structure of the measured data. The calculated spectra are in close agreement for neutron energies above 1.1 MeV because of the dominance of branching to low levels of ^{22}Na in reactions of higher energy α-particles in both branching data sources. Below this energy the structure of the measured data and smoothness of the calculated data are reflected in the respective calculated spectra.

SF and (α,n) neutron spectrum calculations are made in an arbitrary user-specified multigroup energy structure. The spectrum of β^- delayed neutrons for any inventory of fission-product and actinide nuclides is obtained using the 10-keV-binned spectral data and β^- delayed neutron branching (Pn) values of England et al.[94]

Documentation for the code and data library is currently in preparation.

IV. NEUTRONICS FOR CARBIDE LMFBR CORE COMPONENT DEVELOPMENT

(R. J. LaBauve, R. E. MacFarlane, and D. C. George)

We have prepared a preliminary set of carbide liquid metal fast breeder reactor (LMFBR) cross sections based on the CDS homogeneous carbide core. The processing path used is shown in Fig. 56.

The basic library is an 80-group MATXS file[100] produced by the NJOY nuclear cross section processing system.[92] The group structure is given in Table VII. Figure 57 shows the weight function and the group boundaries. Note that this is a typical LMFBR spectrum with a low-energy tail appropriate for the outer shield regions of a reactor.

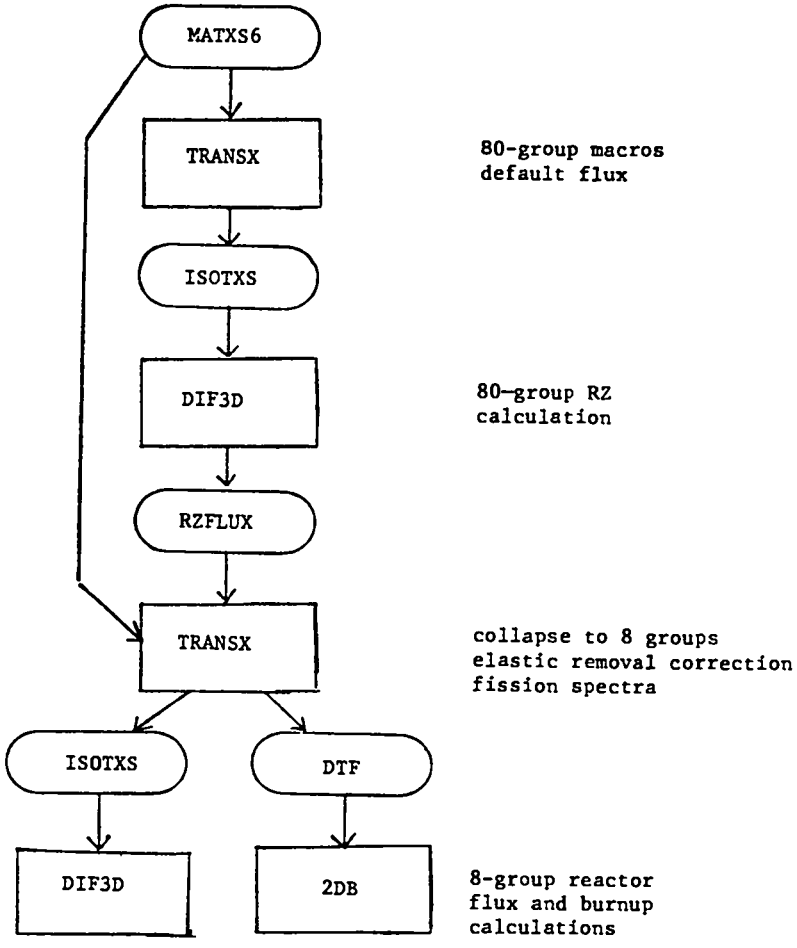

Fig. 56. Processing path for preliminary carbide reactor cross sections.

TABLE VII

BOUNDARIES FOR 80-GROUP STRUCTURE

GROUP	MAXIMUM ENERGY
1	2.00000E+07
2	1.69046E+07
3	1.49182E+07
4	1.34986E+07
5	1.19125E+07
6	1.00000E+07
7	7.78801E+06
8	6.06531E+06
9	4.72367E+06
10	3.67879E+06
11	2.86505E+06
12	2.23130E+06
13	1.73774E+06
14	1.35335E+06
15	1.19433E+06
16	1.05399E+06
17	9.30145E+05
18	8.20850E+05
19	7.24398E+05
20	6.39279E+05
21	5.64161E+05
22	4.97871E+05
23	4.39369E+05
24	3.87742E+05
25	3.01974E+05
26	2.35177E+05
27	1.83156E+05
28	1.42642E+05
29	1.11090E+05
30	8.65170E+04
31	6.73795E+04
32	5.24752E+04
33	4.08677E+04
34	3.18278E+04
35	2.50879E+04
36	2.60584E+04
37	2.47875E+04
38	2.18749E+04
39	1.93045E+04
40	1.70362E+04
41	1.50344E+04
42	1.32678E+04
43	1.17088E+04
44	1.03330E+04
45	9.11882E+03
46	8.04733E+03
47	7.10174E+03
48	6.26727E+03
49	5.53084E+03
50	4.88095E+03
51	4.30743E+03
52	3.80129E+03
53	3.35463E+03
54	2.96045E+03
55	2.61259E+03
56	2.30560E+03
57	2.03468E+03
58	1.79560E+03
59	1.58461E+03
60	1.39842E+03
61	1.23410E+03
62	1.08909E+03
63	9.61117E+02
64	7.48518E+02
65	5.82947E+02
66	4.53999E+02
67	3.53575E+02
68	2.75364E+02
69	1.67017E+02
70	1.01301E+02
71	6.14421E+01
72	3.72665E+01
73	2.26033E+01
74	1.37096E+01
75	8.31529E+00
76	5.04348E+00
77	3.05902E+00
78	1.12535E+00
79	4.13994E-01
80	1.52300E-01
EMIN	1.38879E-04

This library was first converted to 80-group macroscopic cross sections for each of the ten regions of the RZ reactor model shown in Fig. 58. The homogeneous self-shielding option of TRANSX[100] was used. This neglects the pin size, Dancoff factor, and disadvantage factor effects. The final smeared densities for each region are summarized in Table VIII.

The 80-group ISOTXS output from TRANSX was used for an 80-group DIF3D[101] flux calculation using the full-core model of Fig. 58. The resulting k_{eff} was 1.0051 (control rods out in this calculation). The zone-averaged 80-group fluxes from this calculation were saved in RZFLUX format. The problem was run twice, once with control rods in and once with rods out, to get fluxes for control regions for each case.

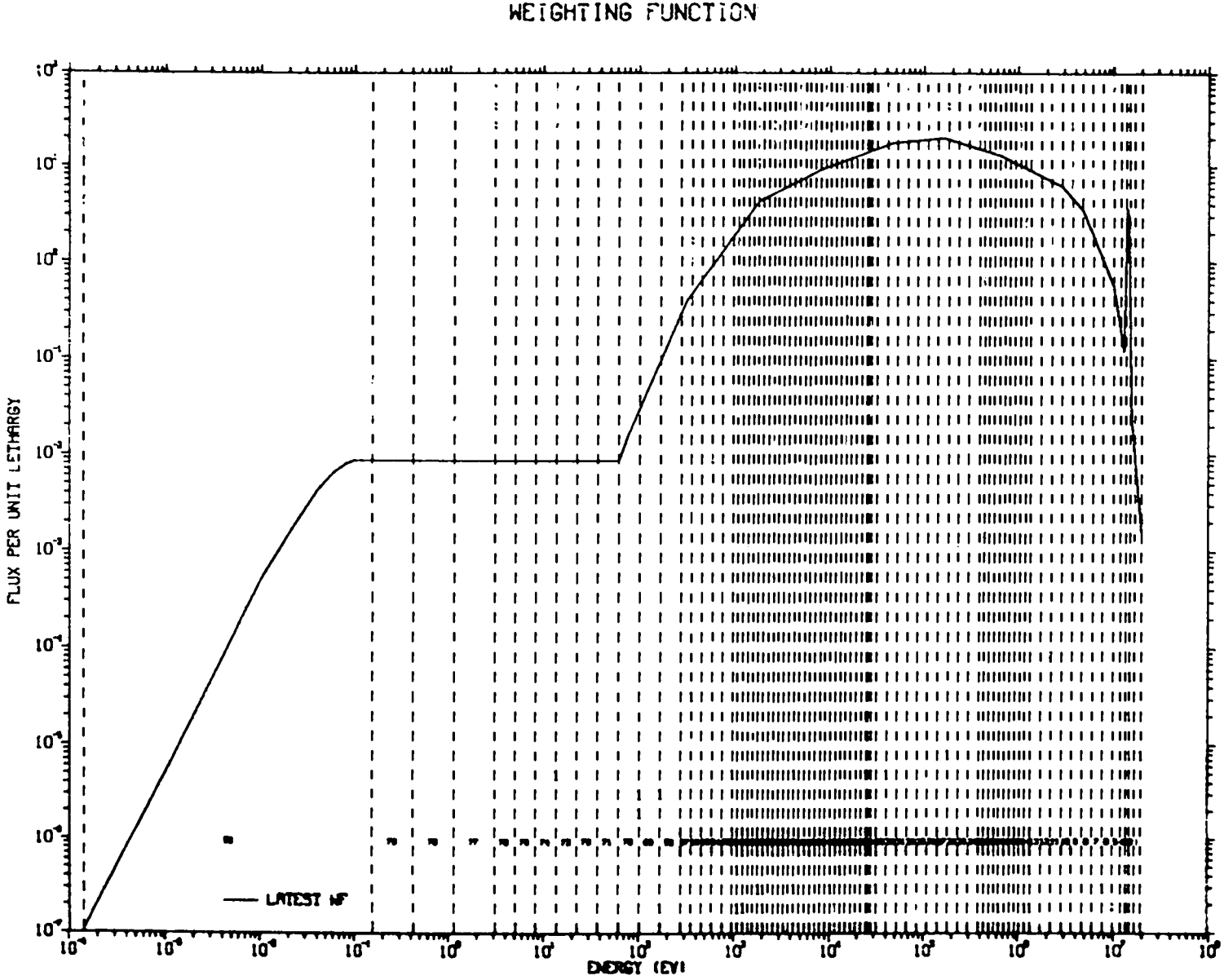

Fig. 57. Weight function and group boundaries used for 80-group set.

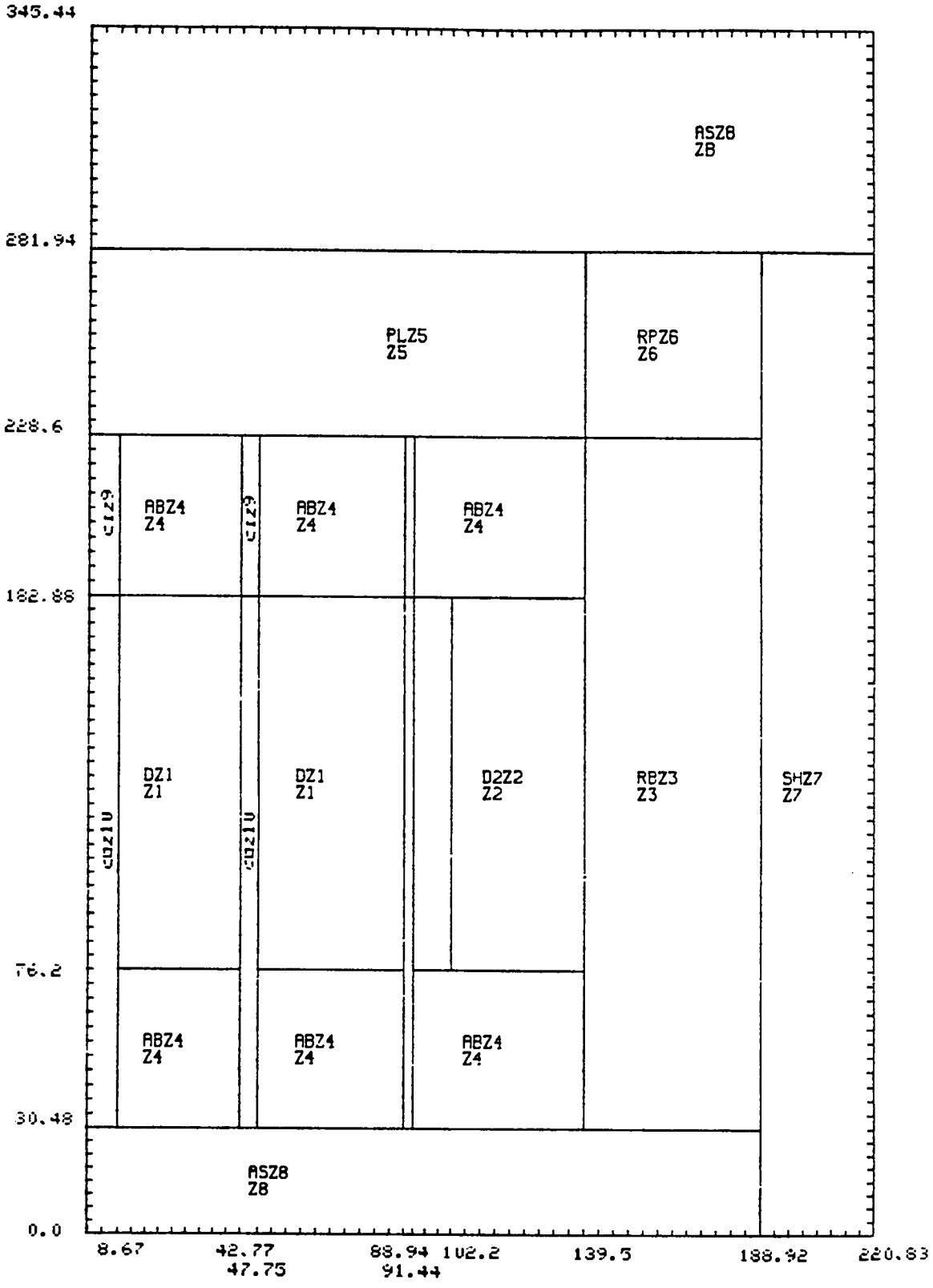

Fig. 58. CDS Carbide full-core R-Z model. Dimensions in cm.

TABLE VIII

HOMOGENIZED DENSITIES BY REGION FOR PRELIMINARY HOMOGENEOUS CARBIDE CORE

Material	D1	D2	RB	AB	DP	BP	RS	AS	CI	CO
U235	1.44-5	1.51-5	3.41-5	2.02-5						
U236	7.97-7	8.37-7								
U238	8.888-3	8.713-3	1.761-2	1.050-2						
Pu238	1.02-5	1.41-5								
Pu239	9.169-4	1.046-3	8.10-5	6.20-5						
Pu240	2.65-4	3.13-4	1.02-6	4.73-7						
Pu241	1.03-4	1.34-4								
Pu242	3.42-5	4.08-5								
F.P.*	5.61-4	4.35-4	1.73-5	1.16-5						
Cr	2.8803	2.880-3	2.058-3	2.880-3	2.880-3	2.058-3	1.147-2	1.232-2	4.611-3	3.163-3
Fe	9.920-3	9.920-3	7.087-3	9.920-3	9.920-3	7.087-3	3.951-2	4.242-2	1.588-2	1.089-2
Ni	1.968-3	1.968-3	1.406-3	1.968-3	1.968-3	1.406-3	7.837-3	8.416-3	3.151-3	2.161-3
Mo	2.230-4	2.230-4	1.594-4	2.230-4	2.230-4	1.594-4	9.659-4	9.537-4	3.570-4	2.449-4
Mn55	2.727-4	2.727-4	1.949-4	2.727-4	2.727-4	1.949-4	1.086-3	1.166-3	4.366-4	2.995-4
Na23	9.590-3	9.590-3	7.400-3	9.590-3	9.590-3	7.400-3	5.236-3	3.771-3	7.434-3	1.965-2
Carbon	1.125-2	1.119-2	1.852-2	1.105-2					9.149-3	
B10									3.367-2	
B11									2.928-3	
	inner driver	outer driver	radial blanket	axial blanket	driver plenum	radial blanket plenum	radial shield	axial shield	control in	control out

*F.P. densities should be divided by 2 for use with ENDF/B-V lumped fission product.

A second TRANSX run was used to collapse to the 8-group structure given in Table IX and to write the constituent microscopic cross sections for each region in the desired format. Because a flux file was available for this run, improved fission spectrum vectors and improved elastic removal cross sections could also be produced. The region fission spectra are given in Table X.

TABLE IX

ENERGY BOUNDARIES FOR 8-GROUP STRUCTURE

Group	Upper Energy	Group	Upper Energy
1	20.0 + 6 eV	5	6.73795 + 4
2	2.2313 + 6	6	1.93045 + 4
3	8.2085 + 5	7	2.03468 + 3
4	1.83156 + 5	8	1.28879 - 4

TABLE X

FISSION SPECTRA BY REGION FOR PRELIMINARY HOMOGENEOUS CARBIDE CORE

Region	Group 1	Group 2	Group 3	Group 4	Group 5	Group 6	Group 7	Group 8
D1	3.662E-01	4.009E-01	2.015E-01	2.412E-02	6.129E-03	1.074E-03	2.924-05	8.043-06
D2	3.662E-01	4.009E-01	2.016E-01	2.414E-02	6.138E-03	1.077E-03	2.934E-05	8.085E-06
RB	3.576E-01	4.031E-01	2.064E-01	2.533E-02	6.352E-03	1.086E-03	2.853E-05	7.366E-06
AB	3.591E-01	4.030E-01	2.054E-01	2.510E-02	6.305E-03	1.081E-03	2.852E-05	7.426E-06

The DTF-format cross sections produced for the two-dimensional diffusion code[102] contain the fission cross section in position 1 and the total in position 4, and the table length is 12. A list of the material numbers and names is given in Table XI. The last two letters of each material name define the region flux used for collapsing that particular material. Note that position 2 contains σ_a (approximately absorption minus n2n) and should not be used for accurate burnup calculations without correction. Separate n2n and capture cross sections are available on the ISOTXS library if needed.

TABLE XI

CROSS SECTION MATERIAL NUMBERS AND NAMES

1	D1	53	NAAB
2	D2	54	CAB
3	RB	55	U235RB
4	AB	56	U238RB
5	DP	57	PU39RB
6	BP	58	PU40RB
7	RS	59	FPRB
8	AS	60	CRRB
9	CI	61	FERB
10	CO	62	NIRB
11	U235D1	63	MORB
12	U236D1	64	MNRB
13	U238D1	65	NARB
14	PU38D1	66	CRB
15	PU39D1	67	CRDP
16	PU40O1	68	FEDP
17	PU41D1	69	NIOP
18	PU42O1	70	MODP
19	FPD1	71	MNDP
20	CRD1	72	NADP
21	FEO1	73	CRBP
22	NID1	74	FEBP
23	MDD1	75	NIBP
24	MND1	76	MOBP
25	NAD1	77	MNBP
26	CD1	78	NABP
27	U235D2	79	CRRS
28	U236D2	80	FERS
29	U238D2	81	NIRS
30	PU38O2	82	MORS
31	PU39D2	83	MNRS
32	PU40D2	84	NARS
33	PU41D2	85	CRAS
34	PU42D2	86	FEAS
35	FPD2	87	NIAS
36	CRD2	88	MOAS
37	FED2	89	MNAS
38	NID2	90	NAAS
39	MOD2	91	CRCI
40	MND2	92	FECI
41	NAD2	93	NICI
42	CO2	94	MOCI
43	U235AB	95	MNCI
44	U238AB	96	NACI
45	PU39AB	97	CCI
46	PU40AB	98	B10CI
47	FPAB	99	B11CI
48	CRAB	100	CRCO
49	FEAB	101	FECO
50	NIAB	102	NICO
51	MOAB	103	MOCO
52	MNAB	104	MNCO
		105	NACO

We made an additional series of 8-group calculations using the ISOTXS version of the library with DIF3D. Results for k-effective are summarized in Table XII. The k-effective for a three-dimensional, triangular-Z problem is also given in this table. The mid-plane hexagonal model for the 3-D problem is shown in Fig. 59. Note from Table XII that k-eff is increased by about .2% in going from 80 to 8 groups (R-Z geometry) and it is increased by about .3% in going from 2-D to 3-D geometry.

TABLE XII

RESULTS OF DIF3D FUNS OF CDS CARBIDE CORE PROBLEMS

Prob. No.	Type	No. of Gps	Remark	k-eff
1	R-Z	80	rods withdrawn	1.00505
2	R-Z	80	rods inserted	0.88015
3	R-Z	8	rods withdrawn, 8-gps collapsed from probs. 1 and 2.	1.00691
4	Triang-Z	8	rods withdrawn, 8-gps collapsed from probs. 1 and 2, 19-axial planes.	1.00957

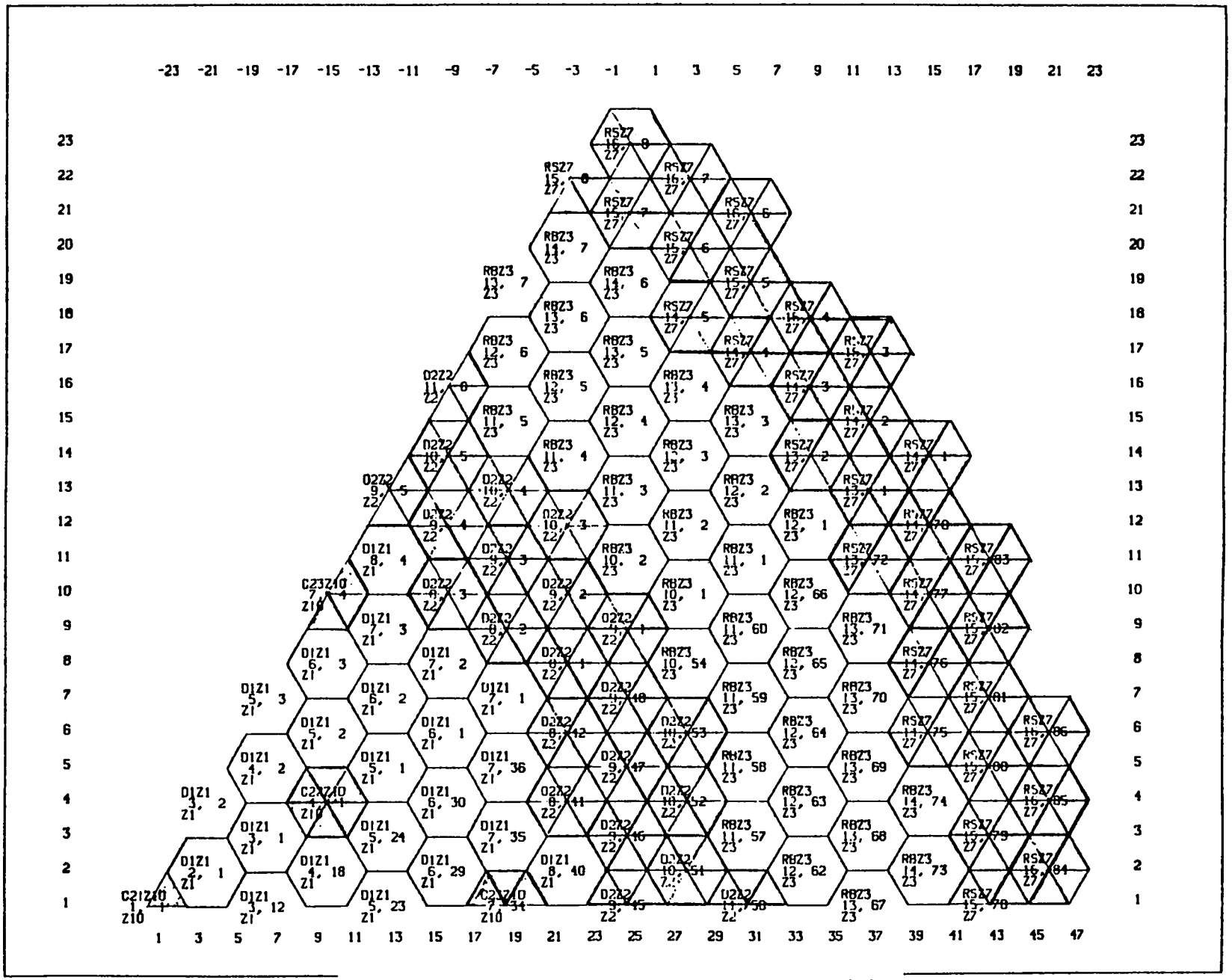

Fig. 59. Mid-plane of CDS Triangular-Z Model.

DIF3D Auxilliary Codes

In conjunction with development work on the DIF3D system, several auxiliary codes have been written. The first set of codes reads and prints some of the standard interface files[103] produced by DIF3D including RZFLUX, zone-averaged group fluxes; PWDINT, power density by interval; and ZNATDN, zone nuclide atomic densities.

The second set of codes is plotting codes that provide the capabilities of displaying power densities and the reactor geometry. One code, HEXPLT, will read the DIF3D input file and produce plots of each plane showing the region boundaries. This is a very useful error-checking feature. Another code, PLTPWR, reads the power density file generated from an R-Z problem and plots two pictures -- a 2-D plot of power in the driver and radial blanket regions (Fig. 60) and a contour plot (Fig. 61). Several codes have been written

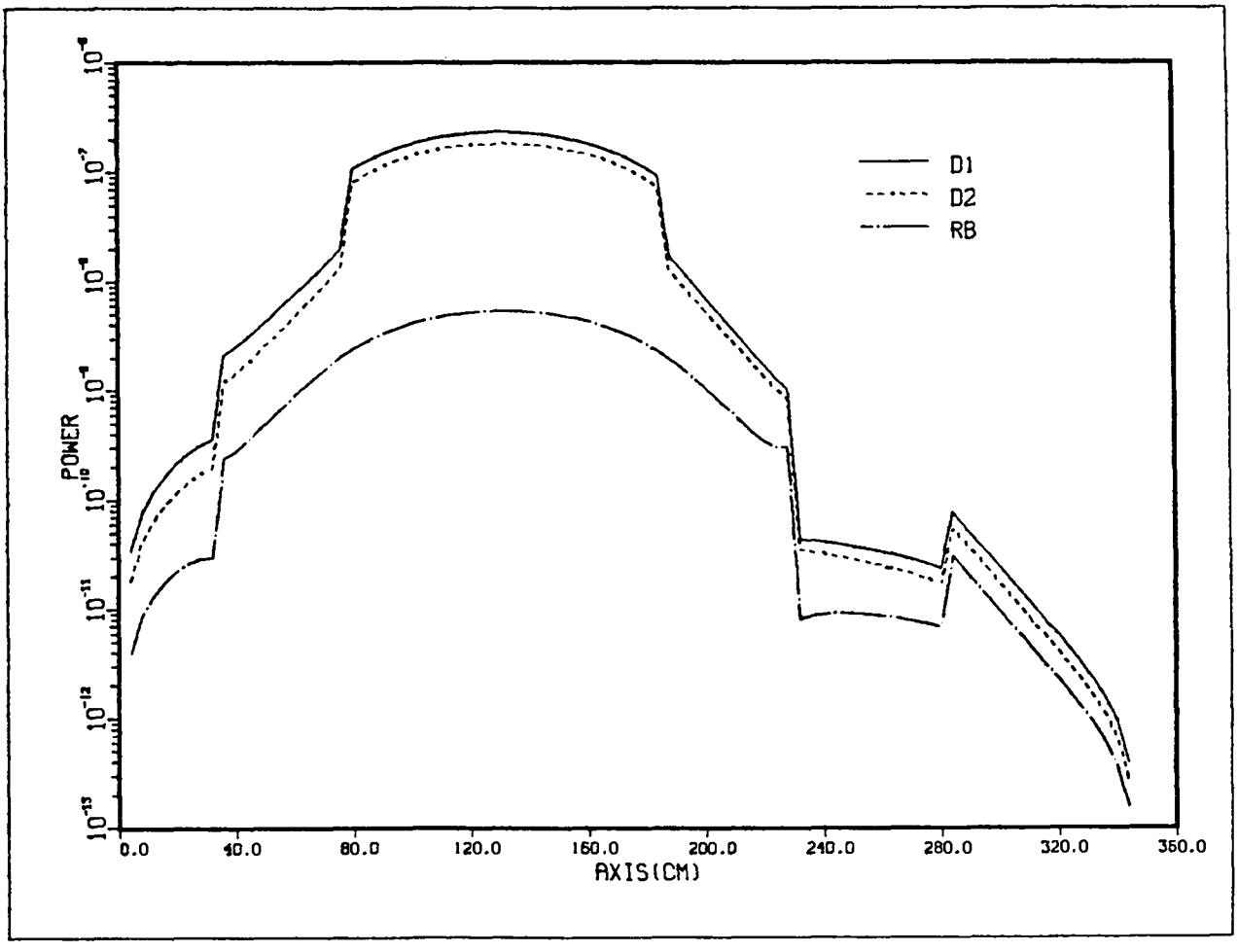

Fig. 60. Axial power traces in two driver regions and radial blanket. Power units normalized to 1 Watt.

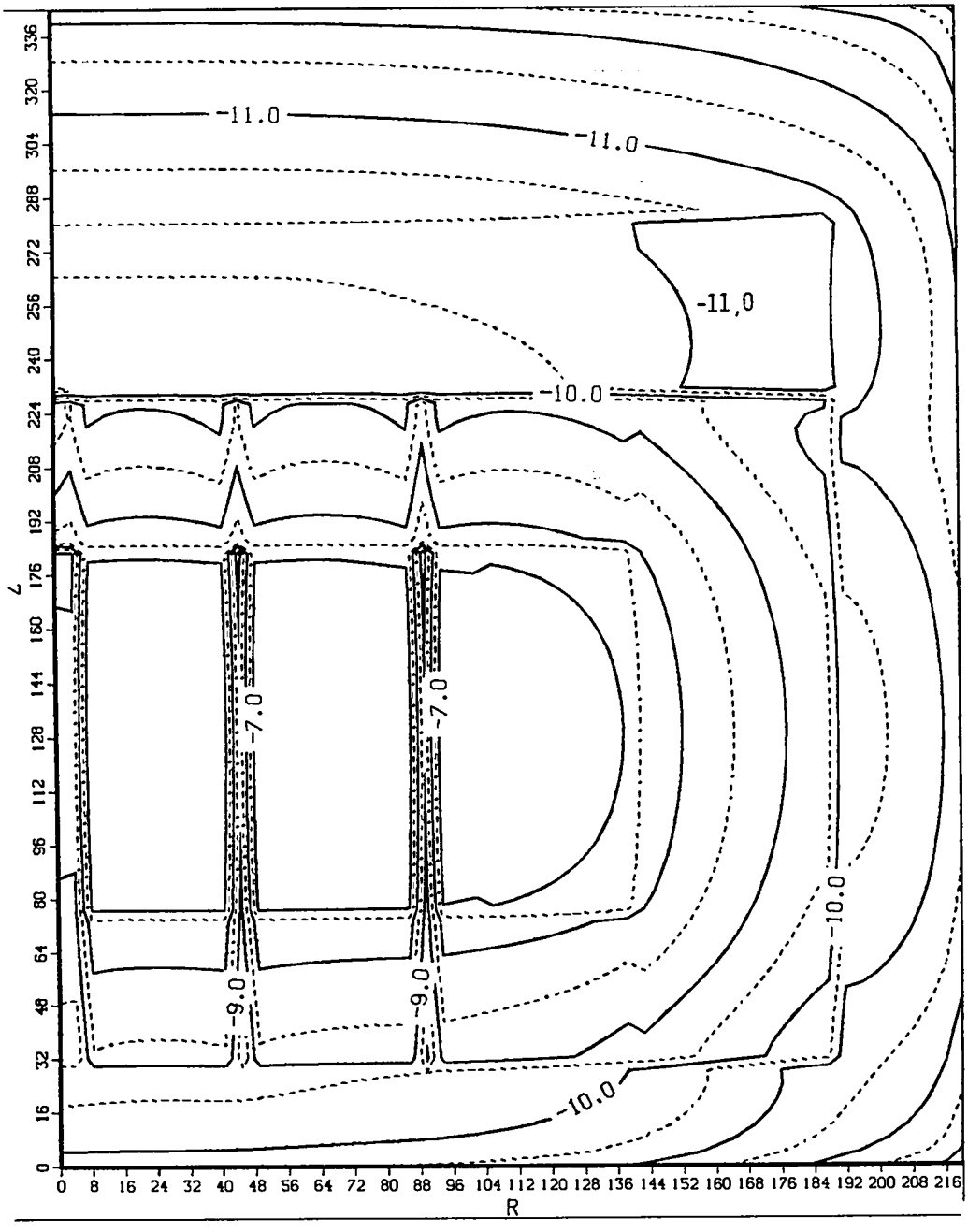

Fig. 61. Power contours for CDS R-Z model. Contours to 1/2 decade steps. Power normalized to 1 Watt

to produce a contour plot superimposed on a plot of the geometric regions (Fig. 62). These types of plots are available for nodal DIF3D and Triangle-Z (both 6 and 24 triangles per hex) problems. Logarithmic contour plots show the contours all the way out to the edge of the reactor core. Linear contours are also available; these contours are superimposed on a region geometric plot terminated at a maximum ring value.

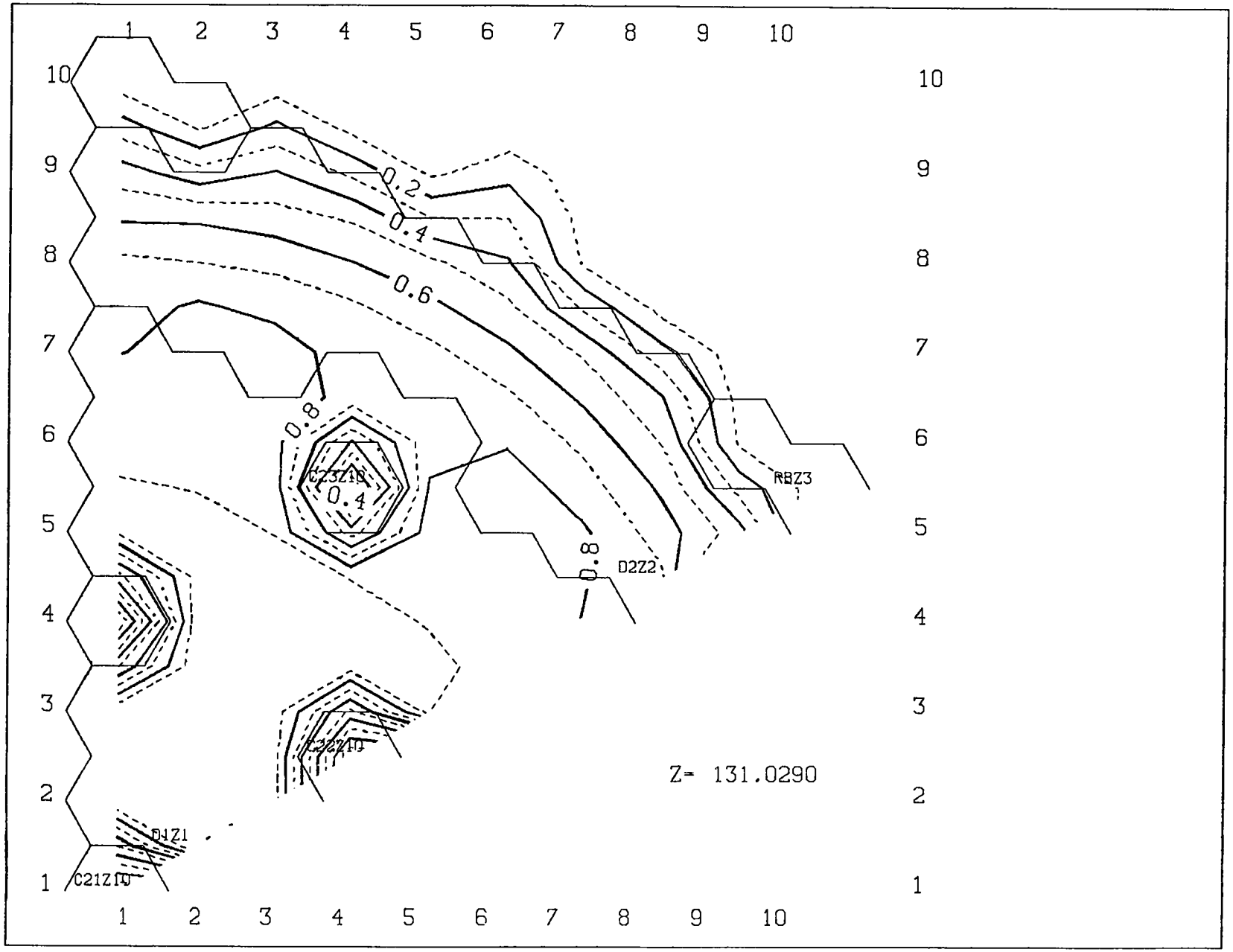

Fig. 62. Power Contours from DIF3D nodal CDS model.

REFERENCES

1. G. M. Hale, D. C. Dodder, and P. W. Keaton, "Fusion Cross Sections for Polarized Particles," E. D. Arthur, Comp., in "Applied Nuclear Data Research and Development, April 1, 1982-September 30, 1982," Los Alamos National Laboratory report LA-9647-PR (April 1983), p. 1.

2. G. M. Hale, "Cross Sections for Polarized Fusion Reactions," Polarized Fusion Fuel Workshop, Madison, Wisc. (March 1983), Los Alamos National Laboratory document LA-UR 83-727 (March 1983).

3. B. P. Ad'yasevich and D. E. Fomenko, "Analysis of the Results of the Investigation of the Reaction D(d,p)T with Polarized Deuterons," Yad. Fiz. 9, 283 (1969) [Trans. Sov. J. Nucl. Phys. 9, 167 (1969)].

4. W. Grüebler, V. König, P. A. Schmelzbach, B. Jenny, and J. Vybiral, "New Highly Excited ^{4}He Levels Found by the ^{2}H(d,p)^{3}H Reaction," Nucl. Phys. A369, 381 (1981).

5. G. M. Hale, D. C. Dodder, and J. C. DeVeaux, "Charged-Particle Elastic Cross Sections," K. H. Böckhoff, Ed., Proc. Int. Conf. Nucl. Data Sci. Technol., Antwerp, Belgium, September 6-10, 1982 (D. Reidel Pub. Co., Boston), p. 326.

6. A. Andrade and G. M. Hale, "A Generalized Fokker-Planck Equation: The Inclusion of the Nuclear and Coulomb-Nuclear Interference Cross Sections (σ_{NI}) in the Small Angle Scattering Regime," Sherwood Plasma Theory Meeting, Alexandria, Virginia, March 1983, Los Alamos National Laboratory document LA-UR 83-84.

7. A. Beyerle, S. G. Glendinning, C. R. Gould, S. El-Kadi, C. E. Nelson, F. O. Purser, L. W. Seagondollar, R. L. Walter, "Triangle University Nuclear Laboratory Neutron Physics," in Reports to the D.O.E. Nuclear Data Committee, U.S. Department of Energy report DOE/NDC-15/U, p. 209 (May 1974).

8. A. Gilbert and A. G. W. Cameron, "A Composite Nuclear Level Density Formula with Shell Corrections," Can. J. Phys. 43, 1446 (1965).

9. J. L. Cook, H. Ferguson, and A. R. de L. Musgrove, "Nuclear Level Densities in Intermediate and Heavy Nuclei," Aust. J. Phys. 20, 477 (1967).

10. E. D. Arthur, P. G. Young, and G. M. Hale, "ENDF/B-V Data File for ^{15}N (MAT 1307)," described in BNL-NCS-17541 (ENDF-201), Ed., R. Kinsey, National Nuclear Data Center, Brookhaven National Laboratory, Upton, New York (July 1979).

11. P. G. Young and E. D. Arthur, "GNASH: A Preequilibrium-Statistical Nuclear Model Code for Calculations of Cross Sections and Emission Spectra," Los Alamos Scientific Laboratory report LA-6947 (November 1977).

12. F. Ajzenberg-Selove and C. L. Busch, "Energy Levels of Light Nuclei H=11-12," Nucl. Phys. A 336, 1 (1980).

13. F. Ajzenberg-Selove, "Energy Levels of Light Nuclei A = 13-15," Nucl. Phys. A 360, 1 (1981).

14. F. Ajzenberg-Selove, "Energy Levels of Light Nuclei A = 16-17," Nucl. Phys. A 375, 1 (1982).

15. F. G. Perey, "Optical-Model Analysis of Proton Elastic Scattering in the Range of 9 to 22 MeV," Phys. Rev. 131, 745 (1963).

16. C. M. Perey and F. G. Perey, "Deuteron Optical-Model Analysis in the Range of 11 to 27 MeV," Phys. Rev. 132, 755 (1963).

17. F. D. Becchetti, Jr., and G. W. Greenlees, in Polarization Phenomena in Nuclear Reactions, H. H. Barschall and W. Haeberli, Eds. (The University of Wisconsin Press, Madison Wisc., 1971), p. 682.

18. D. L. Lessor and R. E. Schenter, "Neutron Spectra from (α,n) Reactions in Plutonium Compounds Calculated from Hauser-Feshbach Theory," Battelle Pacific Northwest Laboratories report BNWL-B-109 (1971).

19. P. Axel, "Electric Dipole Ground State Transition Width Strength Function," Phys. Rev. 126, 671 (1962).

20. D. M. Brink, thesis, Oxford University, Oxford, England.

21. B. Zeitnitz, H. Dubenkropp, R. Putzki, G. J. Krouac, S. Cierjacks, J. Nebe, and C. B. Dover, "Neutron Scattering from ^{15}N: (1). R-Matrix and Phase-Shift Analyses," Nucl. Phys. A 166, 443 (1971).

22. R. Prasad, D. C. Sarkar, and C. S. Khurana, "Measurement of (n,p) and (n,α) Reaction Cross Sections at 14.8 MeV," Nucl. Phys. 85, 476 (1966).

23. P. Fessenden and D. R. Maxson, "^{14}N(n,d)^{13}C, ^{14}N(n,t)^{12}C, and ^{15}N(n,d)^{14}C near E_n = 14 MeV," Phys. Rev. 158, 938 (19617).

24. P. G. Young, Comp., "Applied Nuclear Data Research and Development, October 1, 1981-March 31, 1982," Los Alamos National Laboratory report LA-9468-PR (March 1982).

25. E. D. Arthur, "Calculation of ^{239}Pu Neutron Inelastic Cross Sections," K. H. Böckhoff, Ed., Proc. Int. Conf. Nucl. Data Sci. Technol., Antwerp, Belgium, September 1982 (D. Reidel Pub. Co., Boston), p. 556.

26. E. D. Arthur, Comp., "Applied Nuclear Data Research and Development, April 1, 1982-September 30, 1982," Los Alamos National Laboratory report LA-9647-PR (April 1983).

27. J. Raynal, "Optical Model and Coupled-Channel Calculations in Nuclear Physics," International Atomic Energy Agency report IAEA-SMR-9/8 (1970).

28. C. I. Baxman and P. G. Young, Comps., "Applied Nuclear Data Research and Development, January 1,1981-March 31, 1981," Los Alamos National Laboratory report LA-8874-PR (July 1981).

29. C. Budtz-Jørgensen, H. Knitter, and D. L. Smith, "Neutron-Induced Fission Cross Section of ^{238}Pu in the Energy Range from 5 eV to 10 MeV," K. H. Böckhoff, Ed., Proc. Int. Conf. Nucl. Data Sci. Technol., Antwerp, Belgium, September 1982 (D. Reidel Publ. Co., Boston), p. 206.

30. K. Kari and S. Cierjacks, "Measurement of the Fast Neutron Fission Cross Sections of ^{239}Pu and ^{240}Pu," Proc. Int. Conf. Neutron Phys. and Nucl. Data, Harwell, U.K., 1978, p. 206.

31. W. P. Poenitz, J. F. Whalen, and A. B. Smith, "Total Neutron Cross Sections of Heavy Nuclei," Nucl. Sci. Eng. 78, 333 (1981).

32. A. B. Smith and P. T. Guenther, "On the Neutron Inelastic-Scattering Cross Sections of ^{232}Th, ^{233}U, ^{235}U, ^{238}U, and ^{239}Pu, and ^{240}Pu," Argonne National Laboratory report ANL/NDM-63 (1982).

33. R. Gwin, R. R. Spencer, R. W. Ingle, J. H. Todd, and H. Weaver, "Measurements of the Average Number of Prompt Neutrons Emitted per Fissions of ^{239}Pu and ^{235}U," Oak Ridge National Laboratory report ORNL/TM-6246 (1978).

34. J. Frehaut, "Recent Results on Prompt $\bar{\nu}$ Measurements between 1.5 and 15 MeV," communicated to the National Nuclear Data Center at Brookhaven National Laboratory in 1980, available as SCISRS accession number 20490.

35. D. G. Madland and J. R. Nix, "New Calculation of Prompt Fission Neutron Spectra and Average Prompt Neutron Multiplicities," Nucl. Sci. Eng. 81, 213 (1982).

36. A. B. Smith, P. Guenther, and J. Whalen, "Total and Elastic Scattering Neutron Cross Sections of ^{239}Pu," J. Nucl. Eng. 27, 317 (1973).

37. R. B. Schwartz, R. A. Schrack, and H. T. Heaton II, "Total Neutron Cross Sections of ^{235}U, ^{238}U, and ^{239}Pu from 0.5 to 15 MeV," Nucl. Sci. Eng. 54, 322 (1974).

38. E. Gadioli and L. Zetta, "Level Density of Light Nuclei," Phys. Rev. 167, 1016 (1968).

39. J. R. Huizenga and L. Moretto, "Nuclear Level Densities," Ann. Rev. Nucl. Sci. 22, 427 (1972).

40. E. D. Arthur, "The Impact of Nuclear Level Density Models on Cross Section Calculations," invited paper presented at the IAEA Advisory Group Meeting on Basic and Applied Nuclear Level Densities, Brookhaven National Laboratory, Upton, New York, April 12-15, 1983 (to be published).

41. C. L. Dunford, "A Unified Model for Analysis of Compound Nucleus Reactions," Atomics International report AI-AEC-12931 (1980).

42. J. Bardeen, L. N. Cooper, and J. R. Schrieffer, "Theory of Superconductivity," Phys. Rev. 108, 1175 (1957).

43. S. G. Nilsson, "Binding States of Individual Nucleons in Strongly Deformed Nuclei," K. Dan. Vid. Selsk. Mat.-Fys. Medd. 29, No. 16 (1955).

44. P. A. Seeger and R. C. Perischo, " A Model-Based Mass Law and a Table of Binding Energies," Los Alamos Scientific Laboratory report LA-3751 (October 1967).

45. P. A. Seeger and W. M. Howard, "Semiempirical Atomic Mass Formula," Nucl. Phys. A 238, 491 (1975).

46. E. D. Arthur, "Calculation of Neutron Cross Sections on Isotopes of Yttrium and Zirconium," Los Alamos Scientific Laboratory report LA-7789-MS (April 1979).

47. E. D. Arthur and P. G. Young, "Evaluated Neutron-Induced Cross Sections for ^{54,56}Fe to 40 MeV," Los Alamos Scientific Laboratory report LA-8626-MS (ENDF 304), (December 1980).

48. S. F. Mughabghab, M. Divadeenam, and N. E. Holden, Neutron Resonance Parameters and Thermal Cross Sections-Part A, (Academic Press, New York, 1981).

49. S. M. Grimes, R. C. Haight, K. R. Alvar, H. H. Barschall, and R. Borchers, "Charged-Particle Emission in Reactions of 15 MeV Neutrons with Isotopes of Chromium, Iron, Nickel, and Copper," Phys. Rev. C 19, 2127 (1979).

50. W. Dilg, W. Schantl, H. Vonach, and M. Uhl, "Level Density Parameters for the Back-Shifted Fermi Gas Model in the Mass Range 40 < A < 250," Nucl. Phys. A 217, 269 (1973).

51. S. F. Mughabghab, ENDF/B-V Data File for ^{197}Au (MAT 1379), described in BNL-NCS-17541 (ENDF-201), Ed., R. Kinsey, National Nuclear Data Center, Brookhaven National Laboratory, Upton, N. Y. (July 1979).

52. V. J. Orphan, N. C. Rasmussen, and T. L. Harper, "Line and Continuum Gamma-Ray Yields from Thermal-Neutron Capture in 75 Elements," Gulf General Atomic report GA-10248 (1970).

53. G. L. Morgan and E. Newman, "The Au(n,xγ) Reaction Cross Section for Incident Neutron Energies between 0.2 and 20.0 MeV," Oak Ridge National Laboratory report ORNL-TM-4973 (1975).

54. G. Grenier, J. P. Delaroche, S. Joly, Ch. Lagrange, and J. Voignier, "Neutron Capture Cross Sections of Y, Nb, Gd, W, and Au," Proc. Int. Conf. on Nucl. Cross Sections for Technol., Oct. 22-26, 1979, Knoxville, Tenn. (NBS Special Publication 594, 1980), p. 323.

55. B. Harmatz, "Nuclear Data Sheets for A=197," Nucl. Data Sheets 34, 101 (1981).

56. B. Harmatz, "Nuclear Data Sheets for A=198," Nucl. Data Sheets 21, 377 (1977).

57. D. G. Gardner, Proc. of Conf. on Nucl. Cross Sections and Technol., March 3-7, 1975, Washington, D.C. (NBS Special Publication 425, V. 2, 1975), p. 651.

58. C. Cowan, ENDF/B-V Data File for ^{11}B (MAT 1160), described in BNL-NCS-17541 (ENDF-201), Ed., R. Kinsey, National Nuclear Data Center, Brookhaven National Laboratory, Upton, N. Y. (July 1979).

59. F. P. Mooring, J. E. Monahan, and C. M. Huddleston, "Neutron Cross Sections of the Boron Isotopes for Energies Between 10 and 500 keV," Nucl. Phys. 82, 16 (1966).

60. R. O. Lane, C. E. Nelson, J. L. Adams, J. E. Monahan, A. J. Elwyn, F. P. Mooring, and A. S. Langsdorf, Jr., "States in ^{12}B Observed in the Scattering of Neutrons by ^{11}B," Phys. Rev. C 2, 2097 (1970).

61. G. F. Auchampaugh, S. Plattard, and N. W. Hill, "Neutron Total Cross Section Measurements of ^{9}Be, ^{10} ^{11}B, and ^{12} ^{13}C from 1.0 to 14 MeV using the $^{9}Be(d,n)^{10}B$ Reaction as a White Neutron Source," Nucl. Sci. Eng. 69, 30 (1979).

62. J. Cabe and M. Cance, "Measurement of Total Neutron Cross Sections of Be, ^{11}B, C, Al, Si, S, Ti, V, Ni, ^{235}U, ^{238}U, ^{239}Pu in the Energy Range 100 keV to 6 MeV," Commissariat a L'Energie Atomique report CEA-R-4524 (1973).

63. J. H. Coon, E. W. Graves, and H. H. Barschall, "Total Cross Sections for 14-MeV Neutrons, " Phys. Rev. 88, 562 (1952).

64. C. F. Cook and T. W. Bonner, "Scattering of Fast Neutrons in Light Nuclei," Phys. Rev. 94, 651 (1954).

65. H. B. Willard, J. K. Blair, and J. D. Kington, "Elastic Scattering Angular Distributions of Fast Neutrons on Light Nuclei," Phys. Rev. 98, 669 (1955).

66. D. Porter, R. E. Coles, and K. Wyld, "Elastic and Inelastic Scattering of Neutrons in the Energy Range 2 to 5 MeV by ^{10}B and ^{11}B," United Kingdom Atomic Energy Authority report AWRE 0 45/70 (1970).

67. C. E. Nelson, S. L. Hausladen, and R. O. Lane, "Structure Study of ^{12}B from the Elastic Scattering of Neutrons from ^{11}B," Nucl. Phys. 217, 546 (1973).

68. R. M. White, "A Study of the Higher Excitation States of ^{12}B Via the $^{11}B(n,n)^{11}B$ Reaction," Ohio University report COO-2490-6 (1977); Nucl. Phys. A 340, 13 (1980).

69. P. E. Koehler, H. D. Knox, D. A. Resler, R. O. Lane, and D. J. Millener, "Structure of ^{12}B from Measurement and R-Matrix Analysis of Sigma (Theta) for $^{11}B(n,n)^{11}B$ and $^{11}B(n,n')^{1}\leqq B^{*}$(2.12 MeV), and Shell Model Calculations," Nucl. Phys. A 394, 221-244 (1983).

70. J. C. Hopkins and D. M. Drake, "Elastic and Inelastic Scattering of Fast Neutrons from ^{10}B, ^{11}B, Natural Ge, and ^{93}Nb," Nucl. Sci. Eng. 36, 275 (1969).

71. S. G. Glenndinning, S. El-Kadi, C. E. Nelson, R. S. Pedroni, F. O. Purser, R. L. Walter, A. G. Beyerle, C. R. Gould, L. W. Seagondollar, and P. Thambidurai, "Elastic and Inelastic Neutron Cross Sections for Boron-10 and Boron-11," Nucl. Sci. Eng. 80, 256 (1982).

72. J. A. Cookson and J. G. Locke, "Elastic and Inelastic Scattering of 9.72-MeV Neutrons by ^{10}B and B," Nucl. Phys. A 146, 417 (1970).

73. J. C. Alder and B. Vaucher, "Scattering of 14.1-MeV Neutrons from ^{11}B," Nucl. Phys. A 147, 657 (1969).

74. M. Hyakutake, H. Tawara, M. Matoba, M. Sonoda, A. Katase, Y. Wakuta, and S. Nakamura, "Elastic and Inelastic Scattering of 14.1 MeV Neutrons by ^{14}N," European American Nuclear Data Committee report EANDC(J)22L (1969), p. 30.

75. P. G. Young, E. D. Arthur, C. Philis, P. Nagel, and M. Colin, "Analysis of n+^{165}Ho and ^{169}Tm Reactions," K. H. Böckhoff, Ed., Proc. Int. Conf. Nucl. Data Sci. Technol., Antwerp, Belgium, September 6-10, 1982 (D. Reidel Pub. Co., Boston), p. 792.

76. C. L. Dunford, "A Unified Model for Analysis of Compound Nucleus Reactions," Atomics International report AI-AEC-12931 (1970).

77. D. G. Madland and P. G. Young, "Neutron-Nucleus Optical Potential for the Actinide Region," Proc. Int. Conf. on Neutron Phys. and Nucl. Data for Reactors and Other Applied Purposes, Harwell, U.K., September 25-29, 1978 (published by the Organization for Economic Cooperation and Development, Paris, France), p. 349.

78. G. Haouat, J. Lachkar, Ch. Lagrange, Y. Patin, J. Sigaud, and R. E. Shamu, "Differential Cross Section Measurements for 3.4-MeV Neutron Scattering from ^{208}Pb, ^{232}Th, ^{235}U, and ^{239}Pu," Commissariat á L'Energie Atomique (CEA) report NEANDC(E) 196 "L" INDC(FR) 29L (February 1978).

79. P. G. Young, Comp., "Applied Nuclear Data Research and Development, July 1-September 30, 1981," Los Alamos National Laboratory report LA-9262-PR (March 1982).

80. P. Möller and J. R. Nix, "Nuclear Mass Formula with a Yukawa-plus-Exponential Macroscopic Model and a Folded-Yukawa Single-Particle Potential," Nuc. Phys. A 361, 117 (1981).

81. P. Möller, S. G. Nilsson, and J. R. Nix, "Calculated Ground-State Properties of Heavy Nuclei," Nuc. Phys. A 229, 292 (1974).

82. P. G. Young, Comp., "Applied Nuclear Data Research and Development, Los Alamos Scientific Laboratory report, January 1-March 31, 1975," LA-6018-PR (July 1975).

83. C. I. Baxman and P. G. Young, Comps., "Applied Nuclear Data Research and Development, April 1-June 30, 1977," Los Alamos Scientific Laboratory report LA-6971-PR (September 1977).

84. D. W. Muir, R. E. MacFarlane, and R. M. Boicourt, "Multigroup Processing of ENDF/B Dosimetry Covariances," Proc. ASTM-EURATOM Symp. Reactor Dosimetry, 4th, Gaithersburg, Maryland, March 22-26, 1982, NUREG/CP-0029 (CONF-820321), p. 655.

85. D. E. Cullen, W. L. Zijp, and R. E. MacFarlane, "Verification of Cross Section Processing Codes," Proc. 1982 Kiamesha Lake Meet. Advances in Reactor Phys. and Core Thermal Hydraulics, Kiamesha Lake, New York, September 22-24, 1982 (to be published).

86. D. E. Cullen, N. M. Greene, and R. E. MacFarlane, "The IAEA Cross-Section Processing Code Verification Project as it Applies to Shielding Data," Proc. Int. Conf. Radiation Shielding, 6th, Tokyo, Japan, May 16-20, 1983 (to be published).

87. R. Kinsey, "ENDF-102, Data Formats and Procedures for the Evaluated Nuclear Data Files, ENDF," Brookhaven National Laboratory report BNL-NCS-50496 (ENDF-102) 2nd Ed., (ENDF/B-V) (1979).

88. G. Hehn, R. D. Bächle, G. Pfister, M. Mattes, and W. Matthes, "Adjustment of Neutron Multigroup Cross-Sections to Integral Experiments," Proc. Int. Conf. Radiation Shielding, 6th, Tokyo, Japan, May 16-20, 1983 (to be published).

89. D. R. Harris, W. A. Reupke, and W. B. Wilson, "Consistency Among Differential Nuclear Data and Integral Observations: The ALVIN Code for Data Adjustment, for Sensitivity Calculations, and for Identification of Inconsistent Data," Los Alamos Scientific Laboratory report LA-5987 (December 1975).

90. T. R. England, W. B. Wilson, R. E. Schenter, and F. M. Mann, "ENDF/B-V Summary Data for Fission-Products and Actinides," Los Alamos National Laboratory document LA-UR-83-1285 (ENDF 332) (May 1983).

91. W. B. Wilson, T. R. England, R. J. LaBauve, and R. M. Boicourt, "TOAFEW-V Multigroup Cross-Section Collapsing Code and Library of 154-Group-Processed ENDF/B-V Fission-Product and Actinide Cross Sections," Electric Power Research Institute report NP-2345, Research Project 975-2, Interim Report (April 1982).

92. R. E. MacFarlane, D. W. Muir, and R. M. Boicourt, "The NJOY Nuclear Data Processing System, Volume I: User's Manual," Los Alamos National Laboratory report LA-9303-M (ENDF-324) (May 1982).

93. T. R. England, W. B. Wilson, R. E. Schenter, and F. M. Mann, "Aggregate Delayed Neutrons and Spectral Calculations using Preliminary Precursor Data Evaluated for ENDF/B-VI," Los Alamos National Laboratory document LA-UR-82-84 (April 1982). See also T. R. England, W. B. Wilson, R. E. Schenter, and F. M. Mann, "Delayed Neutron Spectral Calculation Using Augmented ENDF/BV Data," Trans. Am. Nucl. Soc. 41, 567 (1982).

94. T. R. England, W. B. Wilson, R. E. Schenter, and F. M. Mann, "Aggregate Delayed Neutrons and Spectra Using Augmented ENDF/B-V Precursor Data," Los Alamos National Laboratory document LA-UR-83-1270 (April 1983).

95. F. M. Mann, M. Schrieber, R. E. Schenter, and T. R. England, "Compilation of Neutron Precursor Data," K. H. Böckhoff, Ed., Proc. Int. Conf. Nucl. Data Sci. Technol., Antwerp, Belgium, September 6-10, 1982 (D. Reidel Pub. Co., Boston), p. 272.

96. B. G. Whitmore and W. B. Baker, "The Energy Spectrum of Neutrons from a Po-Be Source," Phys. Rev. 78,799 (1950).

97. J. F. Ziegler, Helium Stopping Powers and Ranges in All Elemental Matter, Vol. 4 of The Stopping and Ranges of Ions in Matter, (Pergamon Press, New York, N.Y., 1977).

98. M. Balakrishnan, S. Kailas, and M. K. Mehta, "A Study of the Reaction $^{19}F(\alpha,n)\ ^{22}Na$ in the Bombarding Energy Range 2.6 to 5.1 MeV," Pramana 10, 329 (1978).

99. R. L. Lehman, "Neutron Groups in the Spectrum of a PuF_4 Source," Phys. Rev. 171, 1311 (1968).

100. R. J. Barrett and R. E. MacFarlane, "The MATXS-TRANSX System and the CLAW-IV Nuclear Data Library," Proc. Int. Conf. Nucl. Cross Sections for Technol., Oct. 22-26, 1979, Knoxville, Tenn. (NBS Special Publication 594, 1980), p. 213.

101. R. D. Lawrence, "The DIF3D Neutronics Option for Two- and Three-Dimensional Diffusion Theory Calculations in Hexagonal Geometry," Argonne National Laboratory report ANL-83-1 (March 1983).

102. W. W. Little, Jr., and R. W. Hardin, "2DB User's Manual-Revision 1," Battelle-Pactific Northwest Laboratories report BNWL-831 Rev. 1 (August 1969).

103. R. D. O'Dell, "Standard Interface Files and Procedures for Reactor Physics Codes, Version II," Los Alamos Scientific Laboratory report LA-6941-MS (September 1977).

☆ U.S. GOVERNMENT PRINTING OFFICE: 1983-0-676-026/84

Printed in the United States of America
Available from
National Technical Information Service
US Department of Commerce
5285 Port Royal Road
Springfield, VA 22161

Microfiche (A01)

Page Range	NTIS Price Code	Page Range	NTIS Price Code	Page Range	NTIS Price Code	Page Range	NTIS Price Code
001-025	A02	151-175	A08	301-325	A14	451-475	A20
026-050	A03	176-200	A09	326-350	A15	476-500	A21
051-075	A04	201-225	A10	351-375	A16	501-525	A22
076-100	A05	226-250	A11	376-400	A17	526-550	A23
101-125	A06	251-275	A12	401-425	A18	551-575	A24
126-150	A07	276-300	A13	426-450	A19	576-600	A25
						601-up*	A99

*Contact NTIS for a price quote.

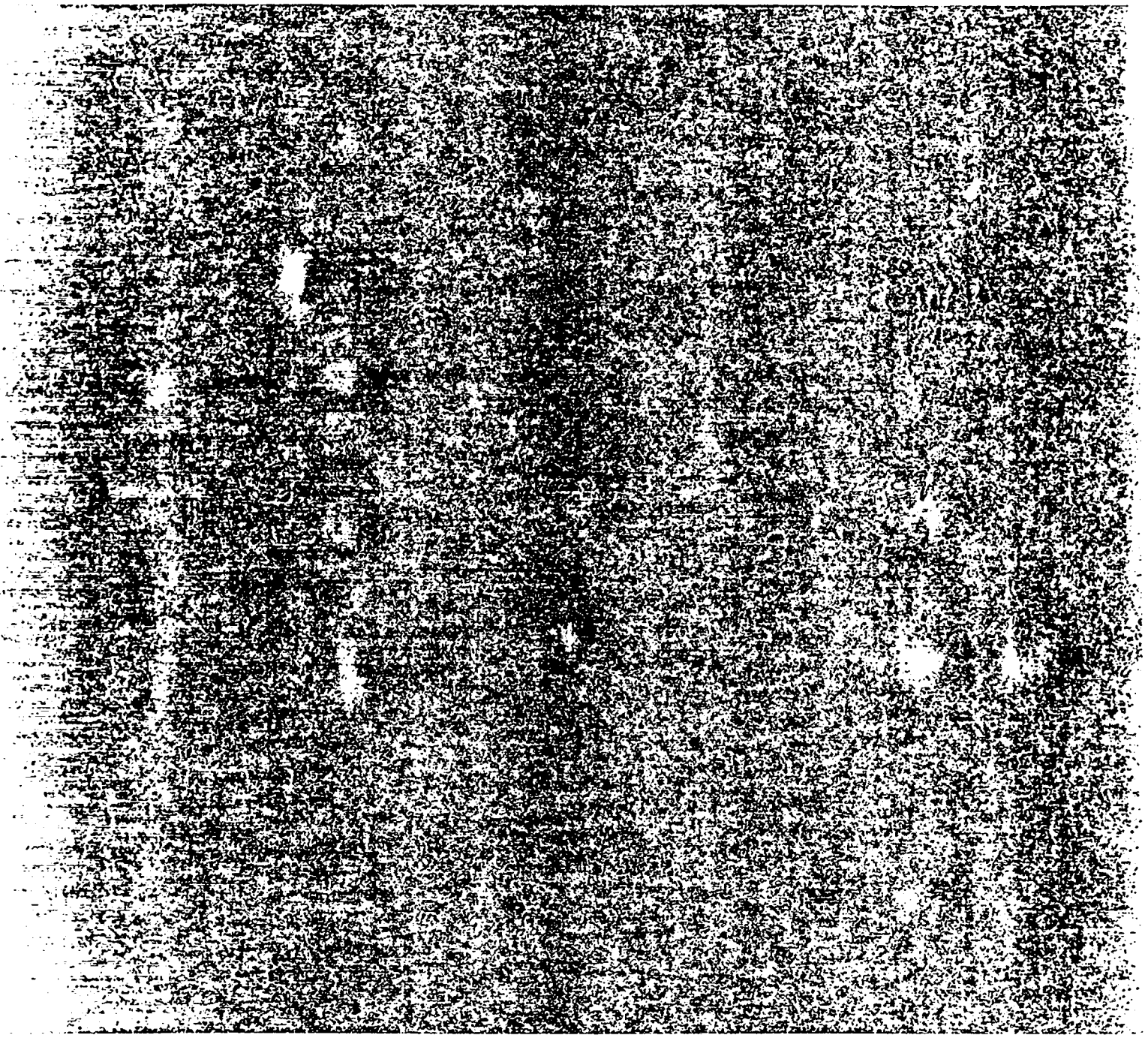

Los Alamos